

Development and validation of a scanned proton beam model for dose distribution verification using Monte Carlo

Erik Almhagen

Supervisors:

David Boersma, Håkan Nyström and Anders Ahnesjö

Thesis for Master of Science in Medical Radiation Physics

2015/08/31

Contents

Sammanfattning på svenska	3
Abstract	4
1 Introduction	5
1.1 The beam line at Skandionkliniken	8
1.2 Monte Carlo	12
1.2.1 Basic method	12
1.2.2 Geant4/GATE	15
1.2.2.1 Step size	16
1.2.2.2 GATE actors	17
1.3 Purpose	18
2 Method	19
2.1 Overview	19
2.2 Data	20
2.2.1 Beam profile measurements	20
2.2.2 IC2/3 data	21
2.2.3 IDD curves	21
2.3 Optical parameters	24
2.4 Energy parameters	31
2.5 Simulations	34
2.5.1 GATE configuration	34
2.5.1.1 Geant4 related settings	34

2.5.1.2	GATE beam profile simulation geometry	36
2.5.1.3	Proton beams	36
2.5.2	Log file to GATE plan file conversion	38
2.6	Beam model validation	40
2.6.1	Optical parameters	40
2.6.2	Energy parameters	40
2.6.3	MatriXX measurements	40
2.6.3.1	Hardware	40
2.6.3.2	Treatment plans	41
2.6.3.3	Normalization	41
2.6.3.4	Gamma index test	41
3	Results	43
3.1	Optical parameters	43
3.2	Energy parameters	46
3.3	Gamma index test	49
4	Discussion	57
4.1	Results	57
4.2	Method	60
5	Conclusion	63
	Appendix	64
	List of abbreviations	74
	Bibliography	74

Sammanfattning på svenska

Bakgrund:

Skandionkliniken är Sveriges nya anläggning för protonterapi med behandlingsstart 2015. En svept stråle används exklusivt. Eftersom Skandionkliniken i samband med att The Svedborg-laboratoriet stängdes ned för kliniskt bruk är den enda anläggningen av sitt slag i Sverige är stråltid en dyr vara. Med mer omfattande QA-mätningar generellt än vad som brukas vid konventionellt fotonbaserade anläggningar eftersöks en metod som kan minimera mängden stråltid som behövs vid QA-mätningar. Syftet med detta examensarbete var att ta fram en strålmödel som kan beskriva strålen vid Skandionklinikens gantry 1 samt utföra enkel validering av denna. Strålmödeln i kombination med loggfilerna som beskriver hur en bestrålning faktiskt gick till används då som indata till en Monte Carlo-simulering som då förhoppningsvis slutligen kan ge en tillförlitlig bild av den levererade dosfördelningen, utan behov för mätning.

Metod:

GATE, baserat på Geant4, användes som Monte Carlo-kod. Den strålmödel som togs fram är en enkel parametrering av fasrymden vid nozzle-utgången där samtliga simuleringar börjar. För att ta fram strålmödeln användes det databibliotek som togs fram i samband med inmätning av systemet. Detta komplementerades i sin tur av data från loggfilerna som genererades under dessa mätningar. För att köra simuleringar baserade på loggfilerna skrevs en MATLAB-kod som konverterar loggfilerna till en behandlingsplan som GATE kan läsa. Därefter gjordes en mängd mätningar av 2D-dosfördelningar. Från mättillfällerna togs loggfilerna som då simulerades och senare kunde jämföras med mätresultaten. Gammaindex användes för att jämföra dosfördelningarna.

Resultat:

Strålmödeln kan i de flesta fall förutspå spotstorleken på strålen inom 0,2 mm. Den kan också förutspå range inom 0,2 mm. Energispridningen i strålen var något svårare att modellera, men fanns ändå vara inom klinisk acceptabel osäkerhet. Resultaten från utvärdering av gammaindex vid jämförelse av dosfördelningarna komplicerades av olika faktorer, men man kan argumentera att efter viss rimlig datamanipulering fås acceptabla resultat.

Slutsats:

Bortsett från de komplikationer som uppstod under vissa delar av valideringen av strålmödeln verkar strålmödeln i sig kapabel till att producera goda resultat. Mer genomgående validering måste utföras innan strålmödeln kan brukas klinisk. En absolutkalibrering av något slag är också nödvändigt. Vidare optimering av metoden som helhet för att öka hastigheten kan också vara nödvändigt för kliniskt bruk. Att använda sig av GPU eller investera i ett datorkluster kan vara nödvändigt.

Abstract

Background and purpose:

Although proton therapy is becoming increasingly common as a radiotherapy modality, facilities offering proton therapy are still scarce in comparison to photon therapy. Sweden's new proton therapy facility, Skandionkliniken, is scheduled to be in operation during August 2015, employing the pencil beam scanning technique. Given Skandionkliniken's unique stance as the only facility offering proton therapy in Sweden as of this writing, it is important to minimize the need for measurements during quality assurance to free up beam time for patients and other endeavors. It is the purpose of this work to create a foundation for a method whereby dose distribution verification is done via Monte Carlo simulation by developing and performing simple validation of a beam model. As input for simulating a dose distribution, log files storing a wide variety of data on how the dose distribution was delivered were used.

Method:

GATE, an open source Monte Carlo code and built on top of Geant4, was used for all simulations. A beam model parameterizing phase space at the nozzle exit was developed. The beam model development process made use of the beam data library and log file data. Using an in house developed code to convert log file data to treatment plans readable by GATE allowed simulation of delivered dose distributions. For validation, gamma index tests were performed comparing measured and simulated dose distributions.

Results:

The beam model was found able to predict the spot size in almost all cases within 0.2 mm. Likewise, the beam model was able to predict the proton range within 0.2 mm. The energy spread was found to be more difficult to estimate; comparisons of simulated and measured curves for at six points around the Bragg peak yielded a maximum deviation of 0.86 mm. Several difficulties prevented easy interpretation of the results of the gamma index tests. If allowance is made for certain data manipulation, pass rates of 90% or above using the global method can be achieved for all depths and for both treatment plans scanned.

Conclusion:

Although some complications arose during validation, the beam model performance appears capable of producing accurate results. To produce a full product suitable for routine patient specific quality assurance, further work will be necessary. Significant computing power would also be mandatory for routine use, necessitating the acquisition of a dedicated computer cluster or using GPUs.

Chapter 1

Introduction

It is generally held that Wilson[1] was the first person to suggest usage of protons for radiotherapeutical applications. The short paper mentions the favorable characteristics of the well known proton Bragg curve with its sharp Bragg peak. Although the first attempts at proton therapy, taking place at the Lawrence Berkeley Laboratory, California, did not make use of the Bragg peak, its utilization was finally implemented at the Gustav Werner institute in Sweden[2]. Ever since these pioneering steps, the number of proton therapy facilities around the world have increased exponentially[3]. The sharp Bragg peak of the protons translates into a greater concentration of dose into a smaller region, relative to photons. Since the position of the Bragg peak is a function of proton kinetic energy, which can be controlled, it is possible to ensure that the target, typically a tumor, is at or around the location of the peak.

Beyond a certain range the dose deposition is virtually zero for protons. No such range can be ascribed to photons. There are multiple proton range metrics in the literature; some of these are summarized in Table 1.1. In this work statements about range, unless otherwise specified, will be referring to the projected range. The finite range of protons is beneficial in the sense of allowing for reduction of the total energy deposited during treatment by more than half, but the very sharp post-Bragg peak fall off necessitates that the range be known with considerable accuracy during treatment planning[4, 5]. Overestimating the range of the protons may lead to parts of the target receiving little or no dose, whereas underestimating it may lead to a high dose to nearby healthy tissue. Noise in the treatment planning CT images may contribute significantly to range uncertainties[6]. This follows from the use made of Hounsfield Units (HU) to calculate the relative stopping power; the latter ultimately controls the proton range.

A reduction in range uncertainty can potentially be achieved using a dual energy CT scan as opposed to the more conventional single energy CT; further, using Monte Carlo techniques where HUs are converted to material composition rather than relative stopping powers the effects of uncertainties in HUs can to some degree be mitigated[5]. Ultimately uncertainties in the proton range may force the treatment planner to increase the margins, resulting in a larger high dose region[7]. Furthermore, the costs involved in the construction of a proton therapy facility are far greater than for more conventional photon based radiotherapy, the former requiring a cyclotron or a synchrotron and possibly large gantries; these make out the most expensive components[8]. A proton therapy treatment may cost

Table 1.1: A summary of a few range metrics found in the literature.

Range metric	Description
Projected range	The average range of the protons, projected along the beam direction axis, ignoring protons that have undergone nuclear interactions. Approximately equal to the depth of the distal 80% dose point.
CSDA range	Continuous Slowing Down Approximation. The path length of the protons, obtained by integrating the reciprocal of the total stopping power. To good approximation equivalent to the projected range in the clinically relevant energy interval.
Practical range	The depth of the distal 10% dose point.

twice that of a photon therapy treatment[9]. Eventually technological advances may reduce costs for proton therapy to levels comparable with advanced forms of photon therapy[10, 11, 8, 12].

The general goal of radiotherapy is to cure patients, typically by delivering a conformal dose distribution to a target. Modern radiotherapy utilizing photons typically use techniques such as intensity modulated radiotherapy (IMRT) or volumetric arc therapy (VMAT) to deliver conformal dose distributions. The photon beam is modulated in 2D by use of a multileaf collimator (MLC), allowing the incident photon beam to take on a variety of irregular shapes, limited by the resolution of the MLC. In proton therapy, passive scattering has traditionally been the most widely used technique. In passive scattering, the narrow proton pencil beam emerging from the beam line is spread out laterally by scattering foils. This laterally spread out beam may then similar to photon based therapy pass through beam shaping devices such as an MLC to provide a conformal dose distribution. Given the narrow width of a Bragg peak, it is also necessary to spread it out in depth as the target is typically larger than the width of the peak. In passive scattering, this is accommodated for by using a modulator wheel. The modulator wheel thickness varies along its circumference, and as it rotates, the kinetic energy of the protons having passed through it will vary with the wheel thickness. This results in a spread out Bragg peak (SOBP); an example case is shown in Figure 1.1.

An important new trend in proton therapy is the use of so called pencil beam scanning, employed for clinical use first at the pioneering Paul Scherrer Institute (PSI)[13]. Pencil beam scanning is currently the most advanced proton therapy delivery technique, allowing for the proton therapy equivalent of IMRT, called intensity modulated proton therapy (IMPT)[14, 15]. Pencil beam scanning uses the narrow pencil beams that emerge from the beam line without subjecting them to scattering foils as in passive scattering. The pencil beams are scanned across the target and due to their narrow width the technique requires no mechanical beam shaping at all. The superposition of all these pencil beams may then result in a to the target homogeneous and conformal dose distribution. As noted above, the concept of range is not suitable when describing photon-matter interaction. Modulation in depth is therefore not possible with photons, but since protons do have a finite range that depends on the kinetic energy of the protons, controllable by the user, modulation in all three dimensions is possible. This added dimension may allow the treatment planner greater flexibility, and hopefully, a more conformal dose distribution.

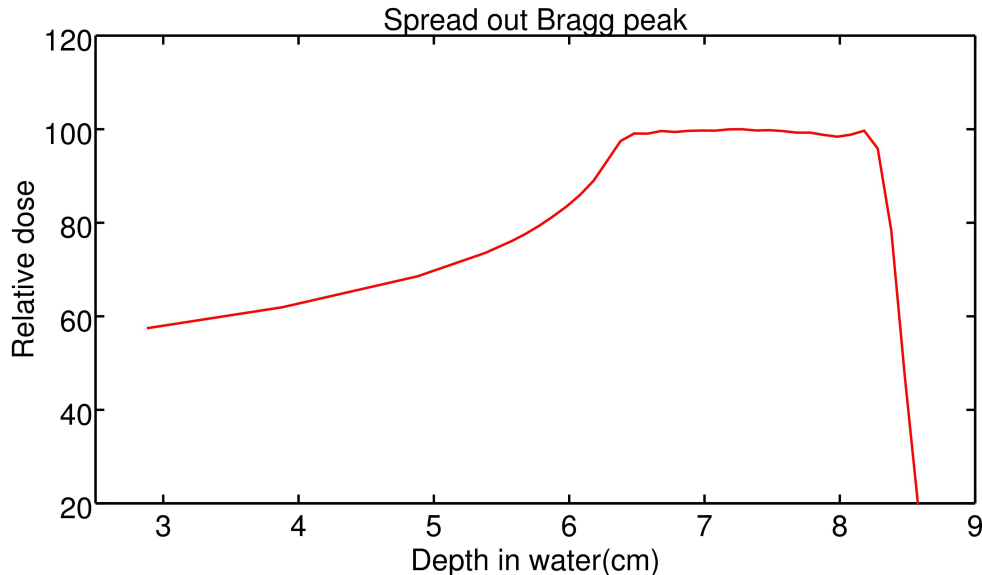


Figure 1.1: Illustrating a 2 cm wide spread out Bragg peak (SOBP). It is the result of a superposition of a number of quasi-monoenergetic beams of various energies and weights.

In passive scattering, the spreading out of the proton beam both laterally and in depth allows simultaneous irradiation of the entire target. In pencil beam scanning on the other hand, the target is divided into a number of layers, each layer corresponding to a certain proton kinetic energy. Each layer is divided into a number of spots, or pencil beam positions. One layer is scanned at a time, and once it is completed, the energy is changed and the next layer is scanned. A pencil beam scanning treatment plan may be expressed as a number of spot positions which is the position of the pencil beam at isocenter, the energy for the spot positions, as well as spot weights, typically expressed in monitor units (MU). Although pencil beam scanning as noted above may ultimately yield more conformal dose distributions, one of the advantages of the passive scattering technique is its reduced sensitivity to patient movement; with pencil beam scanning, only a small part of the target is being irradiated at any one time. If the target were to move during the scanning of a certain layer, parts of the target may not receive the planned dose. Since movement may occur as central parts of the target is being scanned, increasing the margins will not help. Various techniques have been suggested to deal with this difficulty, such as target tracking, gating and rapid re-scanning[16].

Peripherally around the central axis direction of a pencil beam is a low dose region often referred to as the halo, consisting of the particles having undergone nuclear interactions; the latter usually cause large angle deflection relative the incident primary particle direction of the secondary particles. Neglecting the halo in dose calculations may introduce non-negligible errors, as it may contribute up to 15% of the total dose of a treatment[17]. The extent of the halo relative the spot size is large; for field sizes of 20x20 cm² the halo may affect the beam output[18]. Lin et al. has published a series of papers in which a method to experimentally characterize the halo was developed[19, 20, 21]. Following the central limit theorem the spatial extent of the primary protons in a pencil beam may to good approximation be described by a single Gaussian, as these have exclusively undergone electromagnetic

interactions, characterized by continuous low angle deflections and small kinetic energy loss. Nuclear interactions are much rarer, and as indicated above, may yield large angle deflections and large loss of kinetic energy of the incident primary proton. To accurately model this behavior, using a combination of a triple Gaussian or a double Gaussian and a Cauchy-Lorentz function has been suggested[22, 23]. Since a treatment plan may consist of thousands of individual spots, an accurate characterization of the individual pencil beam, including the halo, is important for the calculation of the dose distribution.[22]

In order to obtain an accurate view of the delivered dose distribution following irradiation of a patient, these complexities must be handled by the treatment planning system (TPS). At the same time, the TPS must be fast enough for clinical applications, allowing for interactive work. The necessary compromise between these ideals leads to the TPS employing various simplifications, with some loss of accuracy in its dose calculations as a necessary result. Differences in the calculated dose distribution *contra* the actually delivered dose distribution need not only result from inaccuracies in the TPS, however; the translation of the treatment plan into a series of instructions, and the subsequent execution of these instructions by the entire treatment system (including the cyclotron and all components along the beam line) may also contribute to uncertainties in the delivered dose distribution. For these reasons, a patient specific quality assurance(QA)-process is necessary, where the delivered dose distribution is confirmed so as not to deviate too much from the planned dose distribution. Typically, this is done by performing measurements in a water phantom. Given the current paucity relative photon based alternatives of proton therapy centers, beam time is an expensive commodity. Any efficient QA-process therefore ought to minimize the beam time necessary to perform said validation.

A recent development in patient specific QA methods is the use of log files[24, 25, 26, 27]. Since monitoring systems are mandatory equipment for most radiotherapy systems, linacs as well as cyclotrons, it is possible to have them report the parameters they measure continuously throughout an irradiation. In proton therapy, examples of parameters measured include gantry angle, the position of the spot at the monitor chamber, the charge produced in the monitor chamber per spot etc. For linacs, the positions of the MLC leafs would also likely be recorded in the log files. Since the log files contain data on how the treatment plan was actually delivered as opposed to how it should have been delivered, it allows reconstruction of the delivered dose distribution.

An inherent weakness of the method is that it can only be performed after an irradiation. In fractionated treatment however only a part of the the planned dose is delivered during the first irradiation, whereby possible errors during the first fraction are hopefully small and correctable for subsequent fractions. More serious errors may be caught by interlocks, shutting the beam down for instance if the monitoring chamber readings differ by too much. Ultimately, it does solve the problem of beam time by minimizing the need for measurements as the log file data can be used as input to a TPS or other dose-calculation engine to calculate the delivered dose distribution, and this could be compared to the original, planned dose distribution.

1.1 The beam line at Skandionkliniken

Skandionkliniken is the name of Sweden's, at the time of this writing, newly built proton therapy facility. It is an Ion Beam Applications (IBA) powered facility, exclusively using the pencil beam scanning technique. Proton therapy has previously been available in Sweden, albeit employing the passive scattering technique, and for relatively few patients (typically in the order of 100/year); only

a single, fixed beam room was available. At Skandionkliniken, there are currently two gantries, with a third being planned. An isochronous cyclotron is used for accelerating the protons up to 230 MeV, after which a degrader and an energy selection system is available to provide a wide selection of energies. The protons are transported through the beam line consisting of a vacuum pipe, slits, quadrupoles and dipoles.

At the end of the beam line is the nozzle, the proton therapy equivalent of the gantry head. A schematic illustration of the nozzle is found in Figure 1.2. It is an IBA pencil beam scanning (PBS) dedicated nozzle. It contains two ionization chambers: IC1 at the nozzle entrance which is operated at a lower air pressure (200 mbar) to minimize scattering, and IC2/3 at the nozzle exit which is vented and thus operated at room temperature and pressure. These are for beam monitoring, and apart from the chambers and entrance and exit foils the nozzle interior is held at vacuum, making the cumulative amount of material in the beam path in the nozzle uniquely small. For final beam steering and shaping there are two dipoles and two quadrupoles. Upon leaving the nozzle, the protons enter the treatment room air, in which they will travel until striking the patient/phantom surface.

A basic understanding of the accelerator and beam line is necessary to understand the so called optical and energy properties of the beam (see Chapter 2), as the description of these is the prime objective of the beam model. Only a basic review will be presented here; for more in depth reviews, the reader may consult the following publications and their bibliographies[28, 29, 30]. Figure 1.3 shows a simple drawing of a cyclotron. Two electrodes are situated in a vacuum chamber. A magnetic field is applied, perpendicular to the plane of the left side of the image in Figure 1.3. The shape of the metallic pieces are reminiscent of the letter D, whence they are often referred to as “dees”. The dees are connected to a high voltage AC power supply. An ion source is placed near the center of the vacuum chamber, in between the dees. An electric field is thus created between the dees, and the ions will therefore be accelerated toward one of them. Inside the dees, the electric field is zero. The direction of the resultant Lorentz force will be perpendicular to the direction of the ions at all times, forcing the ions into a circular path. Once the ions leave the dee again, the alternating current will have switched signs so as to accelerate the ions across the gap to the other dee again, and the process is repeated.

An ion traveling in a circular path in a dee will experience both a centrifugal and a centripetal force, both being equal. Therefore

$$Q(E + v \times B) = \frac{mv^2}{r}$$

where Q is the charge of the ion, E is the electric field strength and B is the magnetic field strength. Since $E = 0$ inside the dees

$$Q(v \times B) = \frac{mv^2}{r} \implies QBr = mv \quad (1.1)$$

At this point, it is easy to calculate the kinetic energy of the particles as

$$\frac{Q^2 B^2 r^2}{2m} = \frac{mv^2}{2} \quad (1.2)$$

Furthermore, the time it takes the ions to complete one turn is constant, as shown by

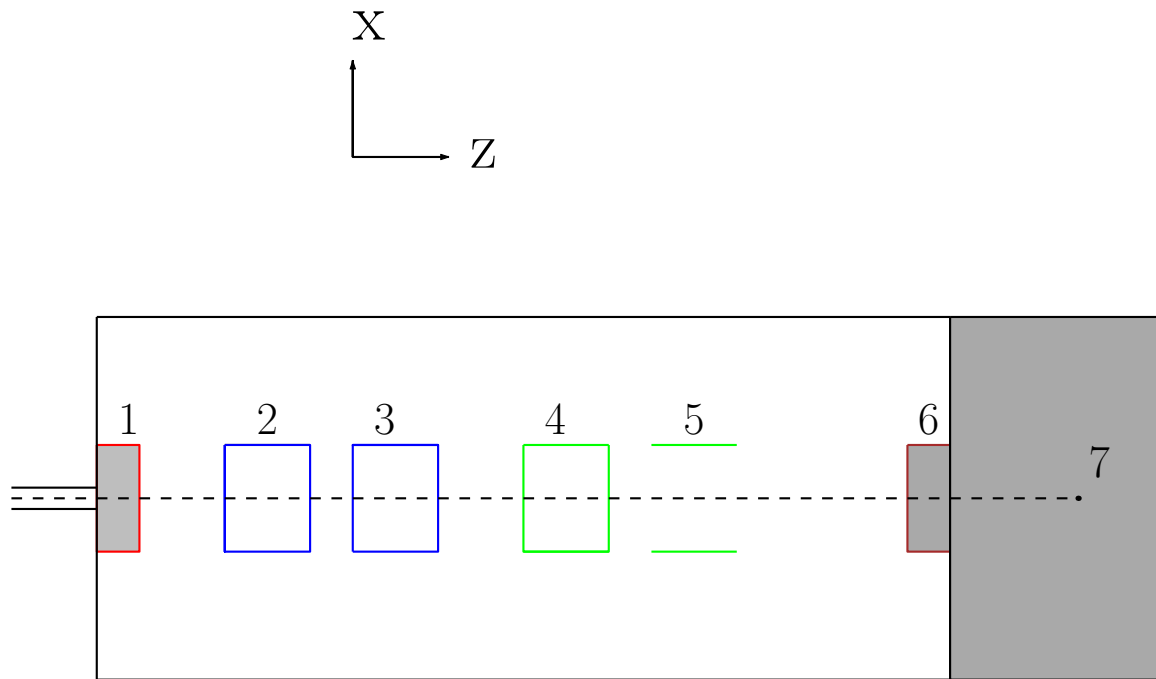


Figure 1.2: A schematic illustration of the nozzle. The beam travels in the positive z direction, from left to right, as indicated by the dashed line. x is up and y is perpendicular to the plane of the illustration, i.e. out of the page. The IC1 ion chamber is denoted by 1, held at 200 mbar air pressure (indicated in light gray). Denoted by 2 and 3 are quadrupoles providing focusing in x and y respectively. Denoted by 4 and 5 are the dipoles steering the beam in x and y respectively. The final component of the nozzle in the illustration, denoted by 6, is the IC2/3 chamber, held at room temperature and pressure (indicated in gray). Upon leaving the nozzle after IC2/3, the beam enters the treatment room air (indicated in gray). The dot at 7 marks the isocenter. The nozzle overall is roughly 2 meters long, and the air gap from the nozzle to isocenter is roughly 50 cm.

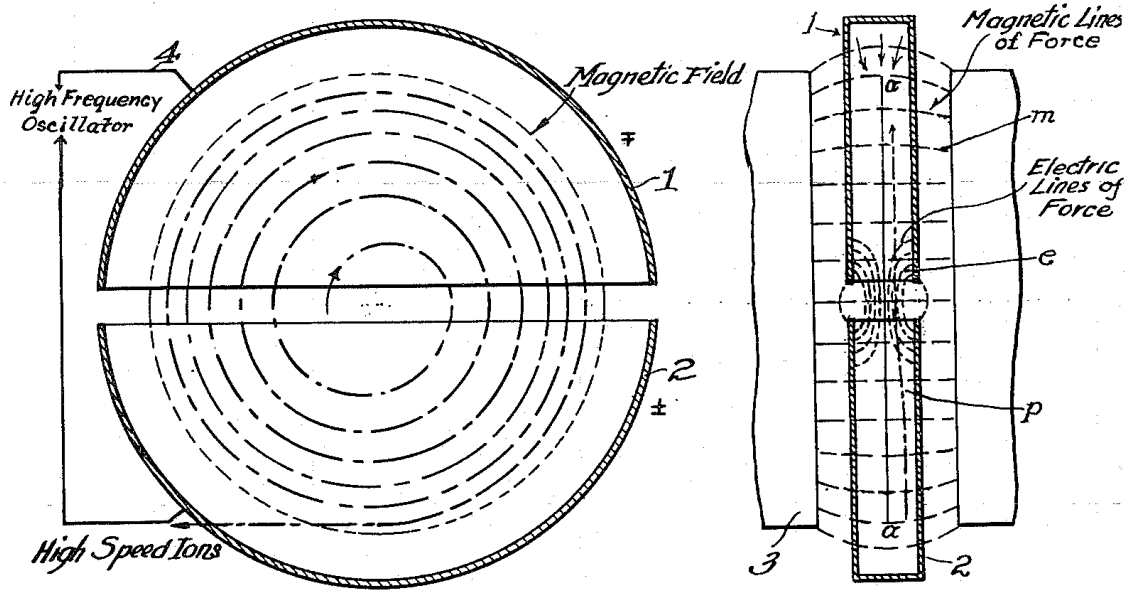


Figure 1.3: Illustrating the basic components of a cyclotron. From the original patent application by Ernest O. Lawrence, inventor of the cyclotron. Now in the public domain.

$$v = \frac{2\pi r}{t} \implies t = \frac{2\pi r}{v} = \frac{2\pi m}{QB} \quad (1.3)$$

where the last equality follows from Equation 1.1. By setting the frequency of the alternating current to half this time, the protons will be accelerated every time they cross the gap between the dees.

Notable is that the kinetic energy of the particles at a given radius is independent of the strength of the electric field. The strength of the magnetic field and the radius of the cyclotron determines the maximum kinetic energy a cyclotron is capable of providing, as given by Equation 1.2. However, although Equation 1.3 suggests a constant magnetic field is appropriate, it fails to take relativistic effects into account. The isochronous cyclotron at Skandionkliniken accelerates protons up to a kinetic energy of 230 MeV. At this energy, protons are traveling at $\frac{v}{c} \approx 0.6$ times the speed of light, and the Lorentz factor $\gamma \approx 1.25$. Therefore, as the protons are accelerated they will gain mass and the time per turn in Equation 1.3 is not a constant. An isochronous cyclotron deals with this problem by using a magnetic field strength that varies with the radius r to ensure that t is kept constant.

All protons leaving the cyclotron at Skandionkliniken will have a kinetic energy of around 230 MeV. If a treatment plan calls for another, lower energy, the protons may pass through a degrader. Low Z materials are preferable for degraders, as their scattering power is low; the cumulative, or multiple scattering angle of a proton relative the incident direction having passed through a low Z material is therefore in general lower than for a high Z material.[31] Due to the random, statistical nature of proton electromagnetic interactions in an absorber, not all protons will lose exactly the same amount of energy, nor will the multiple scattering angle be the same for all protons. Following the degrader, the

protons will pass through the rest of the beam line consisting of various slits, dipoles and quadrupoles. The dipoles are necessary to steer the beam along the beam pipe, to prevent the protons from crashing into the pipe wall. In combination with the slits, it is possible to make sure only a narrow band of energies are able to pass through the beam line to the nozzle, and protons with energies deviating too much from the requested are effectively prevented from reaching the nozzle.

To ensure that the size of the pencil beam does not grow too large due to the different angle of travels of all the protons in the beam, quadrupoles, generally in doublets, are located along the beam line. It can be shown that quadrupoles in multiplets have a net focusing effect on the beam in the sense of decreasing the spatial extent of the beam, even though a single quadrupole only has a focusing effect in one dimension and defocusing in another.[32] The beam finally entering the nozzle will therefore hopefully be characterized by a small angular and energy spread. Its position and spatial spread, or size, will be measured by the ionization chambers in the nozzle. The collected charge in the chambers will also allow for a measure of the intensity of the beam. Standard correction (i.e. for temperature and pressure etc) factors are applied and the collected charge may be presented as MUs, the unit by which the TPS designates the weight, or amount of dose, per pencil beam. Through reference dosimetry measurements the dose delivered at a reference depth per monitor units may be determined so as to enable the TPS to convert the planned dose distribution into monitor units for each specified beam spot. Finally, two dipoles direct the beam as required by the treatment plan.

It is the objective of the beam model as developed in this thesis to describe a set of properties of the beam at the nozzle exit, i.e. once it has passed through the entire beam line as described above as to enable calculation of further beam propagation by Monte Carlo transport code. The beam model is further described in Chapter 2.

1.2 Monte Carlo

1.2.1 Basic method

The MC method may be considered a very accurate method for dose calculations[33]. The dose calculation methods used by TPS are as noted above commonly different, utilizing semi-analytical algorithms to ensure calculations are fast enough to allow the planner to work interactively. The implied weakness of the MC method currently is thus its speed, being in general significantly slower than other alternatives. In the future this may be remedied by gains in computational power. Significant acceleration of dose calculations using MC is possible however by fully utilizing the potential in present day graphics processing units (GPU), widely available; some promising results have been published[34, 35, 36, 37]. Readers unfamiliar with the MC method in radiotherapy and transport theory may consult the following short article and its references[38].

The MC method derives its accuracy by working from first principles, considering the interactions of each simulated particle in some detail. Indeed, in so called analog MC every interaction is considered individually, and the transport solved as exactly as our theories of particle interaction allow. Given the large number of interactions charged particles may undergo as they pass through an absorber, analog MC is not always a feasible option[39, 38]. A solution to this problem is so called condensed history transport, where several interactions taking place during a chosen simulation step size s are bundled together[40]. The processes of scattering, energy loss and streaming or drifting, may be considered

separately; as such, it is an operator-split method. It has been shown that the result of such an operator-split, condensed history method is a solution to the Boltzmann equation in the limit of the step size $s \rightarrow 0$ [41].

In the case of scattering, the property of interest is the accumulated scattering angle relative its incident direction, after having undergone a number of interactions in a medium, where in most cases a single scattering interaction only contributes a small deviation of the particle direction. Cases where the number of scattering interactions is large is usually referred to as multiple Coulomb scattering (MCS), and several theories have been developed to provide probability distributions for the multiple scattering angle. These include theories by Moliere[42], Lewis[43], Goudsmit & Saunderson[44] and Fermi-Eyges[45]. Energy loss, or stopping, is typically handled by dividing incident particle-electron collisions into two categories; hard and soft. In the latter case, the incident particle loses energy continuously, and no secondary particles are generated; in this case the energy loss due to collisions with electrons (bremsstrahlung may be neglected for protons in the clinically relevant energy interval) may be described by the Bethe-Bloch equation

$$-\frac{dE}{dx} \frac{1}{\rho} = 0.3072 \frac{Z}{A} \frac{1}{\beta^2} z^2 \left(\frac{1}{2} \ln \frac{2m_e c^2 \beta^2 W_{max}}{1 - \beta^2} - \beta^2 - \ln I - \frac{C}{Z} - \frac{\delta}{2} \right) \quad (1.4)$$

where the following notation has been used:

ρ Absorber material mass density

Z Absorber material atomic number

A Absorber material atomic mass

$\beta = \frac{v}{c}$ where v is the speed of the incident particle

z Incident particle charge

m_e Electron mass

c Speed of light in vacuum

W_{max} Maximum energy transfer in a collision

I Mean excitation energy

δ Density correction

$\frac{C}{Z}$ Shell correction.

The correction terms may safely be ignored in the clinically relevant energy interval. In Figure 1.4 the linear collisional stopping power using Equation 1.4 is plotted for water, with $\frac{Z}{A} = 0.55$ and $I = 75$ eV and with the corrections neglected.

In hard collisions, secondary particles are generated and tracked; dose deposition does not occur on the spot as in soft collisions. Given the large mass difference between protons and electrons, $W_{max} \approx 0.55$ MeV for 230 MeV protons. The range in water for 0.55 MeV electrons is on the order of 2 mm, which is approximately the size of a pixel element in a CT image, wherefore ignoring tracking of electrons may lead to speed gains with acceptable loss of accuracy for most clinical applications[46]. The threshold for hard collisions must otherwise be set appropriately. Decreasing thresholds increase CPU time as

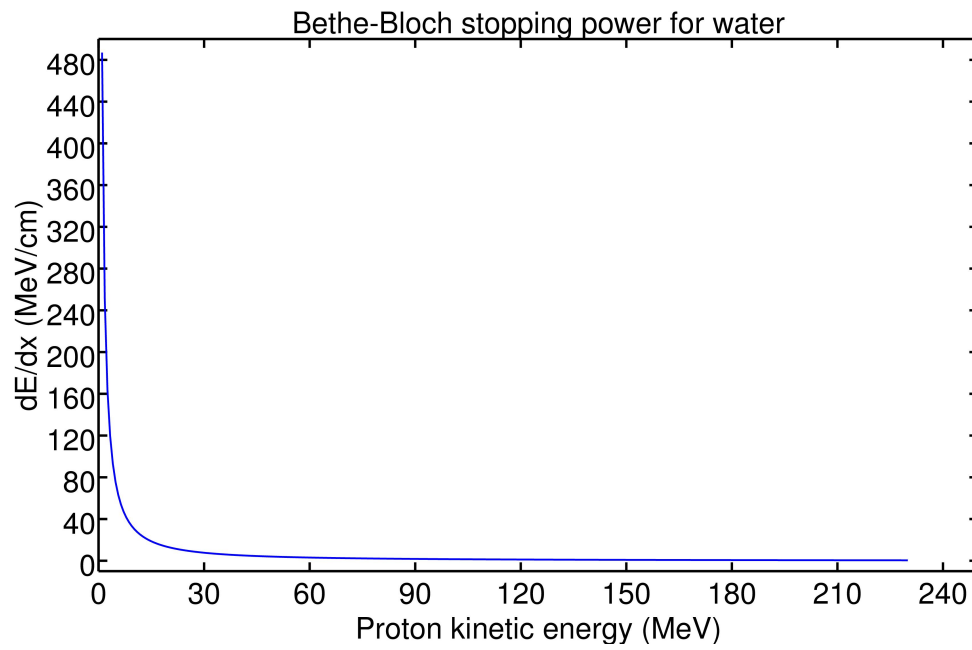


Figure 1.4: Linear collisional stopping power, according to the Bethe-Bloch equation without the higher order correction terms.

more time is spent on tracking secondary particles. Increasing them will speed the simulation up, but with some loss of accuracy.

Equation 1.4 is accurate for proton kinetic energies throughout the clinically relevant range, except for kinetic energies below 1 MeV where the Born approximation is no longer valid [47]. One of the main areas of uncertainty when applying Equation 1.4 is I , the mean excitation energy. It cannot be derived from first principles, and must be measured. Since I enters in a logarithmic expression, the impact of uncertainties in its numerical value is relatively weak, but it is still significant: a study by Andreo indicated that for a 122 MeV proton beam in water, the Bragg peak position may vary by as much as 3 mm using different values of I found in the literature[48].

Actual implementations of these techniques in the form of computer software are available in various forms. Some widely used MC codes include FLUKA[49], Geant4[50, 51] and MCNPX[52]. These codes are versatile with applications well beyond the boundaries of the medical physics field, which may cause difficulties for the medical physicist new user. Geant4 in particular requires substantial knowledge of C++ for usage. Several options that cater more exclusively to the medical physics field have subsequently been developed, with a more user friendly interface. These include TOPAS[53], GAMOS [54] and GATE[55, 56, 57]. These examples are all based on Geant4; however, instead of C++ simpler macro languages are used to define such things as simulation geometry, physics processes and particle source. As detailed further in Section 2, work for this thesis has been carried out using GATE.

1.2.2 Geant4/GATE

Since GATE is built on top of Geant4, some understanding of Geant4 is necessary to understand GATE. As previously noted, Geant4 is a versatile tool, intended for use in a wide variety of fields. It deals with this by making available a substantial set of models, simulating various physics processes such as Coulomb scattering and nuclear interactions, for various particles. Most of these models are limited in their applicability. As such, a user interested in high energy physics simulations, as for instance with the Large Hadron Collider at CERN, would be simulating physics processes with models appropriate for a certain relevant energy interval and particles. For medical applications, other physics processes and another energy interval will be more relevant, and in Geant4 it is the responsibility of the user to make appropriate choices for his or her particular simulation.

The standard package for electromagnetic processes is implemented as a number of classes known as options which the user may call to construct a physics list, which is a list of all particles and models for the physics processes the user wishes to simulate. When the standard package is called, it sets up a number of models to model various electromagnetic processes, as well as a number of parameters pertinent for these models. As an example of a model, the default MCS model is the Urban model, which in turn is based on the Lewis MCS theory[58].

An example of a parameter is the threshold for hard and soft collisions as described above. It is determined in Geant4 by production cuts whereby a user may chose to have particles tracked if they fulfill certain criteria. An example of a production cut is a range cut. A range cut of 2 mm for electrons means that a collision yielding an electron with CSDA range greater than 2 mm will be considered hard, and the produced δ -electron will be tracked. If the range would be less than 2 mm, the collision is considered soft and the energy is deposited locally in accordance with Equation 1.4. For the standard

electromagnetic package, the default range cut for electrons is 1 mm, although the user is able to set it to an arbitrary value, with the added caveat that lower values will require more central CPU time.

1.2.2.1 Step size

As previously stated, in the limit as the step size approaches 0, the condense history method approaches an exact solution to the Boltzmann equation. The step size is therefore an important parameter. What follows is thus a short review of the step size issue; the reader may consult the relevant documentation for further details[59]. Geant4 differentiates the so called geometrical path length, which is the shortest distance between the end points of a step (which is a straight line, unless a magnetic field is present), and the true path length, which is the actual path length as traveled by the particle in between the end points. The latter is thus in general longer than the former. The Geant4 transportation system uses the geometrical path length, i.e. the particle is transported in a series of straight lines. However, since physics processes such as scattering and energy loss are sensitive to the true path length traveled by the particle, a transformation must be performed to go from one to the other.

The step size selection works by first looping over all pertinent physics processes; the model assigned to each of these will propose a true path length as a step size. The minimum of these is selected. It is then compared to other limits set by the user. An example of such a limit in the default option of the standard electromagnetic package is that the step size may not exceed 20% of the residual range of the particle. Of the minimum true path length compared again with other limits, the minimum is again selected. This is then transformed into a geometrical path length. The resultant geometrical path length is then compared to the distance to the nearest boundary, to make sure that the particle cannot cross into a different volume without stopping at the boundary. The minimum of these is again selected, transformed back into a true path length, and this true path length is then used when calculating the multiple scattering angle and the energy loss during the step. The particle is then transported a distance equal to the geometrical path length.

Integrating equation 1.4 is computationally expensive. Therefore, before particle tracking begins, Geant4 evaluates it at a certain number of energies, controllable by the user, and fills tables with the resultant values. These tables may then be interpolated appropriately for a specific energy, and the energy loss ΔE for a certain true path length t of a single step is

$$\Delta E = -\frac{dE}{dx} \cdot t \quad (1.5)$$

where $\frac{dE}{dx}$ is evaluated using the kinetic energy of the particle at the beginning of the step. Therefore equation 1.5 is valid for small true path lengths t and where the gradient of $\frac{dE}{dx}$ is small. Figure 1.4 indicates the latter is valid for most of the clinically relevant energy range in water; it breaks down, however, for lower energies. To make Equation 1.5 yield more accurate results at these lower energies, typically encountered in the dosimetrically very important Bragg peak, the user may set a so called linear loss limit. The latter is a fraction threshold; if the fraction of the particle kinetic energy lost during a step is greater than the linear loss limit, integration of Equation 1.4 is performed. Also available is a so called step limiting function, which gradually reduces the maximum step size as the particle loses energy.

The true path traveled by a charge particle is in general different from a straight line due to the large number of scattering interactions undergone, even during a typical step size of 1 mm. A MCS

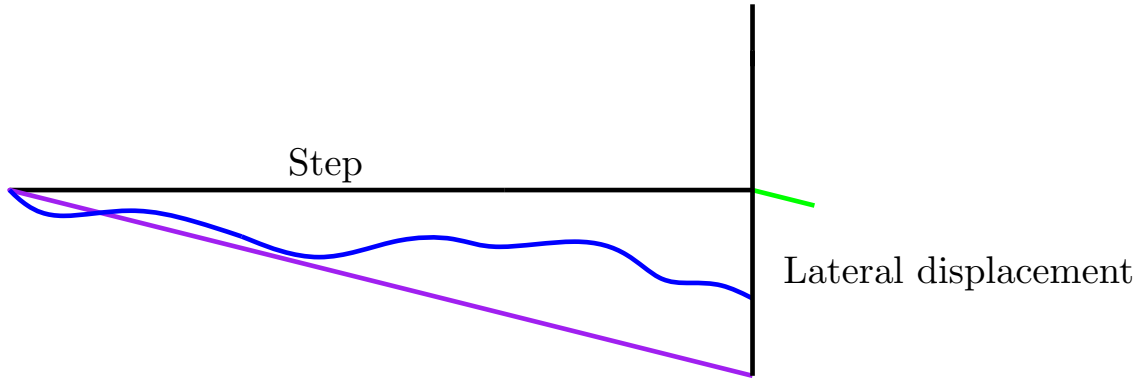


Figure 1.5: The difficulties of charged particle transport with a finite step size can be understood from this simple illustration. The black line is equivalent to a geometrical step size in Geant4 where the angle of travel is updated at the end of the step, with the new angle of travel shown in green. The purple line is the same but with the angle of travel updated at the beginning of the step. The blue line is the true path travelled by the charged particle, indicating that neither method will provide an accurate value for the spatial displacement.

model used in a simulation ought therefore not only to provide a probability distribution for the resultant multiple scattering angle following a step, but the lateral displacement of the particle. Of the MCS theories mentioned previously, only Lewis theory provides the first couple of moments of spatial displacement, and the Urban model, based on Lewis theory, exploits these to calculate the spatial displacement. The spatial displacement problem is usually the largest source of uncertainty in condensed history simulations[60].

Consider Figure 1.5. The black line corresponds to the transportation of a particle during a single step. The new direction of the particle at the end of the step, as a result of the number of scattering interactions during the step as calculated by the MCS model, is shown in green. The blue line corresponds to the true path of the particle along the step. Simply updating the particle direction at the end of each step will in general underestimate the scattering. Inversely, if the particle is transported in the scattering angle calculated for the end of the step as shown in purple in Figure 1.5, the scattering will be exaggerated. For a review of methods employed by various algorithms to solve this problem, see [61].

1.2.2.2 GATE actors

GATE is built on top of Geant4, and all of the above said of Geant4 also applies to GATE. However, in order to facilitate usage for the medical applications specialist, a set of additional medically oriented tools was introduced to GATE, besides the already mentioned use of a simple macro language instead of C++. These include a variety of so called actors that allows for the calculation and subsequent extraction of useful information from a simulation. For example, the dose actor can be attached to any volume in a simulation geometry, and the dose to that volume, either as a whole or to each voxel following a voxelization, can be provided after a simulation. Also important is the phase space actor, allowing extraction of the phase space at a given position. This lets a user focus on the practical

aspects of a simulation, as opposed to having to write accurate and efficient code and consider issues such as voxel tracking (see [62] for details on this area).

1.3 Purpose

It is the purpose of this thesis to construct a simple beam model for the pencil beam scanning system at Sweden's new proton therapy facility, Skandionkliniken, for use in Monte Carlo (MC) simulations and perform basic validation of it. This would in turn allow for what Meier et al. refers to as level 3 and level 4 independence checks of the treatment system[63]. These tests may be implemented in a patient specific QA process that might save precious beam time by performing a validation of the delivered dose distribution by means of MC simulation, using the system log files as input. Details on the method is found in Chapter 2.

Chapter 2

Method

2.1 Overview

Any MC simulation of a particle beam requires a starting point, as well as a set of input parameters describing the particle beam at that point. Options for starting points found in the literature include the beginning of the beam line where the beam exits the accelerator[64], or the nozzle entrance[65, 66], or the nozzle exit[67]. Earlier starting points necessitates modeling the geometry of a greater number of beam line components, such as ion chambers, magnets and scatterers or degraders. The feasibility of the nozzle exit approach has been argued specifically for pencil beam scanning, where beam manipulation within the nozzle is significantly smaller than in passive scattering[46, 68]. Furthermore, significant savings in the necessary CPU time per simulation is also possible in neglecting transporting the protons through the nozzle[15], although this effect will be mitigated for the nozzle at Skandionkliniken which is mostly vacuum. Therefore, the nozzle exit approach was selected as the only realistic option that would allow completion during the time frame of a master thesis work.

A beam model is a function or set of functions that supplies the necessary parameters of the beam at the starting point. As this work was carried out during the commissioning of the site, it was necessary to minimize the need for additional measurements. The method to find a beam model broadly followed was originally developed and validated by Grevillot et al.[69, 70]. Preserving the basic philosophy of this method has in the following been attempted in the sense that nothing but the beam data library (BDL) is necessary to construct the beam model. In practice, the BDL data set was complemented with data from IC2/3 (see Section 2.2). However, this data is automatically generated by the system during irradiation and is thus recoverable without having to perform additional measurements.

The method uses eight parameters to describe the beam at the nozzle exit. Six of these are so called optical parameters, and two are energy parameters. Letting the direction of the beam be along the z -axis, the optical parameters are the spot size in x and y , angular spread in x and y and emittance in x and y . The spot size and angular spread parameters are each described by single Gaussian standard deviations. The two energy parameters are the energy spread, also described by a Gaussian standard deviation, and the mean energy. By finding appropriate values for these parameters by analysis of the BDL for a selection of kinetic energies at the nozzle exit, ideally covering the energy range that

will be used at facility, a polynomial fit as a function of kinetic energy for each found parameter set is performed. Provided that each parameter varies reasonably smoothly with energy, evaluating the polynomials for an arbitrary energy within the energy interval to which the polynomials were fitted should yield accurate values of the eight parameters at the simulation starting point, i.e. the nozzle exit.

For the beam originally modeled by Grevillot et al., the beam size as a function of air depth was linear for all energies, allowing extraction of the angular spread by a fitting a straight line through the measured beam sizes for all energies and obtaining the slope. At Skandionkliniken, the beam size is a more complicated function of air depth. This followed from the fact that the nozzle at Skandionkliniken is, apart from the ion chambers, kept at vacuum, whereas the nozzle for Grevillot et al. was filled with air. This difference necessitated a generalization of the method presented by Grevillot et al. This generalized method also provides an analytical method to calculate the emittance, based on Fermi-Eyges theory. In the subsections below, the details of this generalized method will be presented.

Except when otherwise stated, all fits and numerical calculations were performed in Octave[71], a high level programming language for numerical calculations.

2.2 Data

Two kinds of data were used during beam modeling. The first is the BDL data collected during commissioning of Gantry 1 by the commissioning physicists, as required by Eclipse, the TPS used at Skandionkliniken. The BDL data pertinent for the beam model include beam profile measurements in air and IDD (integral depth dose) curves. The second kind of data is provided by the log files, recording a wide variety of set and monitored beam line parameters during the course of an irradiation. More details on the how the log files were used as input for simulations are given in Section 2.5.2.

2.2.1 Beam profile measurements

The beam profile measurements in air were performed by the commissioning physicists for Eclipse using the Lynx, a scintillator with a 30x30 cm² active surface area. Following measurement, beam profiles were obtained as 600x600 matrices, with a resolution of 0.5 mm. Beam profile measurements were carried out for 18 different proton kinetic energies, from 60 to 220 MeV in intervals of 10 MeV, as well as a measurement for the maximum energy at isocenter, 226 MeV. The energy of a beam is defined for the BDL data as the energy at isocenter in air. An initial set of measurements of beam profiles for a variety of gantry angles was performed at isocenter. Based on these data, it was decided to perform a complete set of measurements for a single gantry angle of 315°. The complete set consists of, for each of the 18 energies, beam profiles measured at five different air depths: isocenter -19 cm, isocenter -10 cm, isocenter, isocenter +10 cm and isocenter +20 cm. The negative and positive signs designate upstream and downstream of the isocenter respectively.

The spot size was characterized by a Gaussian standard deviation, and thus 2D Gaussians were fitted to each beam profile matrix. The fitting was done in ROOT[72] after converting the matrices to ROOT 2D histograms. The central 40x40 beam profile matrix, corresponding to the central 2x2 cm² of the sensitive area of the Lynx, was used for all energies. The 40x40 beam profile matrix was selected to

ensure a simple, consistent method to calculate the spot size, facilitating comparison with simulated beam profiles, whilst avoiding the low bin count and non-Gaussian region further from the center of the Lynx for all energies. The standard deviations in x and y following the fit was extracted. Grevillot et al. estimated a 0.1 mm uncertainty for spot sizes following fits of the Lynx data; this uncertainty, after having been confirmed by IBA, was also accepted for the present work. This uncertainty primarily reflects the Lynx instrumental uncertainty. The statistical uncertainty in a fit to the data is an order of magnitude or more smaller and is thus assumed to be negligible.

2.2.2 IC2/3 data

Grevillot et al. [69] performed beam profile measurements at six depths for each energy, including the nozzle exit. An extra measurement at the nozzle exit is important, as the position of the nozzle exit is approximately at isocenter -54 cm, some 35 cm from the nearest data point. Since the simulations utilizing the beam model intend to start at the nozzle exit, and all optical parameters depend on the beam size at this point (see Section 2.3), the distance to the nearest data point will cause unnecessary uncertainties in the optical parameters. However, a measurement at the nozzle exit at Skandionkliniken was hard to achieve during the commissioning phase of the facility. To overcome this problem, the beam size reading from IC2/3 was extracted from the log files, generated during the beam profile measurements. IC2/3 is a stripped ionization chamber located inside the nozzle at the exit. IC2/3 does not have as high resolution as the Lynx. A conservative estimate for the spot size uncertainty as measured with IC2/3 was given by IBA as 0.5 mm. Examples of spot sizes following 2D Gaussian fits to the data is plotted in Figures 2.1 and 2.2. The upstream most data point is that given by IC2/3; the next five result from fits to the Lynx measurements. The position of the IC2/3 data point is different in the two dimensions due to the separation of the strips in IC2/3; the spot size in x is measured some four centimeters before the spot size in y . The plots well illustrate the spot size variation with air depth is a more complicated function of energy and dimension than that for Grevillot et al.

2.2.3 IDD curves

The integral dose depth (IDD) curves were measured by the commissioning physicists for Eclipse in the IBA BluePhantom, a water phantom allowing for a 0.1 mm steps in ion chamber movement. IDD is, for a given depth, defined as the integral of dose given to a large plane perpendicular to the incident pencil beam direction. The curves were measured using the PTW 34070 plane parallel ionization chamber. Its entrance window diameter is 84 mm, making it among the larger available on the market and thus suitable for IDD-measurements. It has however been noted that even the PTW 34070 is not large enough to capture significant portions of the halo, and therefore an MC-based method was used by which the ion chamber readings may be corrected to provide a true IDD curve[73]. This correction was applied to the measured IDD curve, following a conversion from ionization to dose. Conversion from ionization to dose was necessary since the water-air stopping power ratio cannot be taken as constant in the clinically relevant proton energy range, necessitating application of the following equation (equation B.13 from the TRS-398[74])

$$s_{w,air}(z) = a + bR_{res} + \frac{c}{R_{res}} = a + b(R_p - z) + \frac{c}{R_p - z} \quad (2.1)$$

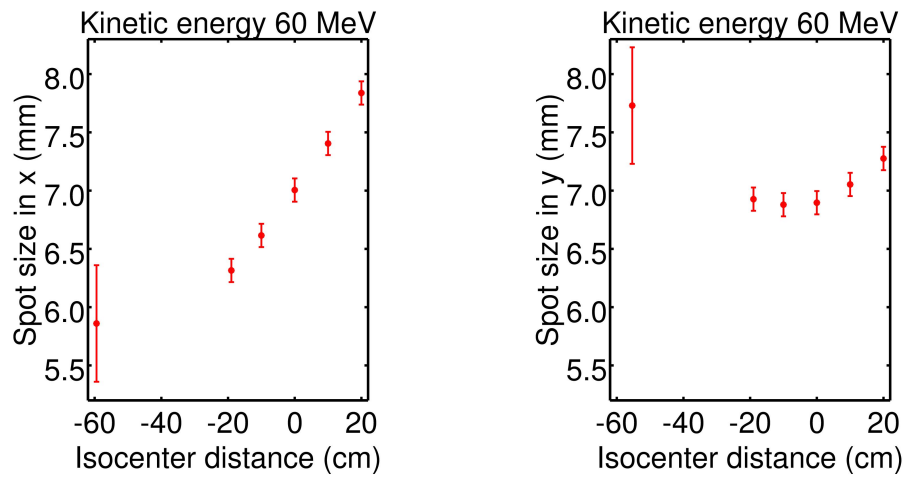


Figure 2.1: The spot sizes against air depth for 60 MeV protons. The errors in the spot sizes as shown in the errorbars were provided by IBA as 0.1 mm for the Lynx data and 0.5 mm for the IC2/3 data.

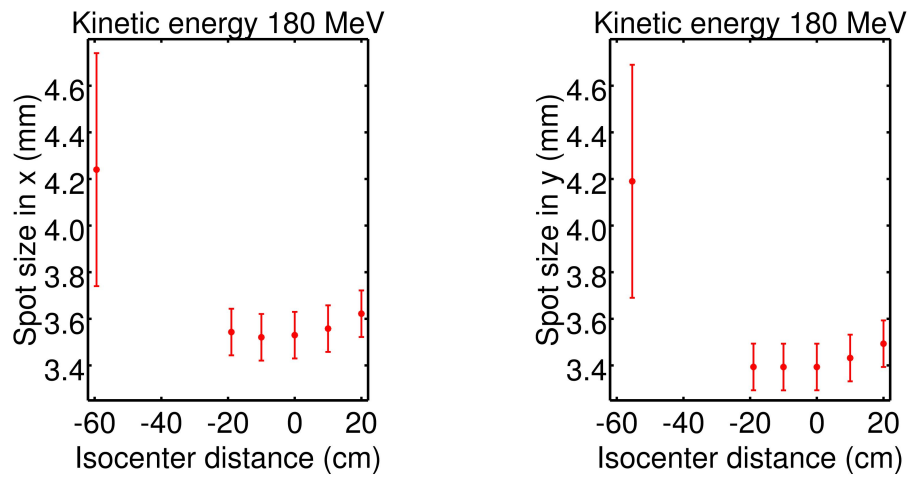


Figure 2.2: The spot sizes against air depth for 180 MeV protons. The errors in the spot sizes as shown in the errorbars were provided by IBA as 0.1 mm for the Lynx data and 0.5 mm for the IC2/3 data.

where $a = 1.137$, $b = -4.265 \cdot 10^{-5}$ and $c = 1.84 \cdot 10^{-3}$ was applied to each measured ionization curve. $R_{res} = R_p - z$ is the residual range, where R_p is the practical range (see Table 1.1) and z is the depth of interest.

2.3 Optical parameters

In order to extract the angular spread from the measured data, the original method as presented by Grevillot et al. was found not to be applicable due to the added complexity of a non-linear beam divergence/convergence. Instead, a new method had to be found. To extract a first order approximation of the optical parameters, it will first be assumed that the beam is propagated through vacuum before striking the patient. Following that, a method will be presented to correct for air.

Angular and spatial distributions are per Fermi-Eyges theory assumed to be Gaussian, and Gottschalk's [75] notation is mostly followed; his paper may also serve as an introduction to the subject of Fermi-Eyges theory, applied to proton therapy. Consider a proton beam entering a slab of a certain material at the origin (0,0,0) of a coordinate system (X, Y, Z) . Let the beam travel along the Z -axis. The basic equation of Fermi-Eyges theory, derived in a short note by Eyges[45] parametrizes the probability density of the protons' position X and direction of travel X' at depth Z in the slab as

$$P(X, X') = \frac{1}{2\pi\sqrt{B}} e^{-\frac{1}{2} \frac{A_0(Z)X^2 - 2A_1(Z)XX' + A_2(Z)X'^2}{B}} dXdX' \quad (2.2)$$

where A_0 is the variance of the angular distribution, A_1 is the covariance of X and X' and A_2 is the variance of the spatial distribution; each A_n is the n th moment of T , the scattering power of the slab. Equation 2.2 is then completed to a standard 2D Gaussian probability density function by setting B as

$$B = A_0A_2 - A_1^2$$

The discussion below will exclusively deal with the X spatial dimension, but all equally applies to Y , for which there is a corresponding equation 2.2. The set of all X, X' such that

$$A_0(Z)X^2 - 2A_1(Z)XX' + A_2(Z)X'^2 = B \quad (2.3)$$

makes out an in general elliptical shape in X, X' -space, and the area enclosed by it is ε , which also provides an interpretation of B .

$$\varepsilon = \pi\sqrt{A_0A_2 - A_1^2} = \pi\sqrt{B}. \quad (2.4)$$

A_0 , A_1 and A_2 are all functions of Z , but for convenience this notation has been dropped in the equation above, and this practice will continue throughout this section. The area ε in X, X' -space is known as the emittance, and is a measure of the correlation of the spatial position and angle or

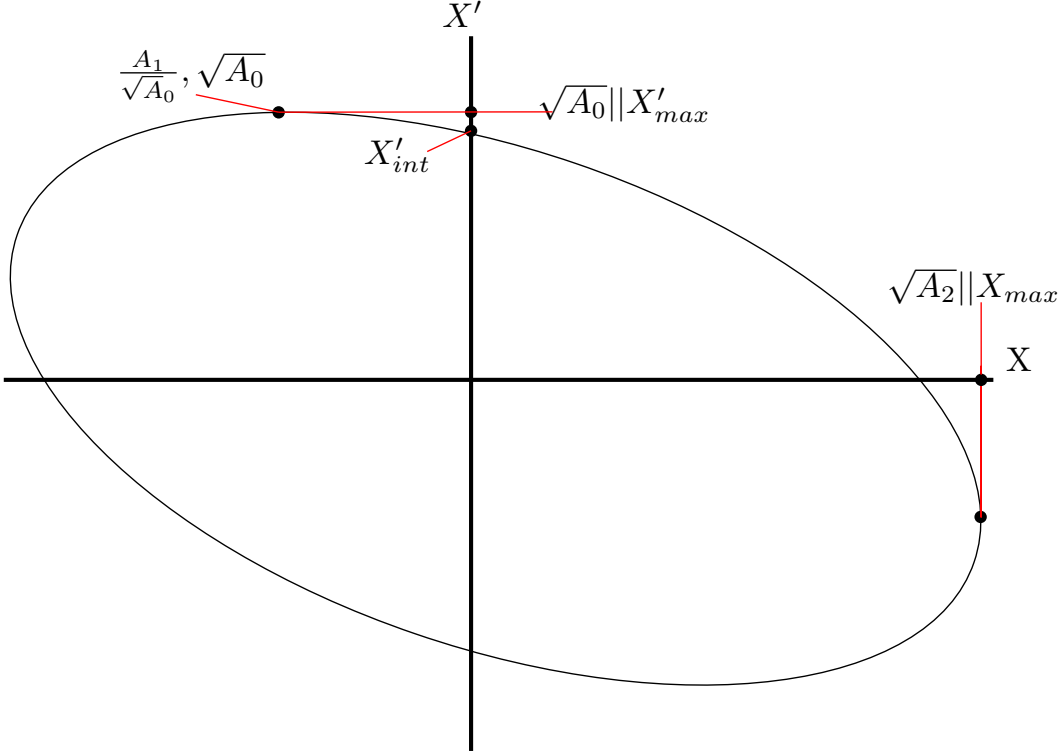


Figure 2.3: A beam ellipse of a convergent beam, illustrating some of the notation in the text. X' is the angle, and X is the spatial position. $||$ is used in the sense of “or”, to indicate two different notations for the same property.

direction of the protons. For a beam with a certain variance in its angular distribution and in its spatial distribution, the maximum possible emittance will occur when there is no correlation in spatial position and angle of travel, i.e. $A_1 = 0$. The ellipse as made out by the set of X, X' satisfying equation 2.3 is usually referred to as the beam ellipse.

Consider the beam ellipse in Figure 2.3. If the beam characterized by the beam ellipse is propagated through vacuum where the scattering power $T = 0$, all points on the beam ellipse curve would be moving strictly horizontally along the X -axis since no scattering will occur to change the direction of the protons (in Figure 2.3, all the points above the X -axis would be moving right and all points below would be moving left). In this case, it follows from Liouville’s theorem that $\frac{d\epsilon}{dZ} = 0$, or in other words that the emittance remains constant. Furthermore, the area of the ellipse may be calculated as $\pi \cdot X'_{int} \cdot X_{max}$, where X'_{int} is the point where the ellipse intercepts the X' -axis and X_{max} is the X -coordinate of the maximum spatial spread in the ellipse, which corresponds to the standard deviation of the spatial distribution in X ; this is also illustrated in Figure 2.3. It follows thus that when the beam characterized by the beam ellipse in Figure 2.3 is propagated through vacuum, it will initially converge. This is necessary because X'_{int} will initially increase, whilst Liouville’s theorem holds that the emittance must be constant; the only way for these two statements to be valid simultaneously is

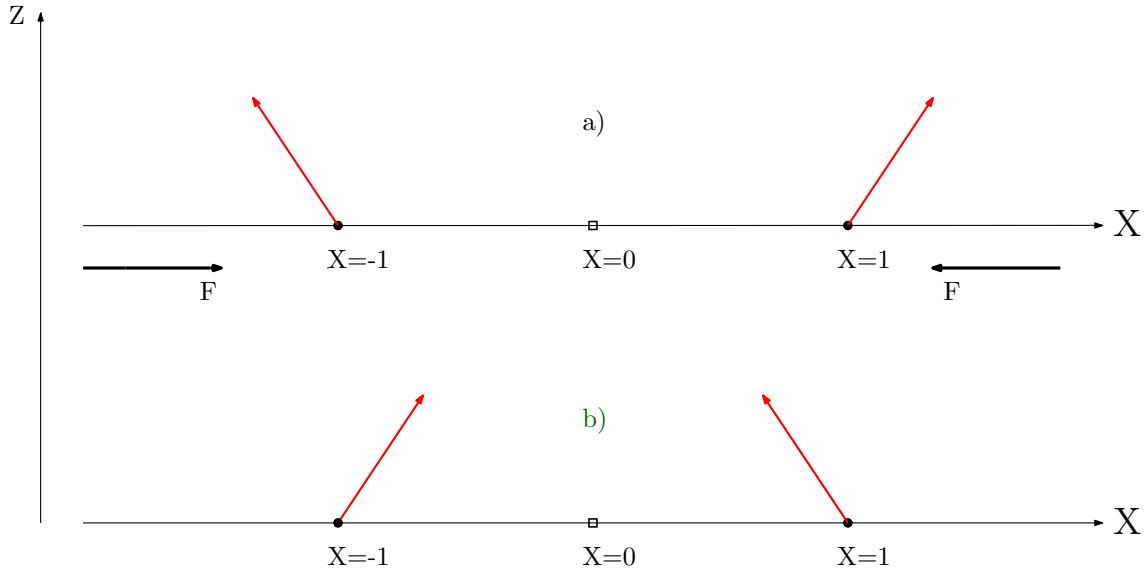


Figure 2.4: In a), two protons are traveling at a certain angle relative the Z -axis with their directions being represented by the red lines. If no steps were taken to prevent it, the spot size of this two proton beam would increase indefinitely. Suppose rather that these two protons then pass through a quadrupole in which a force Lorentz force F is applied along the X -axis, whose magnitude is proportional to the distance of the proton from the center of the X -axis. In that case, we may end up with the case as shown in b); the two protons retain their angle of travel but their spatial positions are exchanged, yielding a beam whose spot size will decrease.

for X_{max} , the standard deviation of the spatial distribution, to decrease.

A convergent beam characterized by the ellipse in Figure 2.3 may be created by the use of magnets. The simple illustration in Figure 2.4 may help in understanding how this is accomplished for a hypothetical two proton beam. The magnitude of one of the proton's X coordinate would determine the magnitude of Lorentz force F applied to it by the magnets. The direction of force along the X -axis would hold the opposite sign to the proton's X coordinate. By fine tuning strength of the magnetic field provided by the quadrupoles, it is possible to have the protons in a) exchange positions, whilst still retaining the direction of travel relative to the Z -axis. This new situation is shown in b). This two proton beam will, if allowed further undisturbed propagation, decrease its spot size. At some point however, the distance between the protons will start increasing again. The point at which the spot size of the beam is at its smallest is known as the beam waist.

The beam waist for a proton beam must, by necessity, as noted above, occur when X'_{max} intersects the X' -axis. Moreover, it is also deducible from inspection of the beam ellipse that the convergence will slow down as the beam approaches the beam waist. This happens since some protons cross the X' -axis sooner than others, and once across these protons will contribute to the divergence of the beam. As the distance from the beam waist position goes to infinity, all protons will have crossed the X' -axis,

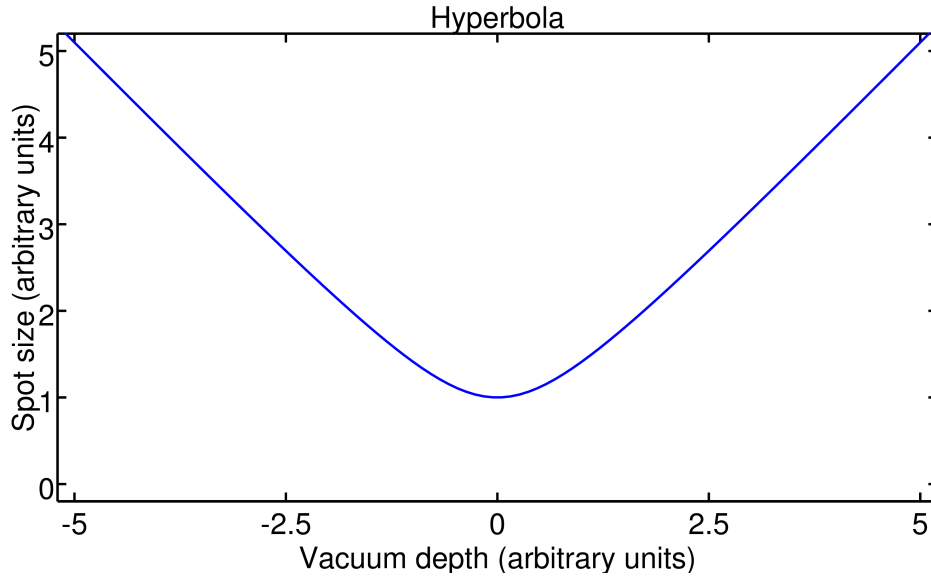


Figure 2.5: Illustrating spot size variation with vacuum depth for a convergent beam as a hyperbola in the form of Equation 2.5.

and since there is no scattering in vacuum, the protons will increase their distance to one another with a constant speed proportional to X'_{max} . At this point, the beam size as a function of air depth should be linear with a constant derivative, much like the beam modeled by Grevillot et al.

The above description of spot size variation with distance from the beam waist fits well the mathematical function known as the hyperbola, i.e. that the spot size σ_X variation with vacuum depth Z can be described as

$$\frac{\sigma_X^2}{a^2} - \frac{(Z - c)^2}{b^2} = 1. \quad (2.5)$$

where a , b and c are constants determining the the shape of the hyperbola. An example of a hyperbola with constants $a = 1$, $b = 1$, $c = 0$ is shown in Figure 2.5.

Some simplification and rearrangement of equation (2.5) yields

$$\sigma_X = a \sqrt{1 + \frac{(Z - c)^2}{b^2}} \quad (2.6)$$

Two important properties of the hyperbola are evident from Equation 2.6. First, the minimum of the hyperbola will occur when $Z = c$. Second, as $Z \rightarrow \infty$ the slope of the hyperbola approaches $\frac{a}{b}$.

By fitting equation (2.5) to the six measured spot sizes for a given energy, with a , b and c as fitting parameters, $\frac{a}{b}$ should yield a first order approximation of the angular spread of the beam for that particular energy. c might also be considered a first order approximation of the beam waist position. As noted above and illustrated in Figures 2.1 and 2.2, the uncertainty in the IC2/3 data point is larger than that for the Lynx. This difference in uncertainty warrants a weighted fit. Weights were set to $\frac{1}{U}$, where U is the uncertainty associated with the data point. This translates to a weight of 2 to the IC2/3 data and a weight of 10 to the Lynx data. The spot size at the nozzle exit was given by evaluating the fitted hyperbola at the nozzle exit Z -coordinate, yielding a first order approximation of the spot size. The emittance thus remains. Recalling Equation 2.4, A_0 , A_1 and A_2 must all be known to calculate the emittance. By setting $A_0 = \left(\frac{a}{b}\right)^2$ and

$$A_2 = a^2 \left(1 + \frac{(d-c)^2}{b^2} \right)$$

where the latter follows from squaring equation Equation 2.6 and setting $A_2 = \sigma_X^2$ and where d is the Z -coordinate of the nozzle exit (or whatever Z -coordinate described by the beam ellipse), A_1 remains to be found. The coordinate of the point in the beam ellipse corresponding to the maximum angular deviation is $\left(\mp \frac{A_1}{\sqrt{A_0}}, \pm \sqrt{A_0}\right)$. The triangle in Figure 2.6 may facilitate visualization of the situation, and from it a simple trigonometric relation may be derived to obtain A_1 . Returning to the beam ellipse in Figure 2.3, the beam waist must occur at the Z -coordinate when the protons at the $\left(\mp \frac{A_1}{\sqrt{A_0}}, \pm \sqrt{A_0}\right)$ -point reach the $(0, \pm \sqrt{A_0})$ -point, as already established. Supposing the beam waist position is known by using the c -parameter of the fitted hyperbola, the distance along the Z -axis to the beam waist is $(c-d)$; the angle at which they travel is also known, which is $\sqrt{A_0}$ relative to the Z -axis, or $\frac{\pi}{2} - \sqrt{A_0}$ relative to the X -axis. Therefore

$$\tan\left(\frac{\pi}{2} - \sqrt{A_0}\right) = \frac{(c-d)}{\frac{A_1}{\sqrt{A_0}}} \implies A_1 = \frac{(c-d)\sqrt{A_0}}{\tan\left(\frac{\pi}{2} - \sqrt{A_0}\right)} \quad (2.7)$$

Having thus found A_1 , it is possible to calculate the emittance in X . Since a corresponding method may be employed in Y , all six optical parameters may be found using the method described for the 18 energies.

The accuracy of the method thus far is limited to the extent that air can be approximated as vacuum, since it is assumed that the beam is propagated in a material characterized by a scattering power $T = 0$. Measurements however were carried out in air. The effect of this is likely that a hyperbola fit to the measurement data will yield a $\frac{a}{b}$ higher than expected, leading to an overestimation of the angular spread. This is illustrated in Figure 2.7. Two beams characterized by identical beam parameters and having been propagated through vacuum are shown after the beam waist. At absorber depth 1, one of the beams enters an air absorber and the other continues in vacuum. The blue line illustrates the latter case and how the spot size would vary in vacuum where $T = 0$; after a slight curvature in the beginning following the beam waist it approaches a constant slope some distance away from the beam waist. The red line on the other hand shows spot size variation in air where $T \neq 0$; there is a slight upwards curvature that arises due to scattering. Since the measured data will be following the red

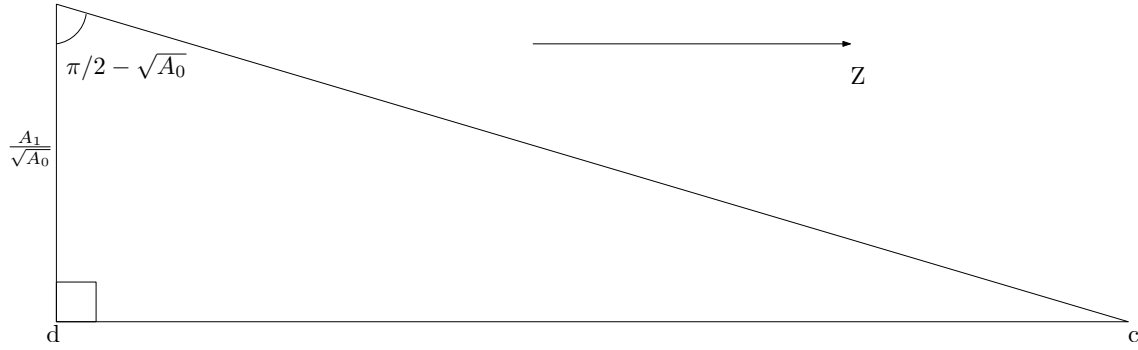


Figure 2.6: A triangle demonstrating the technique to find the emittance. The protons with maximum angle within the beam ellipse travel with an angle $\sqrt{A_0}$ relative to the Z -axis, or $\frac{\pi}{2} - \sqrt{A_0}$ relative to the X -axis, since it is perpendicular to the Z -axis. The projected distance along the Z -axis they will cover before reaching the beam waist is $c - d$. The distance to the Z -axis is $\frac{A_1}{\sqrt{A_0}}$.

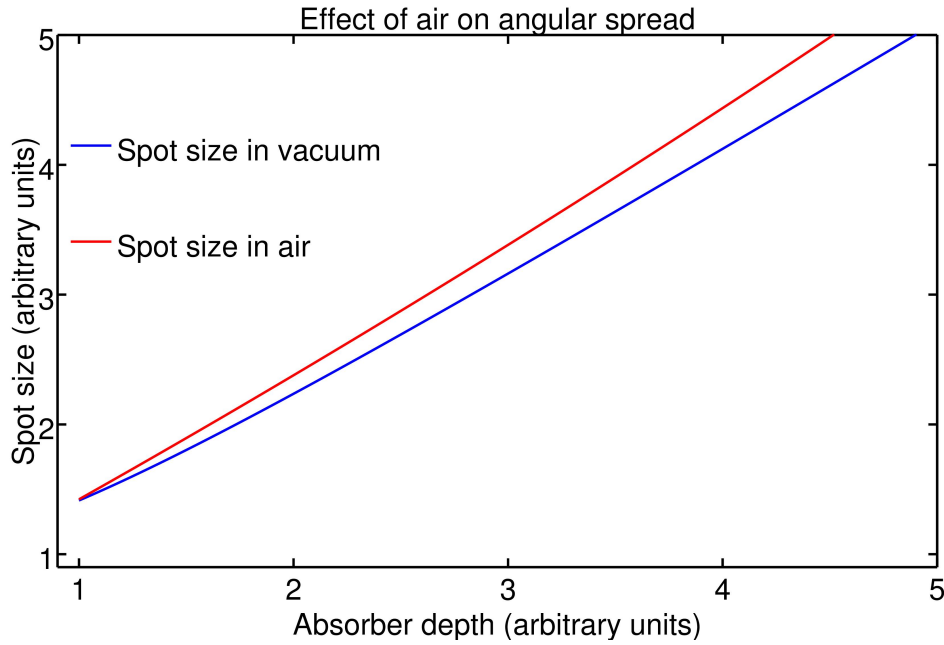


Figure 2.7: Illustrating the effect of air on the spot size variation with absorber depth after the beam waist. The red curve, corresponding to a spot size curve in air, has a slight upwards curvature, leading to an ever increasing slope; the blue line, corresponding to a spot size curve in vacuum, approaches a constant slope.

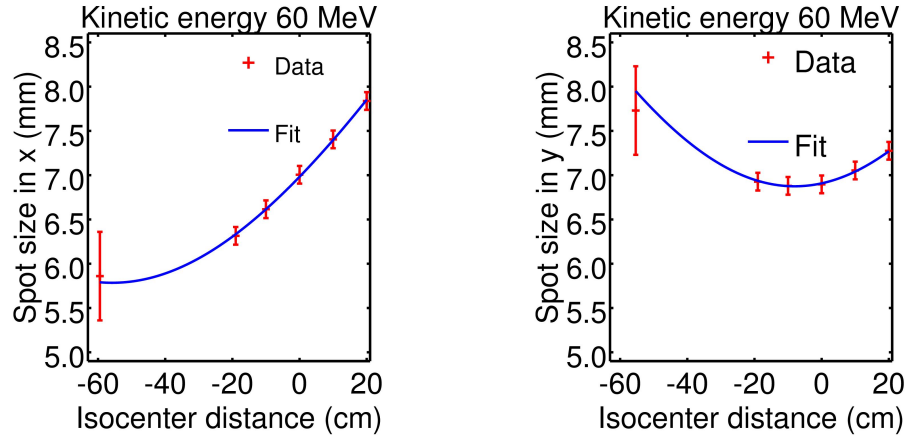


Figure 2.8: The hyperbola fits to data corrected for air for a proton beam with kinetic energy 60 MeV. The errors in the spot sizes as shown in the errorbars were provided by IBA as 0.1 mm for the Lynx data and 0.5 mm for the IC2/3 data.

curve, the fitted hyperbola will as noted above give a too large $\frac{a}{b}$ -value. To overcome this, a correction taking air into account was performed by simulation.

A simulation was run in air with the optical parameters calculated as outlined above. A second simulation, with the same optical parameters, was then performed in vacuum. In both simulations, the spot size at the position of the Lynx data points was calculated. The difference between the spot size in air and the spot size in vacuum was subsequently calculated. This difference was then subtracted from the spot sizes calculated from the Lynx data to give a reasonable estimation as to what the spot size would have been, had the beam profile measurements been carried out in vacuum. The method to calculate the optical parameters was then repeated using this modified Lynx data, and the resultant optical parameters were accepted as final.

This correction is computationally expensive. To accomplish it in a feasible time frame, the Uppsala Multidisciplinary Center for Advanced Computational Science (UPPMAX) computer cluster, provided by the Swedish National Infrastructure for Computing (SNIC), was used. 18 CPU cores were utilized for a total of 400 CPU-hours, each core simulating 5 million protons for one of the energies as described in Section 2.2 in air. Simulations in vacuum are significantly quicker and could be performed using a single CPU in a few hours for all 18 energies. Examples of the weighted least square hyperbola fits to the data corrected for air are shown in Figures 2.8 and 2.9. The complete set of plots of the fits for all energies is found in the Appendix.

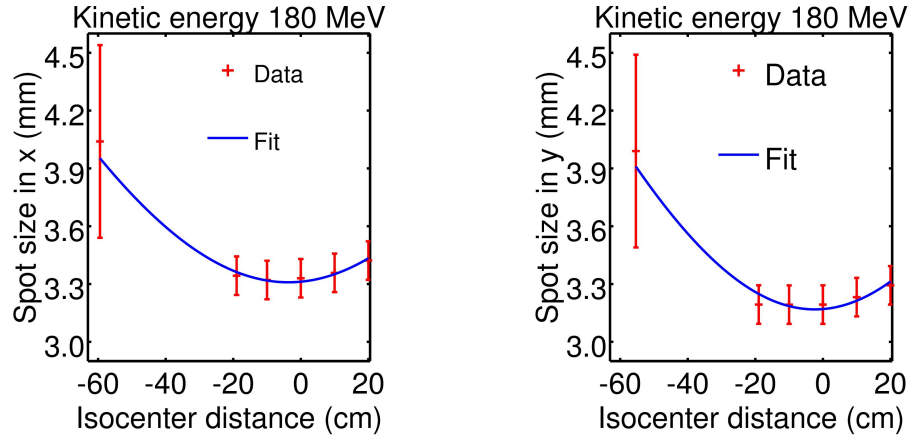


Figure 2.9: Showing the hyperbola fits to data corrected for air for a proton beam with kinetic energy 180 MeV. The errors in the spot sizes as shown in the errorbars were provided by IBA as 0.1 mm for the Lynx data and 0.5 mm for the IC2/3 data.

2.4 Energy parameters

In order to simulate a treatment plan based on log file data a method to transform the range at the nozzle entrance to kinetic energy at the nozzle exit is necessary, since the log files only provide the former and not the latter. To do this, log files for the IDD curve measurements were obtained. From these the nozzle entrance range corresponding to each curve was extracted. Following this, the distal d80 range was calculated for each measured curve. This is the range corresponding to 80% of the Bragg peak dose on the distal side of the Bragg peak. This distal d80 range value was used as an approximation of the proton range at isocenter. This range was subsequently translated into an energy using an equation supplied by IBA as follows:

$$E = e^{0.001685 \ln R^3 - 0.004901 \ln R^2 + 0.561372 \ln R + 3.464048}$$

where E is the energy and R is the distal d80 range. Having thus found the energy at isocenter corresponding to a range at the nozzle entrance, a smaller correction is necessary to account for the ~ 50 cm air gap between the nozzle exit and the isocenter. This was performed by a power law fit to the PSTAR[76] range-energy data for air. The appropriateness of using a power law to describe particle range as function of energy is generally known as the Bragg-Kleeman rule, and is still advocated in recent literature[77, 78, 79]. Justification may also be gleaned from a log-log plot of range vs energy, as shown in Figure 2.10

Using a power law of the form

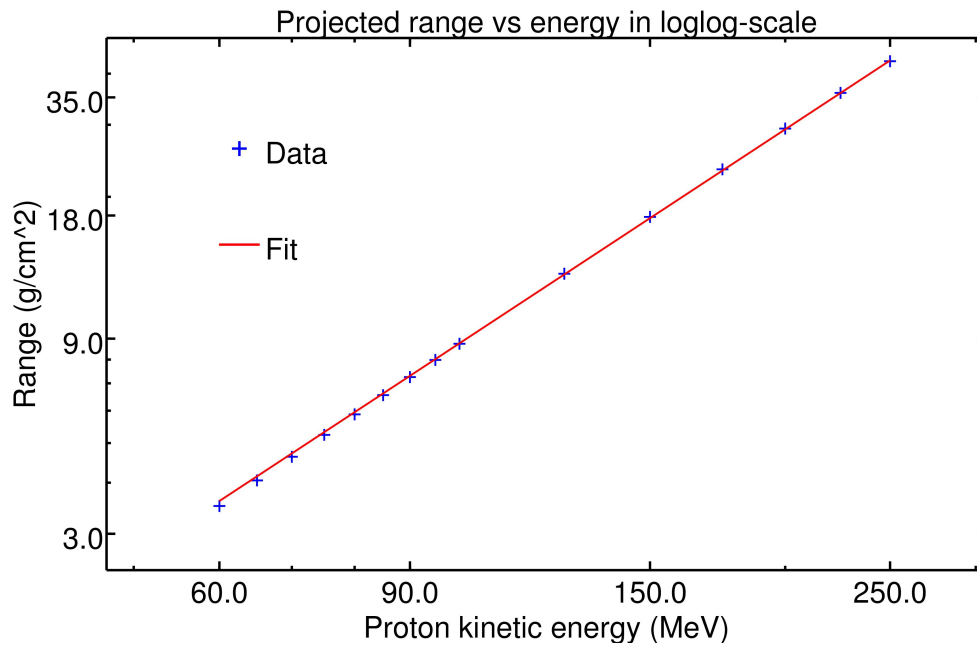


Figure 2.10: Since the data points line up on straight line on a log-log plot, a power law is a good choice to fit the data. The blue crosses are range data from NIST, and the red line is a power law (Equation 2.8) fit to the range data.

$$R = aE_{iso}^b \quad (2.8)$$

where a and b are fitted parameters thus allows accurate conversion of the energy in water at isocenter to range at isocenter in air. The energy at the nozzle exit should thus correspond to the range R at isocenter in air as given by Equation 2.8, plus an additional range r equal to the air gap length. Taking the inverse of Equation 2.8 and adding r thus yields

$$E_{noz} = \left(\frac{R + r}{a} \right)^{\frac{1}{b}} \quad (2.9)$$

which should provide the energy at the nozzle exit. Having performed this for all energies, cubic spline interpolation is used to obtain the energy at nozzle exit for an arbitrary range. The energy is thus the only parameter that does not depend on a single, fitted polynomial. The mechanics behind this will be further detailed in section 2.5.

Of the two energy parameters, the more difficult and time consuming to find is the energy spread. An algorithm was devised to automatize the process that may be summarized by the following steps. Given the kinetic energy at the nozzle exit and three initial values of energy spread

1. Calculate the range in water for the proton kinetic energy, add one centimeter to the found range and round it upwards to the nearest integer to ensure a sufficient margin. Create a water phantom with a thickness using this value. Set the dose actor resolution to score dose in planes of 0.1 mm. Adjust the position of the water phantom such that the distance from the start of the simulation until the surface of the water phantom is equal to the air gap distance from the nozzle exit to isocenter.
2. Using the geometry found in step 1., create three macro files run by GATE with the three different energy spreads. Run three simulations, one for each macro file.
3. Using the three resultant dose depth curves from GATE from step 2., compare each with the measured curve for that energy. Find the absolute value of the relative difference from the proximal d50, d80 and d90 ranges between measured and simulated curves. Also calculate the absolute value of the average relative dose deviation in the plateau region between measured and simulated curves. Sum all these deviations together for each energy spread, and fit a second degree polynomial to the sums as a function of energy spread. Find the minimum by taking the derivative of the polynomial.
4. Create three new values of energy spread, using the minimum found in step 3. as the central value, and two outer values equal to the central value ± 0.05 . Run three more simulations using these energy spreads. Repeat step 3. Then
 - (a) If new minimum found is within the interval of the three new energy spreads, accept this minimum as the best energy spread and exit.
 - (b) If new minimum found is not within the interval of the three new energy spreads, create a new energy spread interval with the new minimum as the central value and the two outer values equal to the central value ± 0.10 . Run three simulations using the three energy spreads, and move to step 3.

This method is computationally expensive in the sense of requiring at least six simulations per energy to find the energy spread. The computational expense was further increased by the fine resolution of the measurements, occasionally dropping to measurements in depth increments of 0.1 mm, thus necessitating the resolution calculated in step 1. Matching this precision whilst keeping statistical fluctuations on the simulated dose depth curve within reasonable limits, necessary for the range finding algorithm used in step 3. above, required setting some parameters (see Table 2.2) to values that significantly increased the time per simulated primary proton. To accommodate this, UPPMAX was again used. 18 CPU cores worked for some 800 CPU hours in total, running 100 000 protons per simulation to ensure an uncertainty of around 0.5% or less up until the Bragg peak. Having thus found the energy spread and the energy at nozzle exit, all parameters relevant for the beam model have been found.

The range finding algorithm in step 3 begins by first finding the data point of the dose depth curve closest to the relative dose sought (i.e. 80%). Following this, depending on if the found point has a greater or smaller relative dose than that sought, it will find the nearest data point on the other side of the sought relative dose value. It will then perform a linear interpolation between these two data points and solve the resulting linear equation for the range.

2.5 Simulations

2.5.1 GATE configuration

2.5.1.1 Geant4 related settings

All simulations were run in GATE 7.1, compiled on top of Geant4.10.01. Geant4 materials were used for all simulations as per the recommendation of the GATE collaboration group. Some studies of appropriate physics lists for proton therapy have been published[80, 81, 82]. Although there is a general agreement in using option3 of the standard electromagnetic package, there is disagreement with regards to model for nuclear interactions. Kurosui et al. suggests the precompound model or the Bertini cascade; Grevillot et al. finds the precompound model to give the best results, whereas Jarlskog & Paganetti favors the binary cascade. In running the algorithm for finding the energy spread as outlined in Section 2.4, all three of these models were tested for a single energy; no model of the three was found to yield results substantially different from another, and ultimately the precompound model, combined with the binary cascade (see below), was chosen.

ICRU49 gives a value of the mean excitation energy as 75 ± 3 eV[83]. The Geant4 collaboration group, in order to better accommodate carbon ion transport, set the excitation energy to 78 eV[84, 85] for the G4_WATER material. For all simulations, the mean excitation energy for G4_WATER was set to 76.5 eV, which was found to give the best fit to the measured projected ranges. As a base for the physics list, the modular QGSP_BIC_EMY_HP was called, meaning the standard electromagnetic package with option3 for electromagnetic processes was used, as well as the HP (high precision) package for neutron modeling. The precompound model was used for nuclear interactions up until 170 MeV, after which it is no longer applicable; for higher energies the binary cascade was used. Tables 2.2, 2.3 and 2.4 list parameter values different from default ones for the various simulations, with Table 2.1 holding the default values.

Table 2.1: Default electromagnetic package, option3 parameters.

Parameter	Value
Range cut for protons electrons, positrons and gamma rays	1 mm
Linear loss limit for protons and electrons	0.01
dE/dx bin range	100 eV - 100 TeV
Number of dE/dx in bin range	220

Table 2.2: This table contains the non-default value parameters for the simulations run to find the energy spread.

Parameter	Value
Range cut for protons, electrons, positrons and gamma rays	0.01 mm
Linear loss limit for protons and electrons	0.0001
dE/dx bin range	1 eV - 1 GeV
Number of dE/dx in bin range	1200
Maximum step size in water phantom	0.04 mm

Table 2.3: This table contains the non-default value parameters for the simulations run to perform the gamma index test.

Parameter	Value
Range cut for protons, electrons, positrons and gamma rays	0.1 mm
Linear loss limit for protons and electrons	0.001
dE/dx bin range	1 eV - 1 GeV
Number of dE/dx in bin range	1200
Maximum step size in water phantom	0.4 mm

Table 2.4: This table contains the non-default value parameters for the simulations run to find the optical parameters.

Parameter	Value
dE/dx bin range	1 eV - 1 GeV
Number of dE/dx in bin range	1200

In general, increasing the number of dE/dx bins increases simulation precision with only a minimal increase in simulation time for simple geometries; for more complicated geometries including a large number of materials the increase may not be negligible. For the energy spread simulations, the dose was scored in 0.1 mm thick planes. Since the stopping power is almost constant throughout the clinical energy range as illustrated in Figure 1.4, significant fluctuation in the dose may be observed in the dose scored in each plane in the plateau region and well into the proximal rise of a Bragg curve. This introduces difficulties for the range finding algorithm as described in Section 2.4. In an attempt to reduce these fluctuations, a maximum step size was introduced in the water phantom that would force at least one full step to take place entirely within a plane.

This maximum step size could be relaxed somewhat without introducing unnecessary fluctuation for the gamma index simulations, where each voxel was $0.95 \times 0.95 \times 1 \text{ mm}^3$ in size. For the optical parameters, the entire simulation geometry consisted of air and vacuum. Dosimetrical precision was of little concern, and thus the parameters could be kept at default values.

2.5.1.2 GATE beam profile simulation geometry

To obtain beam profiles in simulations, the phase space actor was used instead of the dose actor. The world volume material was set to G4_AIR. Inside the world volume, six volumes, also of material G4_AIR, were constructed. The last five were positioned so as to have their proximal surface coincide with the air depth positions of the Lynx data measurements; the first one was positioned with its proximal entrance at the nozzle exit. To each of these six volumes, a phase space actor was attached. The phase space actor by default registers the position of all particles entering it. Starting the simulation at the nozzle exit, the phase space actor failed to register a significant portion of the protons in the first phase space volume. For this reason, a 0.5 mm vacuum gap was introduced between the starting point of the simulation and the first phase space volume entrance. The simulation geometry is illustrated in Figure 2.11.

The output from each phase space actor was provided as a .root-file. It was thus imported into ROOT and the same method to calculate spot sizes as detailed in section 2.2 was utilized. It was found that electron contamination had a significant impact on the spot size obtained. The Lynx is specified as being sensitive to electrons in the range 4-25 MeV. Since the maximum electron energy protons at Skandionkliniken are able to generate is $\sim 0.55 \text{ MeV}$, and the distribution of secondary electrons is proportional to $\frac{1}{E^2}$, filters were introduced into the simulation in order to make the phase space actor only consider protons.

2.5.1.3 Proton beams

Individual Pencil beams, used in the IDD curve and beam profile simulations, were simulated using the PencilBeam source type. Pencil beam properties, along with the start position, are specified in this source type using the eight parameters described in Section 2. In addition to these eight parameters, a beam may be set as either convergent or divergent in x and y respectively. Information on whether the beam is convergent or divergent is provided by the sign of $(c-d)$ -term in Equation 2.7; if it is negative, the beam is divergent and if it is positive the beam is convergent. However, since A_1 is squared in equation 2.4, the sign is not contained in any of the eight parameters of the beam model, wherefore it must be set separately.

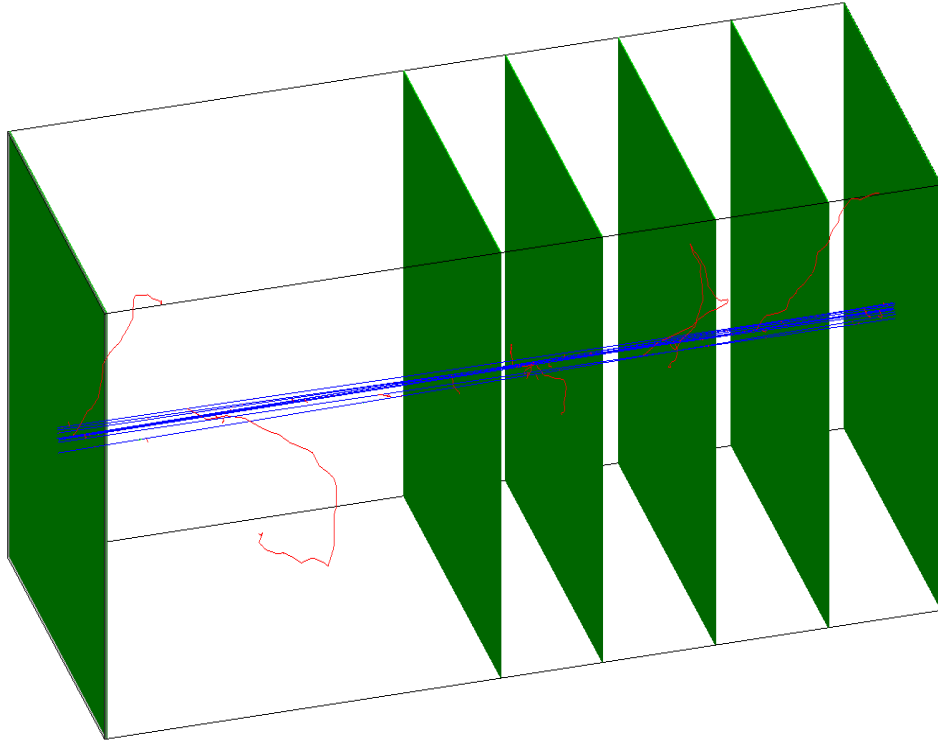


Figure 2.11: The simulation geometry for the beam profile simulations. The world volume is delineated by the black lines and the phase space actor volumes are shown in green. The tracks of ten simulated protons, traveling from left to right, are shown in blue. In red are the tracks of δ -rays, ignored by the phase space actor.

Treatment plans were simulated using the TPS PencilBeam source type. Unlike the PencilBeam source type, the TPS PencilBeam source type cannot handle beams with different convergence/divergence settings in x and y . Rather, the beam must be set as convergent or divergent for the entire treatment plan in both dimensions. A glance at Figure 2.8 seems to indicate a clearly divergent beam in x , if one were to use isocenter -19 cm as the simulation starting point whereas in y , it seems to be convergent. By having the simulation starting point further upstream, at the nozzle exit, it was possible to ensure the beam was convergent or nearly convergent for all energies in both x and y .

The TPS PencilBeam source type is dependent on two input files: the source file and the plan file. The latter contains the treatment plan in the form of a list of spot positions and weights, as well as the energy for each layer. The basic method to transform the log files to a GATE plan file is detailed in Section 2.5.2. The source file consists of the eight polynomials that, evaluated for the energy given for each layer in the plan file, gives the eight parameters that describe the proton pencil beam.

2.5.2 Log file to GATE plan file conversion

During the course of an irradiation, the IBA beam delivery system records the current value of a wide variety of parameters throughout the entire beam line. These log files do not store the mean kinetic energy at isocenter of the beam, but rather the range in water at the nozzle entrance through use of an internal energy-range conversion table. In order to serve as a basis for simulations, this had to be translated into a kinetic energy at the nozzle exit. The method employed is detailed in Section 2.4. Having performed this for all 18 energies, cubic spline interpolation was used to provide the energy at nozzle exit for arbitrary ranges. This energy is then used for evaluating the eight polynomials stored in the GATE source file; the source file also contains the nozzle exit to isocenter distance, as well as the virtual source positions. The polynomials describing the optical parameters and the energy spread used were polynomials fits to the data as detailed in the Sections above; the mean energy polynomial however was a simple first degree polynomial, with the coefficient set to 1 and the constant to 0.

The log files are originally stored in an IBA proprietary format. IBA staff at Skandionkliniken subsequently converted the log files into a comma separated values text format. To ensure speed and efficiency in handling the data, only the data relevant for the construction of a GATE plan was extracted from the log files.

The pertinent parameters to reconstruct a treatment plan are the spot positions, the spot weights in terms of MUs, the energies for each layer and the gantry angle. The spot position at IC2/3 and the charge generated in the monitor chamber are logged every 250 μ s. Whenever the beam is switched off, a value of -10000 is recorded for spot position. Whenever the beam is switched on, positive values are given. When a spot is complete, -10000 is again recorded until the next spot begins. For each spot, an average was calculated over all positions logged for the duration of the spot. All charge generated in the monitor chamber for the duration of the spot was summed. The collected charge during a spot was multiplied with a correction factor given in the log files, and then divided by a constant $a = 3.9 \cdot 10^{-9} \text{C}$ to yield the MUs for that spot; the value thus given is associated with an uncertainty of 3-5%, according to IBA.

The log files store spot positions at the location of the IC2/3 strips only. These are located at isocenter at isocenter -59 cm in x and isocenter -55 cm in y respectively. Since treatment plans are generally characterized by spot positions at isocenter, as is the GATE input file, the spot positions at IC2/3 must be projected forward to isocenter. For this purpose, the virtual source positions were

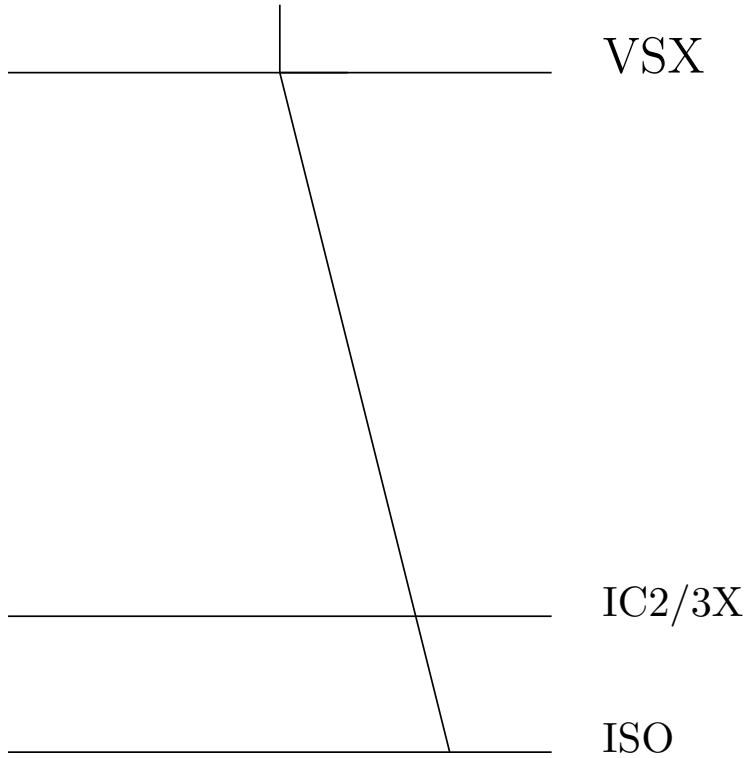


Figure 2.12: VSX=virtual source position in x , IC2/3X=position of IC2/3 reading of the spot position x -coordinate, ISO=isocenter. Since the x coordinate of the spot position at VSX and IC2/3X is known, it is possible to fit a first degree polynomial through these and extrapolate, yielding the x -coordinate at isocenter. The same method is used in y .

used. Assuming $x = 0$ and $y = 0$ in the IC2/3 coordinate system at the virtual source position in x and y respectively, it is possible to fit a first degree polynomial to the two data points in x and y , and by extrapolation it is possible to obtain the spot position at isocenter. The method is depicted in x in Figure 2.12. Due to the limited resolution of IC2/3, the spot position coordinate is, as is the spot size, subject to an uncertainty of ± 0.5 mm. Assuming a negligible uncertainty in the virtual source position, this projects to an uncertainty of ± 0.72 mm uncertainty at isocenter in x ; for y , the uncertainty is ± 0.68 mm. Adding the uncertainty in the x and y in quadrature leads to a total uncertainty in the spot position of ± 1.00 mm.

A current limitation in the log file to GATE input file code written to perform the conversion is that it can only handle a single field. Adding multiple field capabilities will be left to future work.

2.6 Beam model validation

To validate the beam model, comparison with measured data is necessary[86]. The methods employed for this purpose will be presented in the following subsections.

2.6.1 Optical parameters

After having obtained a set of optical parameters for each of the 18 energies, polynomial fits were performed. Each polynomial was evaluated for the 18 different energies to obtain 18 sets of optical parameters. A GATE macro file was created for each of the 18 sets using its parameters as input for the PencilBeam source type. 400 000 protons were simulated for all 18 sets using UPPMAX, requiring in total some 40 CPU hours. Spot sizes were calculated as detailed in Section 2.2.1. Maximum and mean deviations for each of the Lynx depths were subsequently calculated.

2.6.2 Energy parameters

As for the optical parameters, having found 18 sets of energy parameters, these were subjected to polynomial fits and evaluated to create 18 GATE macro files. Each GATE macro was run on UPPMAX using 100 000 protons per simulation, requiring about 60 CPU hours. Comparisons between the measured and simulated IDD curves were performed by comparing distal and proximal d50, d80 and d90.

2.6.3 MatriXX measurements

As further validation, a fresh set of measurements were performed that would allow testing the performance of the beam model against 3D dose distributions. In the following sections following established terminology the reference distribution will refer to the measured dose distribution and evaluated distribution will refer to the simulated distribution.

2.6.3.1 Hardware

Dose distribution measurements were carried out using the MatriXX, a 32x32 array of plane parallel ion chambers. The ion chambers in the MatriXX have a diameter of 4.2 mm and a height of 2 mm. With the distance between chambers at 7.619 mm, only part of the active measurement area of 24.4x24.4 cm² is sensitive to the incident proton beam.

The MatriXX was used in the IBA Digipant water phantom, a slightly smaller water phantom than the BluePhantom and dedicated for use with the MatriXX, allowing the latter to be accurately positioned at different depths. Since the Digipant wall and the outer protective layer of the MatriXX have a certain thickness, the water equivalent thickness (WET) depth was used rather than the geometrical depth in the Digipant. To allow the IBA OmniPro software that was used during the measurements to move the MatriXX in the Digipant and to convert from geometrical depth to IBA WET depth, a known WET depth for one geometrical depth must be entered. IBA supplied a WET depth as 102.6 mm for a geometrical depth of 100 mm.

Table 2.5: Parameters for the measured treatment plans. The energy interval gives the highest and lowest proton kinetic energies at the nozzle exit.

Treatment plan number	1	2	3
Range (cm)	25	16	8
SOBP length (cm)	2	3	2
Energy interval (MeV)	197.32-188.27	152.06-136.43	103.71-89.19
Number of layers	4	6	8

2.6.3.2 Treatment plans

Measurements were carried out for three different treatment plans detailed in Table 2.5. All three plans were 10x10 cm² square fields in the xy -plane. Each treatment plan was repeated multiple times to allow the MatriXX to be positioned at different depths. The log files were obtained for the measurements. Since the measurement had to be repeated for each MatriXX depth position, a set of log files was generated for each treatment plan. Neglecting differences in the delivery for the same treatment plan, a single set of log files, corresponding to a single delivery with the MatriXX at a certain depth, was converted to a GATE plan file for each treatment plan. This GATE plan was then used as input for a simulation, yielding a 3D dose distribution covering the entire range of the treatment plan.

2.6.3.3 Normalization

The MatriXX following calibration at a standard laboratory is able to report dose distributions in units of mGy. GATE reports the dose to each voxel in units of Gy for the number of incident particles simulated. Since a massive amount of computing power would be necessary to simulate the actual number of protons striking the MatriXX during measurements, normalization is necessary. For normalization, the mean dose M_r of all points of the reference distribution above 80% of the max dose was calculated at the smallest measured IBA WET depth for each treatment plan where the dose gradient may be expected to be at its lowest. The same procedure with the same fraction and depth was repeated for the evaluated distribution yielding M_e . Then the entire 3D evaluated distribution for the treatment plan was multiplied with the fraction $\frac{M_r}{M_e}$.

2.6.3.4 Gamma index test

A quantitative comparison of the simulated and measured dose distribution was performed in the form of a gamma index test[87, 88, 89]. Although the AAPM TG 119[90] used the so called Van Dyk or global method, whereby the dose difference criteria is calculated relative to a single point of the reference distribution (typically the maximum dose point is used in the global method), a strong case can be made for using the local method whereby the dose difference criteria is defined relative the reference point under consideration[91]. Each reference 2D distribution was compared with the 3D simulated distribution; for the the global method, this means that the reference distribution was sought for its maximum value for each depth. Entering 3% thus as a dose criteria means 3% of this maximum value.

For efficiency a limited search method was employed whereby only a cube, centered on the reference point, with sides equal to twice the distance criteria was sought for each reference point in the evaluated distribution. All points outside this cube (and even for some within) in the evaluated distribution necessarily have a $\Gamma > 1$, which means failure. However, since

$$\gamma(\mathbf{R}_r) = \min\{\Gamma(\mathbf{R}_r, \mathbf{R}_e)\} \forall \{\mathbf{R}_e\}$$

where \mathbf{R}_r is the reference point and \mathbf{R}_e is the evaluated point, the used limited search method may not find the true value of $\gamma(\mathbf{R}_r)$ when it is greater than unity. For this reason, the true gamma distributions will not be presented, but rather what shall be referred to as semi-gamma distributions $\gamma_s(\mathbf{R}_r)$. The difference may be described formally as

$$\gamma(\mathbf{R}_r) = \gamma_s(\mathbf{R}_r) \forall \{\gamma(\mathbf{R}_r) \leq 1\}$$

$$\gamma(\mathbf{R}_r) \leq \gamma_s(\mathbf{R}_r) \forall \{\gamma(\mathbf{R}_r) > 1\}$$

Points of the reference distribution with a dose lower than 30% of the maximum dose were ignored in the gamma index test. Appropriate standard criteria for a gamma index test in proton therapy have yet to become established in the literature. For VMAT photon therapy, 3%/3mm criteria are standard with a 90% tolerance limit for the pass rate[92] or 95%[93], using the global method. Pass rates for both the global/Van Dyk (with the dose difference criteria defined relative the maximum dose in the reference distribution) and the local method was calculated for each treatment plan.

Chapter 3

Results

3.1 Optical parameters

Figures 3.1, 3.2 and 3.3 demonstrate the resulting six polynomials that followed a fit to the obtained optical parameters for the 18 different energies, as described in Section 2.3. Evaluated for a given energy at nozzle exit, they yield the six optical parameters at the nozzle exit. In Table 3.1 the maximum measured-simulated differences are presented. These were calculated by evaluating the polynomials shown in the Figures at the proton kinetic energies of the data points and taking the absolute value of the difference between this value and the value of the data point, and then finding the maximum. These six polynomials make out the optical part of the beam model. All six polynomials are of the 4th order. To compute the error bars, the error propagation formula was used with errors as provided by the covariance matrix of the hyperbola fit.

Figure 3.4 shows the results of a comparison in the form of measured-simulated spot size differences at isocenter using optical parameters as provided by the polynomials illustrated in Figures 3.1, 3.2 and 3.3. The error bars were computed by adding the uncertainties for the Lynx spot size data and the statistical fit error for the simulated spot sizes as given by ROOT in quadrature. Except for an outlier at 60 MeV in x , the beam model seems able to predict the spot size within 0.2 mm for all energies at isocenter. The outlier warrants an explanation. For 60 MeV in x , the beam waist is found somewhere in IC2/3, i.e. before the nozzle exit (see Figure 2.8). It is thus divergent. However, as noted in Section 2.5 the TPS PencilBeam source type in GATE can only simulate beams that are either convergent or divergent in both dimensions. 60 MeV in x was thus simulated as a convergent beam even though it is divergent, resulting in a smaller simulated spot size.

Table 3.1: The maximum differences between the polynomials and data points in Figures 3.1, 3.2 and 3.3 along with χ^2 and the number of degrees of freedom (ndf).

Parameter	Spot size		Angular spread		Emittance	
Dimension	x	y	x	y	x	y
Absolute max difference	0.16 mm	0.22 mm	0.18 mrad	0.22 mrad	1.87 mm mrad	6.04 mm mrad
χ^2 /ndf	47.4/13	7.88/13	10.3/13	3.14/13	25.2/13	4.90/13

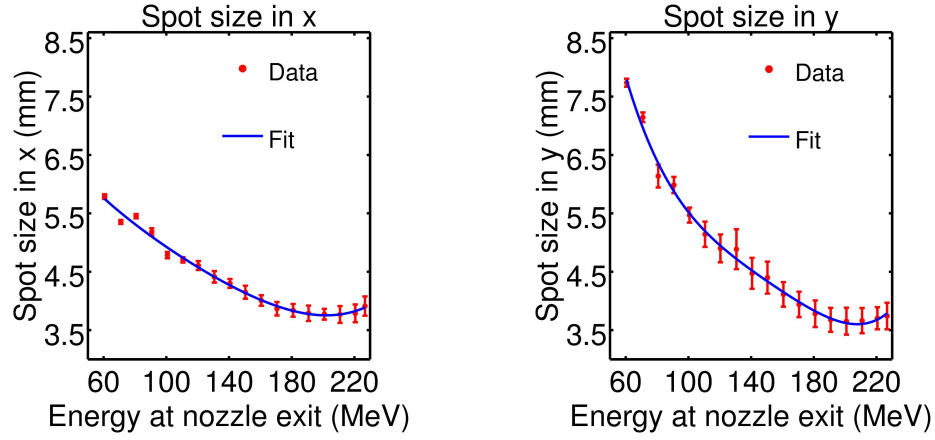


Figure 3.1: 4th order polynomial fits to the spot sizes at nozzle exit, found as described in Section 2.3 by evaluation of Equation 2.6, as a function of the energy at the nozzle exit.

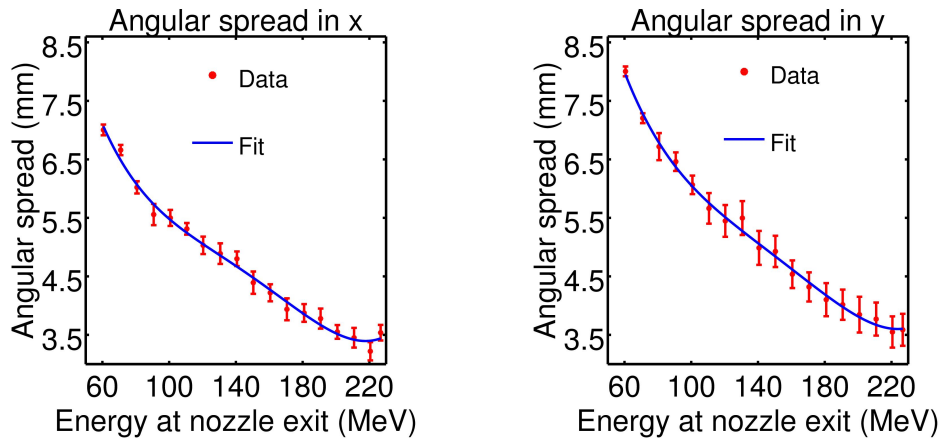


Figure 3.2: 4th order polynomial fits to the angular spread at nozzle exit, found as described in Section 2.3 by taking the $\frac{a}{b}$ -value from Equation 2.6, as a function of the energy at the nozzle exit .

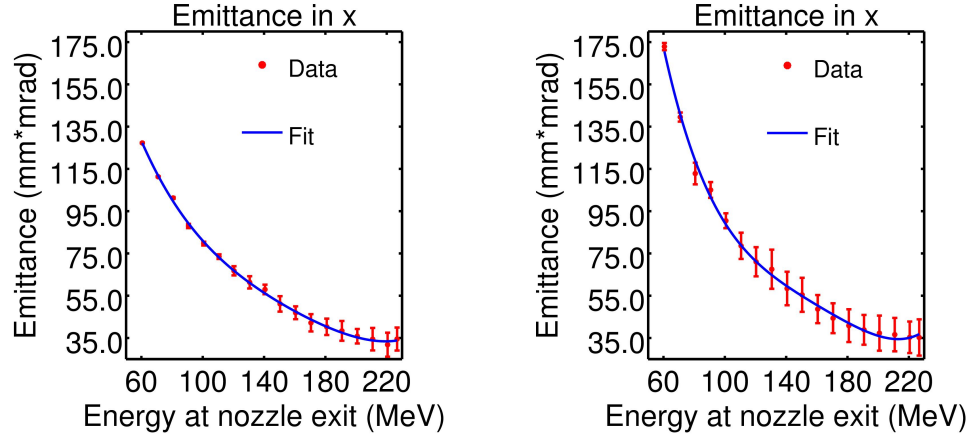


Figure 3.3: 4th order polynomial fits to the emittance at nozzle exit, found by applying Equation 2.4 as described in Section 2.3, as a function of the energy at the nozzle exit.

Table 3.2: The goodness of fit indicators of the simulations using the optical parameters as given by the beam model.

Statistic	x-dimension					y-dimension				
	Iso-19	Iso-10	Iso	Iso+10	Iso+20	Iso-19	Iso-10	Iso	Iso+10	Iso+20
Mean difference (mm)	0.01	-0.01	-0.03	-0.02	0.01	0.02	-0.02	-0.03	-0.03	0.00
Absolute max difference (mm)	0.20	0.26	0.33	0.29	0.29	0.28	0.24	0.19	0.23	0.23

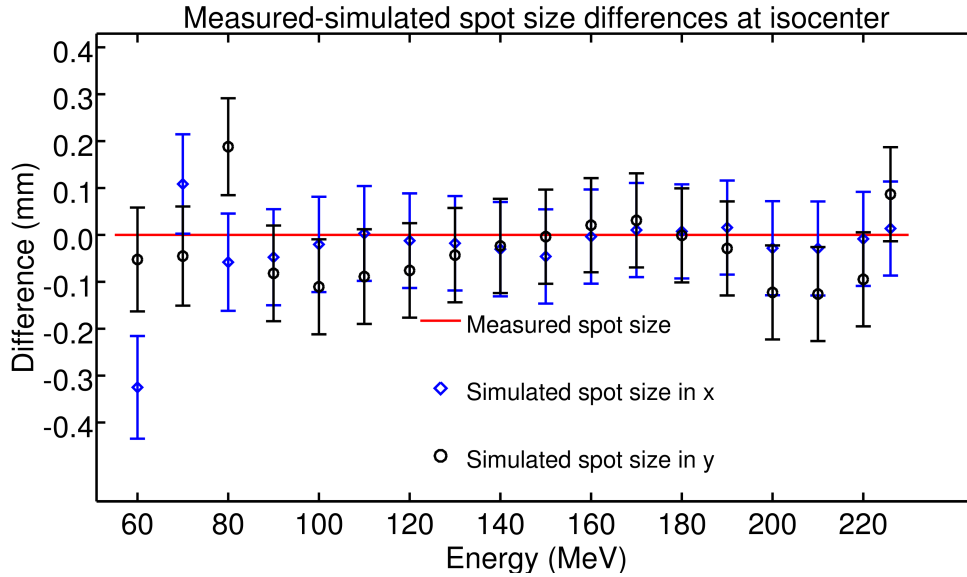


Figure 3.4: The measured-simulated spot size differences at isocenter. The errorbars were computed by adding the uncertainties in the Lynx spot size data and the statistical fit error for the simulated spot sizes in quadrature

A summary of the data for isocenter and the other air depths is found in Table 3.2. Overall, the accuracy provided by with which the beam model is able to predict the spot size at a given depth is sufficient for clinical applications and thus validates the optical part of the beam model.

3.2 Energy parameters

Figure 3.5 illustrates the cubic spline interpolation used to convert the range at nozzle entrance provided by the log files to kinetic energy at the nozzle exit, used in the simulations. As noted previously in Section 2.5.2 it effectively replaces the mean energy polynomial of the beam model. The polynomial for the energy spread as a function of energy at the nozzle exit is shown in Figure 3.6. As an assessment of the uncertainty associated with the polynomial, the maximum deviation from a point to the polynomial curve is 0.026 MeV.

Figures 3.7, 3.8 and 3.9 are examples of simulated vs measured IDD curves, where the simulated curves use the kinetic energy as found by the cubic spline interpolation and with an energy spread as found by the algorithm detailed in section 2.4.

As a summary of the results for the energy part of the beam model, Table 3.3 houses the maximum measured-simulated range differences. The differences for all energies and ranges are plotted in Figure 3.10. The ranges d50, d80 and d90 are the ranges corresponding to relative doses of 50%, 80% and 90% of the maximum dose, i.e. the Bragg peak dose. Since there is a 50%, 80% and 90% relative dose point on both sides of the Bragg peak, these will be distinguished by reference to the proximal

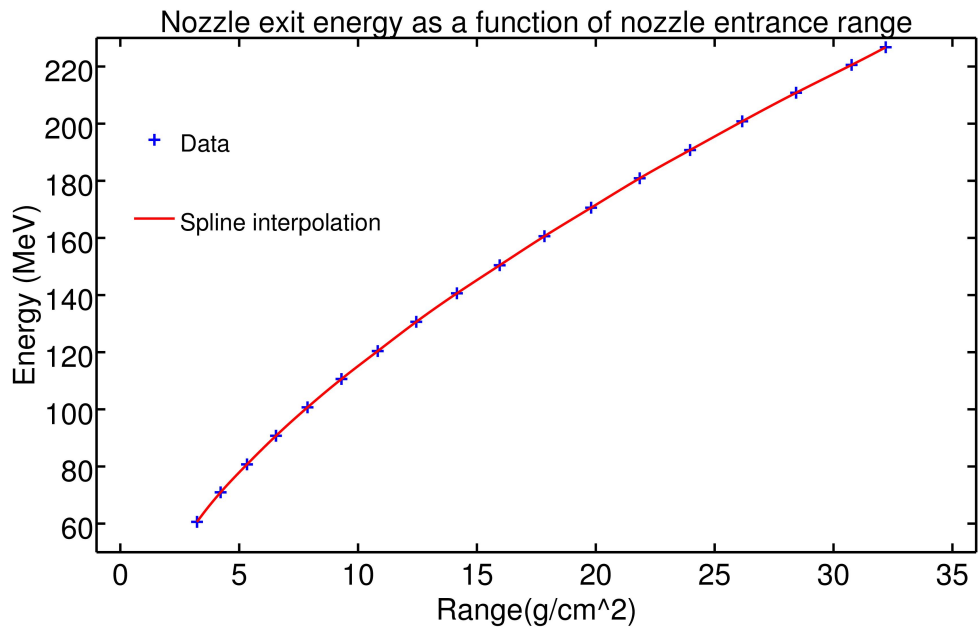


Figure 3.5: Spline interpolation of range at nozzle entrance vs energy at nozzle exit data.

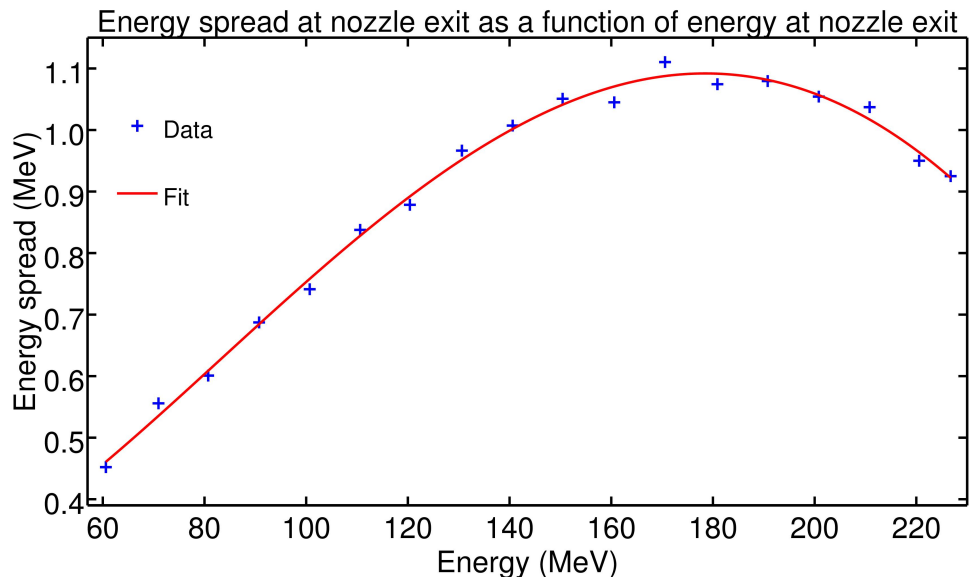


Figure 3.6: The energy spread beam model polynomial. The polynomial is 4th order.

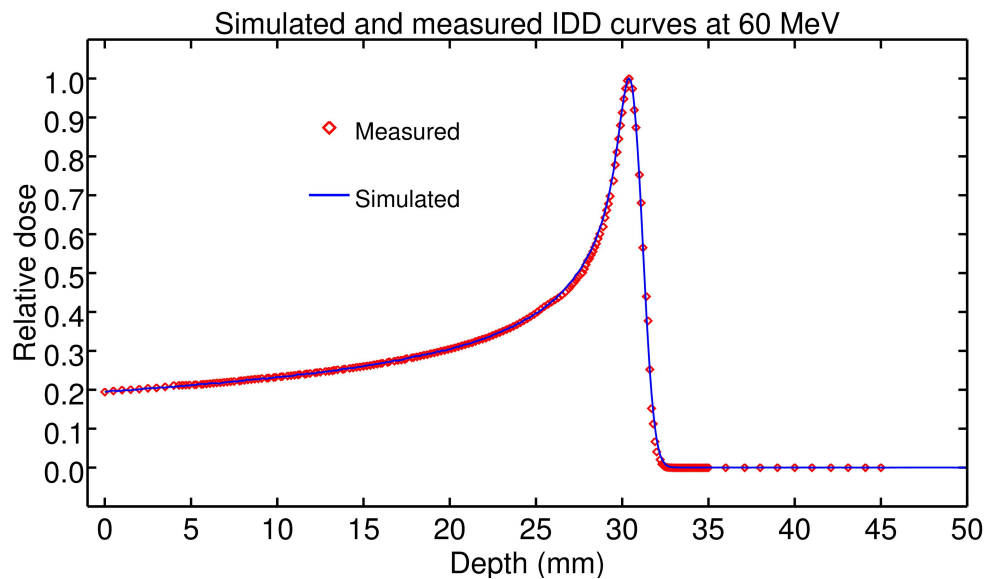


Figure 3.7: The measured and simulated curves for a 60 MeV proton beam in water.

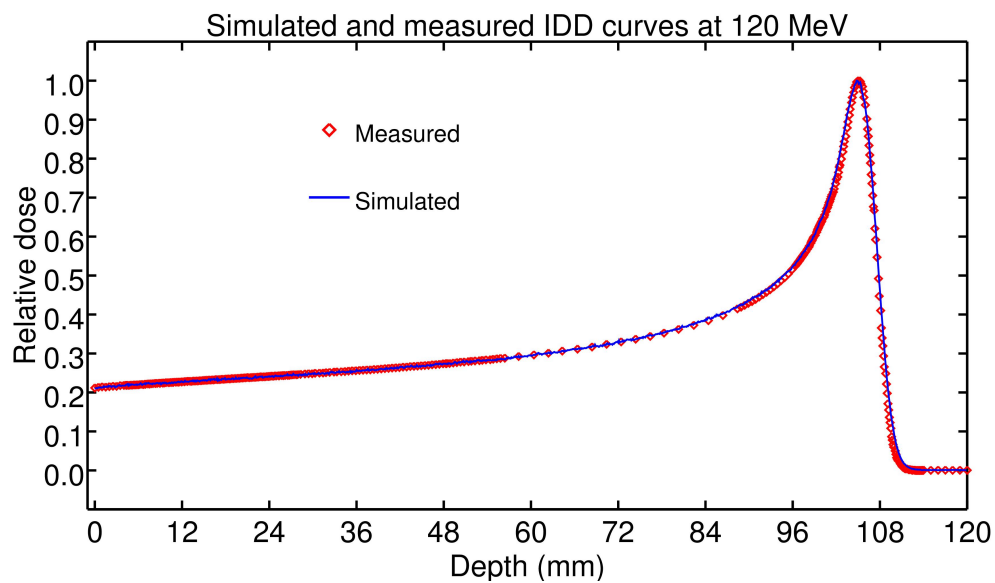


Figure 3.8: The measured and simulated curves for a 120 MeV proton beam in water.

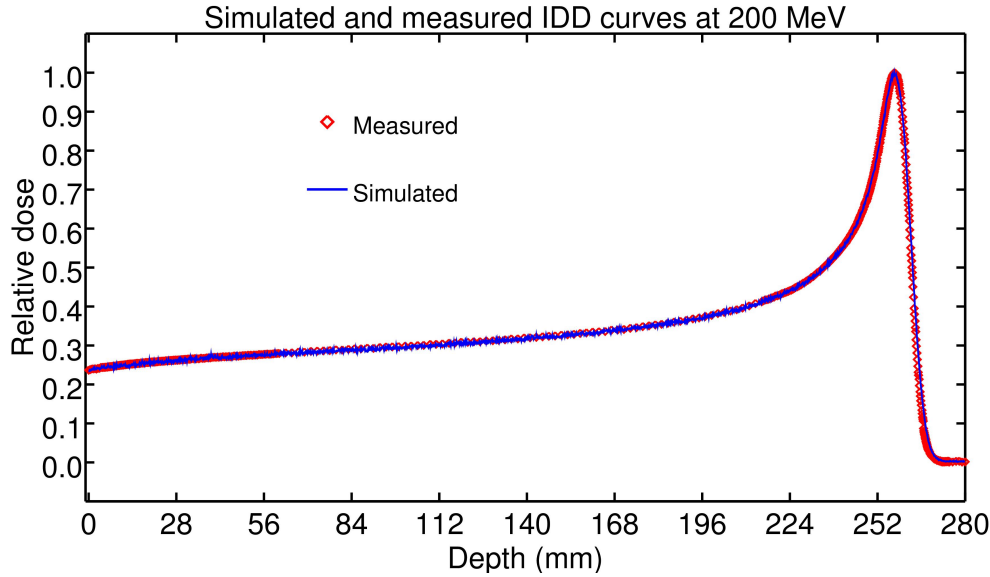


Figure 3.9: The measured and simulated curves for a 200 MeV proton beam in water.

Table 3.3: The absolute maximum differences in the proximal and distal d50, d80 and d90 ranges between the measured and simulated dose depth curves. In brackets are the energies at which these maximum differences occur.

Proximal			Distal		
d50 (190 MeV)	d80 (220 MeV)	d90 (220 MeV)	d50 (226 MeV)	d80 (210 MeV)	d90 (210 MeV)
0.86	0.61	0.52	0.50	0.18	0.10

or distal d50, d80 or d90 ranges. The distal d80 as noted in Table 1.1 is a good approximation of the projected range and thus relatively insensitive to the energy spread; the maximum deviation at -0.18 mm indicates that the method used to find the energy at the nozzle exit is accurate. Overall, only for five cases in Figure 3.10 is the absolute value of the difference greater than 0.5 mm.

3.3 Gamma index test

Due to a serious set up error the 16 cm range plan measurements were discarded. For the other two plans, henceforth referred to as the high and low energy plan, it was found that the MatriXX distribution was shifted relative to the simulated distribution. The latter geometry assumes a perfect experimental set up. An example of a semi-gamma distribution illustrating the shift is found in Figure 3.11.

A translation of the high and low energy measured distributions significantly increased the percentage of points that passed the set criteria. It was found that in order to yield high pass rates, the shift in x had to be increased with increasing depths. This would be consistent with a set up error where a

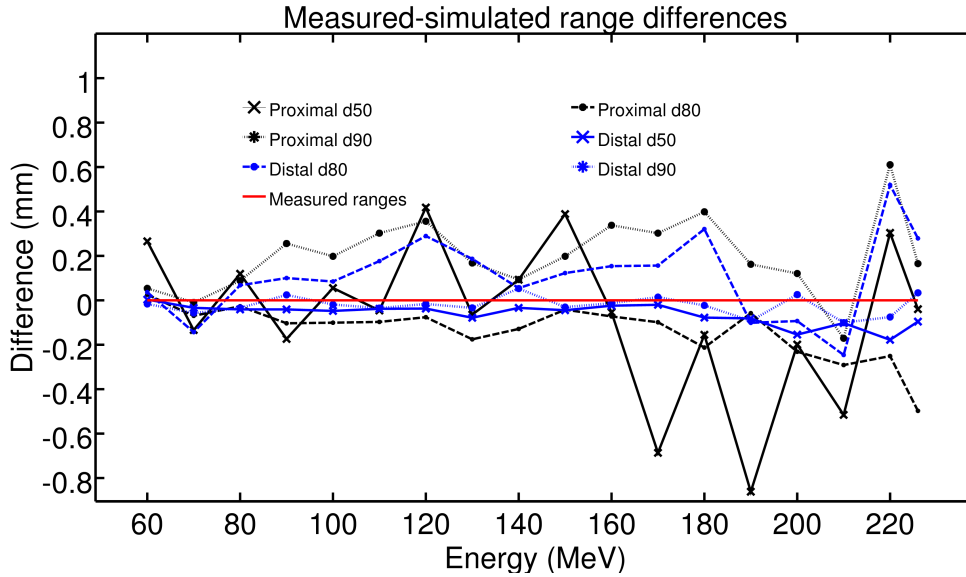


Figure 3.10: Measured-simulated range differences at the various ranges in water.

certain rotation around the y -axis was introduced. The assumed set up error is illustrated in Figure 3.12. It was found that assuming an angle of rotation around the y -axis of 0.9 degrees, and a constant shift in x of -0.1 mm, along with a constant shift in y of +1.8 mm, consistently predicted translations that provided higher pass rates throughout the range of both treatment plans.

Furthermore, a shift was found in the z -direction. For both treatment plans, the measured data seems to indicate a range greater than the simulated data. This is shown for the higher energy plan in Figure 3.13. Subsequent measurements performed by the commissioning physicists at Skandionkliniken indicated that the standard IBA WET value used for the geometrical to WET depth transformation is exaggerated, i.e. that the entire measured dose depth curve should be shifted to the left. For both the high and low energy measured curve, by shifting the measured curve 2 mm to the left brought it in line with the simulated curves.

The semi gamma distribution for the same simulated depth as in Figure 3.11, with the 2 mm subtracted from the depths of the MatriXX distributions, and with the translations in x and y as described above, is illustrated in Figure 3.14.

In Figures 3.15 and 3.16 the pass rates against depth plots are shown. Pass rates for both the global and local method are presented. In general, the minimal pass rates occurs at small depths; once passed that, the global method is consistently yielding pass rates above the 95% limit, and at all depths for both plans above the 90% limit. The local method struggles with the 90% limit at the shallow depths, but following an initial rise consistently stays above the 90% limit and fluctuates around the 95% limit. As a measure of the efficiency of the gamma index code using the limited search method, a MatriXX and a simulated distribution comparison took on average two seconds to complete.

To provide a sense of the distribution of $\gamma(\mathbf{R}_r)$, $\gamma_s(\mathbf{R}_r)$ -distributions were collected for each depth for both treatment plans and for both the local and global methods. They were subsequently binned to

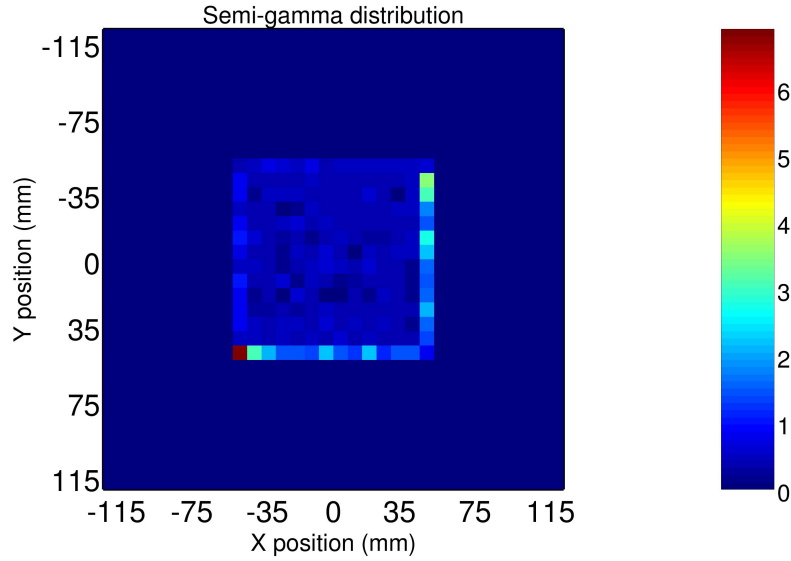


Figure 3.11: The darkest shade of blue, surrounding the square of lighter shades of blue are points of the MatriXX receiving less than the set 30% threshold of the maximum dose. The two rightmost and down-most lines are lit up, indicating that the most severe failures are concentrated in these two regions and possibly resulting from a shift in the distribution position relative the simulated. The showed distribution is for a IBA WET depth/water geometrical depth of 68.8 mm for the high energy treatment plan.

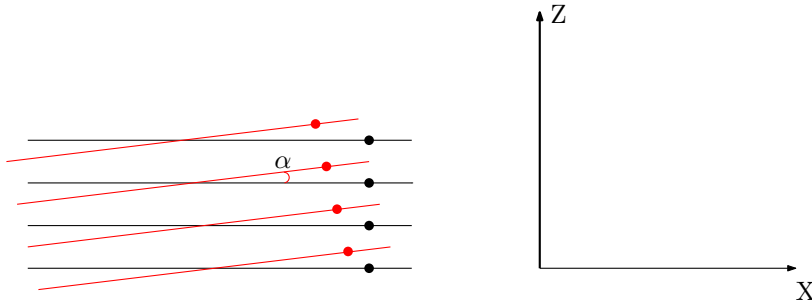


Figure 3.12: A simple schematic overview of the assumed set up error. The black lines indicate the ideal position of the MatriXX and the simulated coordinate system, with the beam traveling along the positive z -direction. The black dots show positions with identical x -coordinates. Introduced during set up of the MatriXX, a certain angle of rotation α around the y -axis perpendicular to the plane of the image of the Digiphot would cause the MatriXX to take on positions indicated by the red lines, yielding an increasing magnitude of the shift along the x axis with depth. In this set up coordinate system, red dots indicate points with identical x coordinates.

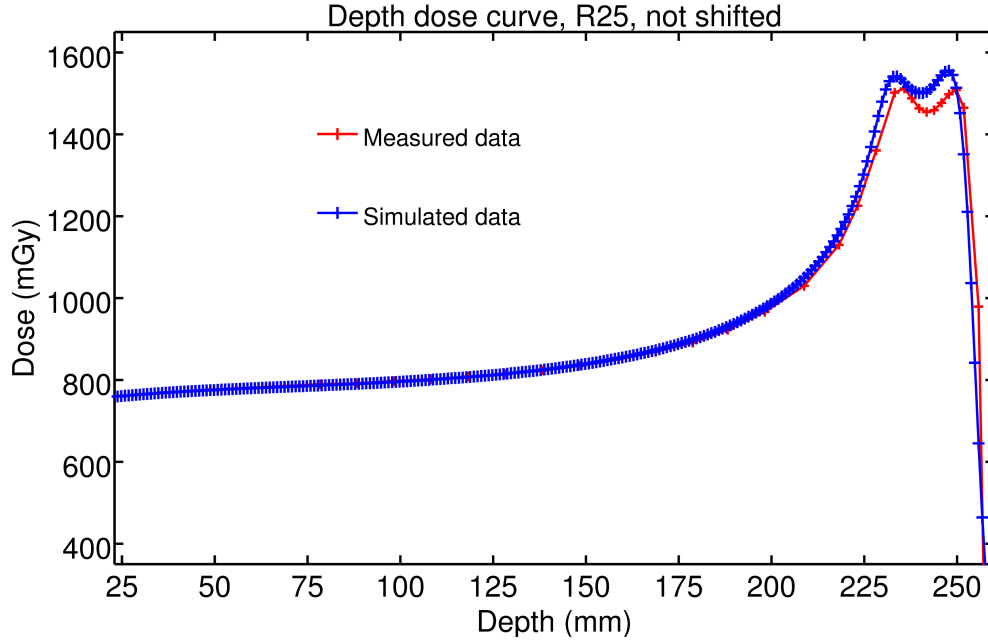


Figure 3.13: An unshifted dose depth curve for the high energy, 25 cm range treatment plan. At the normalization depth, the pixels with a dose greater than 80% of the maximum depth were found. Using the voxels with the same coordinates as these a mean was calculated for each depth. The points in the curves represent these mean values. The depth is IBA WET depth for the measured curve and geometrical water depth for the simulated curve. The spacing between points of the simulated curve was 1 mm at all times; for the measured curve, it was 1 cm. In the Bragg peak region it decreased to 2 mm. The apparent increase in the dose at the very end of the measured curve is noise.

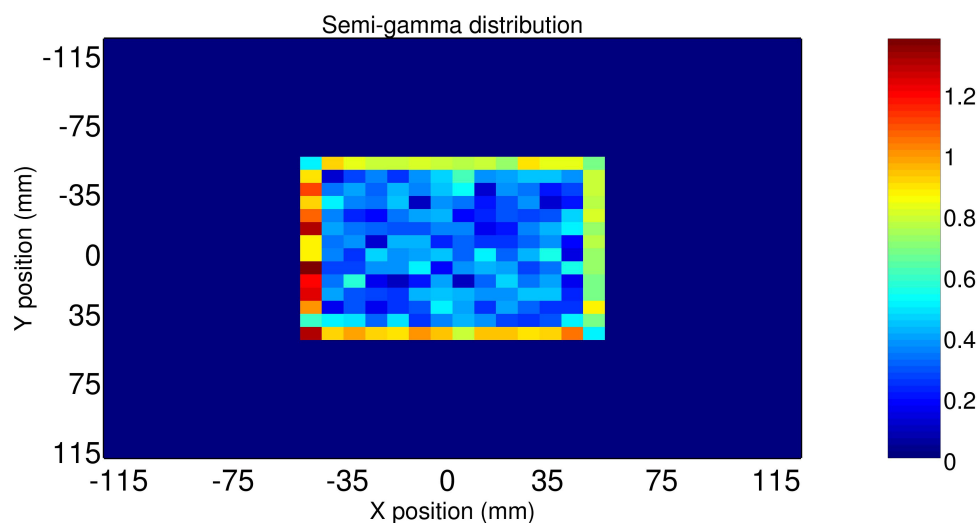


Figure 3.14: Semi-gamma distribution for the same data as in Figure 3.11, having now applied all appropriate translations.

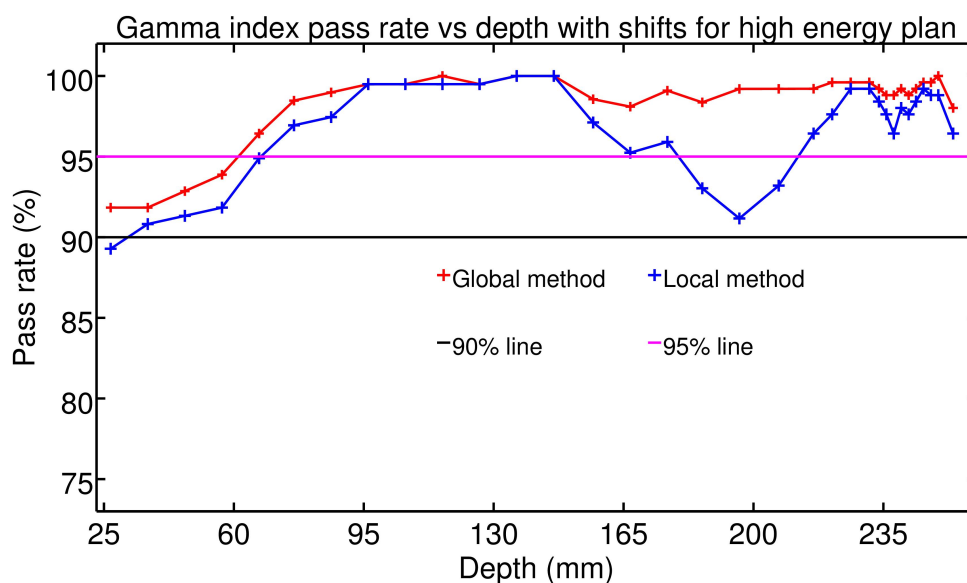


Figure 3.15: The gamma index pass rate vs depth for the high energy plan. Lines are drawn through each data point to facilitate visualization only. 90% and 95% lines are likewise drawn showing the common tolerance limits.

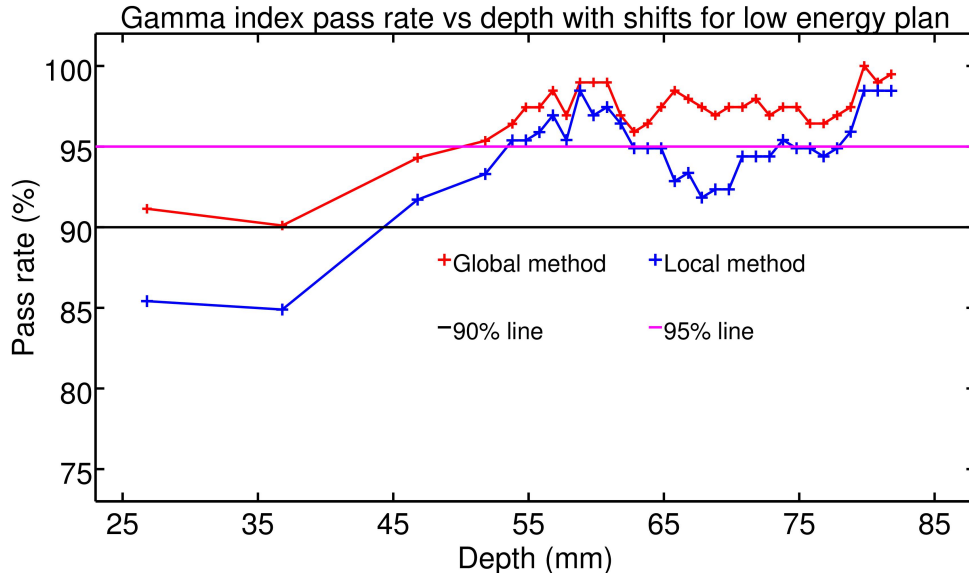


Figure 3.16: The gamma index pass rate vs depth for the low energy plan. Lines are drawn through each data point to facilitate visualization only. 90% and 95% lines are likewise drawn showing the common tolerance limits.

create a histogram, whose area was normalized to 100. The resulting differential histograms are shown in Figures 3.17 and 3.18, with cumulative histograms in Figures 3.19 and 3.20. So as to not bias the histograms to greater depths where the number of measurement points is greater, each set of $\gamma_s(\mathbf{R}_r)$ for a given depth and method was multiplied by the distance to the subsequent measurement point. All points with $\gamma_s(\mathbf{R}_r) \geq 1$ are gathered in the rightmost bin, since $\gamma_s(\mathbf{R}_r)$ cannot be taken to be equal to $\gamma(\mathbf{R}_r)$ in this region.

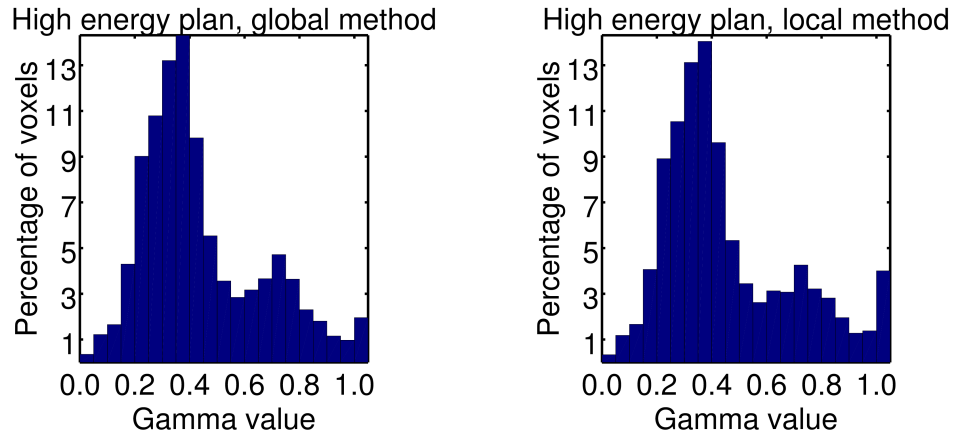


Figure 3.17: The differential distribution of $\gamma(\mathbf{R}_r)$ for all the depths for the high energy plan, using the global method on the left and local on the right.

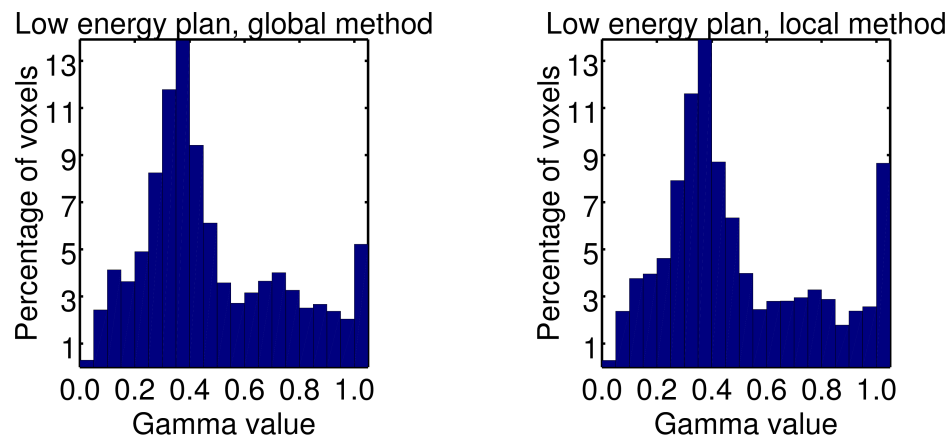


Figure 3.18: The differential distribution of $\gamma(\mathbf{R}_r)$ for all the depths for the low energy plan, using the global method on the left and local on the right.

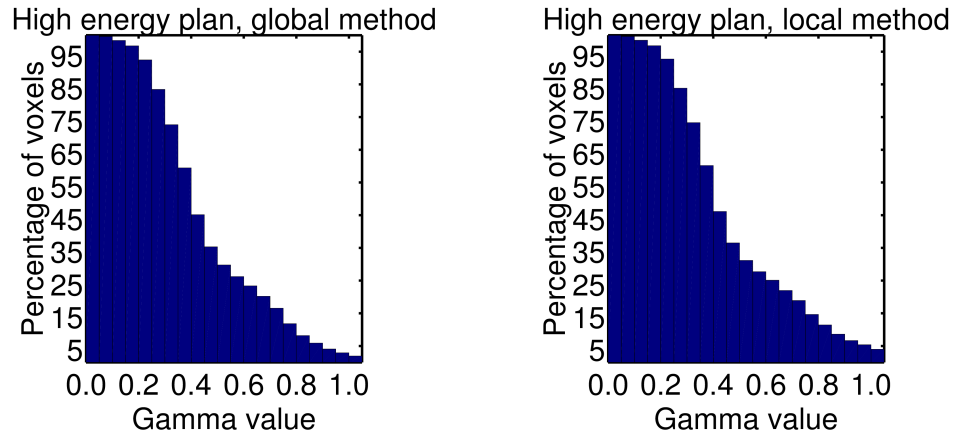


Figure 3.19: The cumulative distribution of $\gamma(\mathbf{R}_r)$ for all the depths for the high energy plan, using the global method on the left and local on the right.

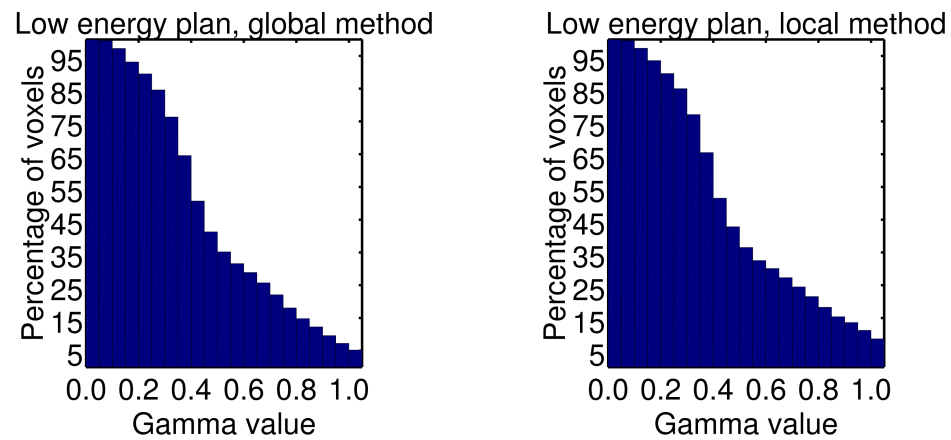


Figure 3.20: The cumulative distribution of $\gamma(\mathbf{R}_r)$ for all the depths for the low energy plan, using the global method on the left and local on the right.

Chapter 4

Discussion

4.1 Results

A glance at Figures 3.1, 3.2 and 3.3, as well as Table 3.1, indicates a reasonably smooth variation with energy in all cases for the optical parameters. The χ^2 values found in Table 3.1 does indicate, given the errors as plotted in the Figures, that variation with energy is not very smooth for the emittance and spot size in x. These high χ^2 -values are probably caused by the initial data points where the error bars are small, and thus relative to the size of the error bars the distance to the polynomial curve is large. Although the uncertainty associated with a data point might be small this does not guarantee that the data points will vary smoothly with energy. The latter is very much effected by beam tuning. Some low χ^2 -values were also reported in Table 3.1, indicating the error bars may be too large. Possibly a lower order polynomial would yield better χ^2 -values. The maximum measured-simulated differences are relatively small however, and Figure 3.4 and Table 3.2 indicates clinically acceptable accuracy in terms of spot size prediction.

Given that the lower energies means more degrader material in the beam line, the parameter values decreasing with increasing energy is reasonable and what would one expect. The very slight rise or flattening of the polynomial curves for the top energies may be a result of tuning. The spot size at isocenter may still be smaller, or tuning for these energies were less successful. It is worth noting that IBA has performed their own spot size measurement and fits, and these may conflict with those presented above due to differences in the measurement and fitting methods. A comparison of the results would suggest that the optical beam parameters as found in this work provides a level of accuracy roughly equal to that of Grevillot et al.

The basic method to compute the energy at nozzle exit from the range at nozzle entrance seemed to produce accurate results, with a maximum noted deviation of 0.18 mm in the projected range from the measured, as noted for distal d80 in Table 3.3. For the remaining ranges where the differences were evaluated, a glance at Figure 3.10 would suggest that the found values of the energy spread parameter using the method detailed in Section 2.4 are reasonable. For certain cases, the ranges differed by more than 0.5 mm, with a maximum of 0.86 mm. It may be noted that all of the deviations > 0.5 mm ended up on the proximal side of curves. A possible explanation may be found in the statistical fluctuations

in the simulated dose depth curves. The size of these fluctuations seems to be the greatest at high energies on the proximal side of the Bragg peak.

These fluctuations inhibit the range finding algorithm's ability to accurately find the range for a certain dose. This is especially prominent at the proximal d50 level where the proton kinetic energy is the greatest of all the six considered ranges, and hence dE/dx the flattest as indicated in Figure 1.4. During development of the general algorithm to find the energy spread, it was also found that the Geant4 physics models were in general unable to model both the plateau region and the proximal rise accurately simultaneously. An accurate modeling of the plateau region often meant underestimating the d50, d80 and d90, whereas an accurate modeling of the latter three often lead to an underestimation of the dose in the plateau region. If the measured-simulated range difference for certain dose levels is deemed excessive, fine tuning of the energy spread is possible for these cases.

The γ -index test was as indicated in the Section 3.3 complicated by a series of factors. By introducing corrective shifts based on the assumption of a set up error, acceptable pass rates could be achieved. A case for the validity of these corrective shifts can be made as follows.

First, the increasing translation necessary in the x-direction to provide reasonable pass rates suggested a rotation around the y -axis. This axis is the only axis that could reasonably accept a rotation, since the Digipant was resting on the treatment couch, whose flatness would prohibit rotation around the other axes. Second, the high and low energy treatment plan measurements were performed back to back without modifying the experimental set up. The fact that the same angle of rotation and constant shifts could be used to model the translation for both the high and low energy treatment plan suggests a set up error. It should further be noted that the beam model itself is not involved in positioning a 2D dose distribution in a given coordinate system. Therefore, if a simulated dose distribution by a simple translation can be made to match the measured dose distribution, it should constitute validation.

The resolution of the MatriXX is far from ideal. It provides little opportunity for a comparison of the penumbra; the latter is effectively measured by a single row or column on the MatriXX as is evident from Figure 4.1. Film for instance could provide a much improved resolution relative to the MatriXX, and would be useful for further measurements seeking to validate the beam model. With increased resolution follows an increase in computation time needed to perform the gamma index test, even using the limited search method. For a film resolution of 0.1 mm, and for the same number of depths per treatment plan, the gamma index test would take hours. Speed gains may be sought in using a compiled programming language such as C++ as opposed to a scripted language like Octave.

In depth, along the z -axis, the beam model is very much involved in the sense of setting the energy at the nozzle exit and thus controlling the proton range. Since the energy at nozzle exit seems to be a very smooth function of the range at the nozzle entrance as indicated by Figure 3.5 and the projected range (distal d80) in Table 3.3 suggests the beam model should be able to accurately predict the range, and if anything, slightly overestimate it, the issue may be as hinted in Section 3.3 related to the translation from geometrical depth to IBA WET depth. Evidence in favor of this conclusion would be that the simulated range for both the high and low energy is a constant 2 mm shorter than the corresponding measured ranges. Measurements performed by commissioning physicists indicated that the IBA WET was overestimated by around 1.1 mm, not enough to explain the full 2 mm, but indicative of an systematic error that would push the measured curve in the direction observed in Figure 3.13 relative to the simulated curve. The nature of this shift warrants further investigation in future work.

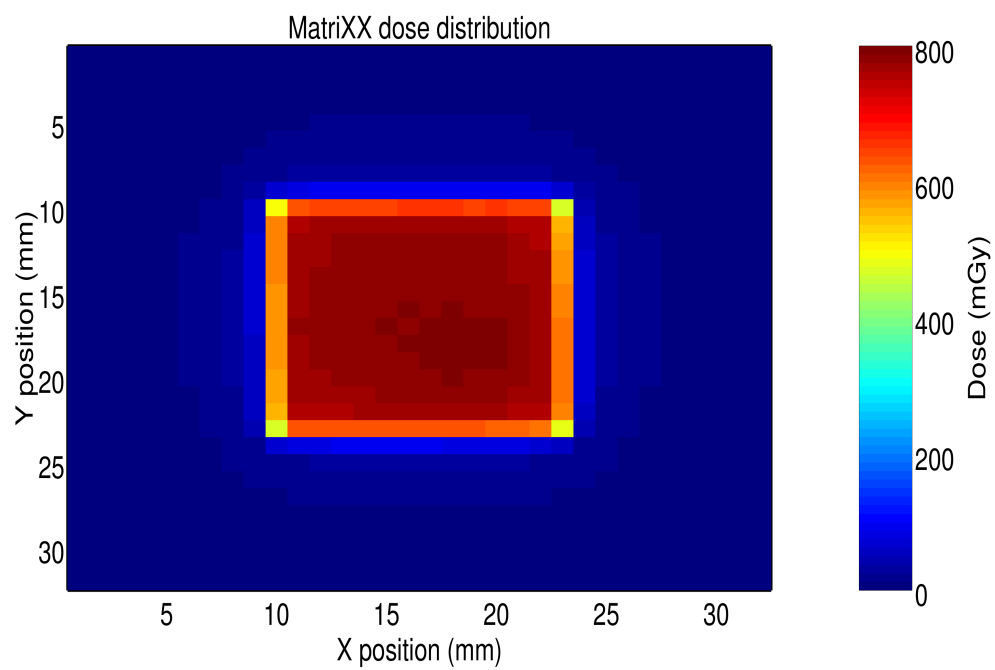


Figure 4.1: An example of a dose distribution as measured by the MatriXX.

4.2 Method

A potential weakness of the beam model as described in this work is its dependence on the beam parameters varying smoothly with energy. If this is not the case, the errors introduced by the polynomial fit may become unacceptable for clinical applications. Whether the parameters does vary smoothly or not with energy is very much dependent on beam tuning. At Skandionkliniken tuning was performed for each energy individually by IBA. During tuning, keeping the spot size small at isocenter takes priority over keeping beam waist variation with energy smooth; the latter is important for the emittance parameter. If the smoothness with energy cannot be achieved for a system, a different approach will be necessary.

Five of the eight parameters are modeled as single Gaussians. As noted the Introduction, more advanced functions such as triple Gaussians or a double Gaussian and a Cauchy-Lorentz function have been suggested to provide more accurate modeling of the spot size. The Gaussian approximation follows naturally as a consequence of the central limit theorem when considering the numerous, small scale electromagnetic interactions as a proton penetrates an absorber. However, nuclear interactions do not follow this pattern with their large angular deflections and possible generation of neutrons and ions. By using a single Gaussian to approximate the spot size at the nozzle exit, in effect the halo as generated in the nozzle is ignored or underestimated. The path traveled by the protons through the as of this writing unique nozzle at Skandionkliniken consists mostly of vacuum; the ion chambers are exceptions, but IC1 is held at 200 mbar. The WET of the nozzle and the ~ 50 cm air gap between nozzle exit and isocenter is around 2 mm, although there is a slight dependency on energy. This is illustrated in Figure 4.2.

As already argued in 2.1, the nozzle exit as a starting point for simulation is particular attractive for pencil beam scanning in general for this very reason. The reduced amount of material in the beam path reduces the number of interactions inside the nozzle. From this of course follows a reduced halo. However, in [68] it is suggested that a full geometrical reconstruction of the nozzle might be necessary however for studies of out of field dosimetry, with simulation starting at the nozzle entrance. For paediatric patients and other cases where long term secondary effects are especially important, this might be of particular interest.

Since it was not possible to procure Lynx measurements closer to the nozzle exit than isocenter -19 cm, IC2/3 data had to be resorted to. The IC2/3 reading of the spot size cannot match the accuracy provided by the 2D Gaussian fits to the Lynx data. Ideally, a number of Lynx measurements in the interval between the nozzle exit and isocenter -19 cm would have been preferable and might have increased the accuracy of the optical parameters.

An issue with MC in general is, as has already been noted, the high demands on computing power to complete tasks in a reasonable time frame. Some steps in the method outline in Chapter 2 would require a single computer weeks to finish. In principle, the air correction method detailed in Section 2.3 could be replaced by an analytical and thus computationally cheaper method using a scattering power model such as that given by [94]. Let z_{iso+20} be the air depth at isocenter +20 cm, and let the origin $z = 0$ be at the nozzle exit. If the $\frac{a}{b}$ -value resulting from the hyperbola fit to the data can be taken to provide the numerical value of the angular spread at some point $0 < z < z_{iso+20}$, then the angular spread σ_θ at the nozzle exit can be calculated as

$$\sigma_\theta = \frac{a}{b} - \int_0^z T(z') dz'$$

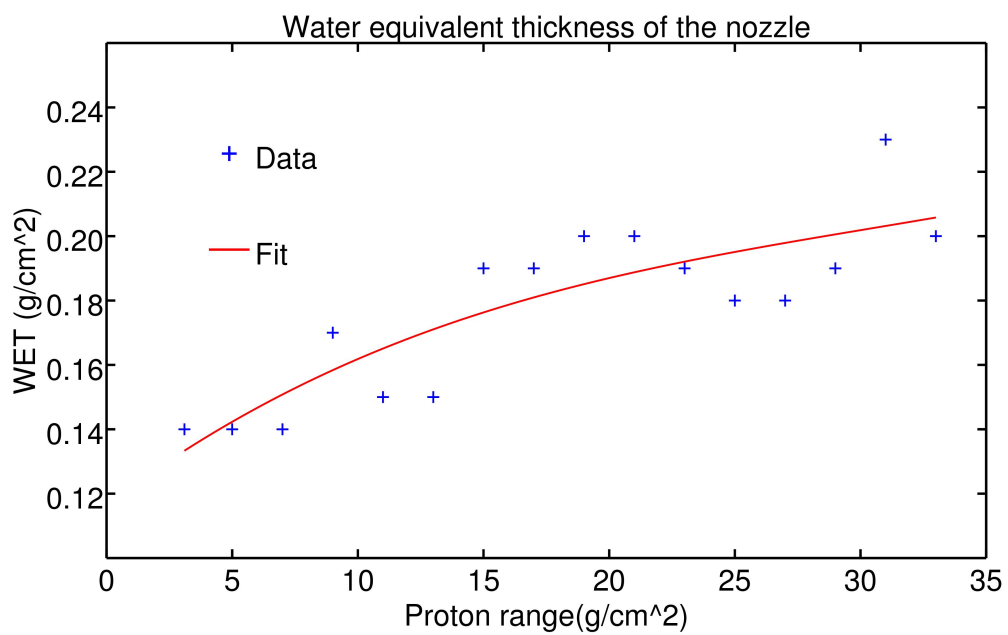


Figure 4.2: The nozzle and air gap WET as a function of range. Data and polynomial fit as supplied by IBA.

where $T(z')$ is the scattering power as a function of depth z' .

The method to find the beam model will only have to be run once, however. A more serious issue is the time needed to run the actual simulations. To obtain an uncertainty of around 1-2% in the central region of the dose distribution for the treatment plans run for the gamma index test such as that shown in Figure 4.1, it was necessary to simulate about 50 million protons. For the high energy plan, some 30 primary protons were simulated per second per CPU core, rising to 50 primary protons per CPU core for the low energy plan. To be able to finish the high energy simulation in 24 hours, 20 cores had to be used. Even though Geant4 as of version 10.0 supports multi-threading this has yet to be extended to GATE, wherefore each of the core ran its own instance of the simulation, simulating 2.5 million protons, and once all cores had finished the results were combined. For routine clinical use as a part of the patient specific QA procedures, a dedicated computer cluster will be necessary to provide sufficient computing power. Some gain in speed may be achieved once GATE attains multi-threading support, as will the ever increasing performance of available computer hardware. GPU based simulation is also an option.

Chapter 5

Conclusion

It has been shown that the method used can be generalized to provide optical parameters handling beams that are convergent after the nozzle exit by application of simple Fermi-Eyges theory. This generalization is still achievable using BDL measurements only, complemented by log file data that can be retrieved without having to perform additional measurements. The algorithm devised to find the energy spread was able to keep the proximal and distal d50, d80 and d90 differences between simulated and measured IDD curves below 0.5 mm in most cases, with the more difficult cases concentrating to the proximal side at higher energies. Spot size prediction was within 0.2 mm for the vast majority of cases, with few outliers. The projected range in terms of the distal d80 was within 0.2 mm for all cases. Problems with the gamma index tests necessitated certain data manipulation to provide reasonable results; a case can be made for the validity of these manipulations. Further work is necessary before routine use in QA. More detailed dose distribution measurements, preferably with equipment of higher resolution than the MatriXX would be necessary to verify the data manipulations and test beam model performance in high dose gradient regions. Introducing metallic or other objects into the water phantom would allow testing of the beam model's capabilities for dealing with inhomogeneities. Adding capabilities for simulating multiple-field treatment plans is also necessary. Securing additional computing power on a permanent basis would also be mandatory to be able to perform simulations on a daily basis with sufficient accuracy. If that is not an option, exploring GPU-powered simulation would be a possibility.

Appendix

In this appendix, plots the weighted least square hyperbola fits to the air corrected data as described in Section 2.3 for all energies are shown.

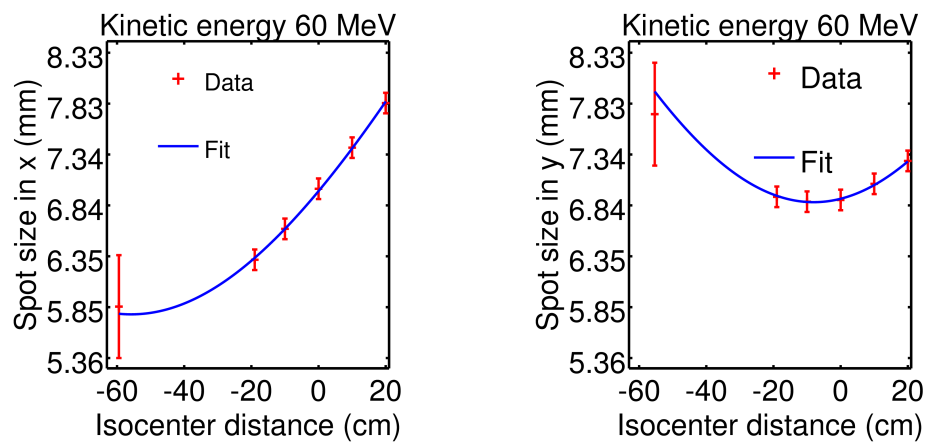


Figure 5.1:

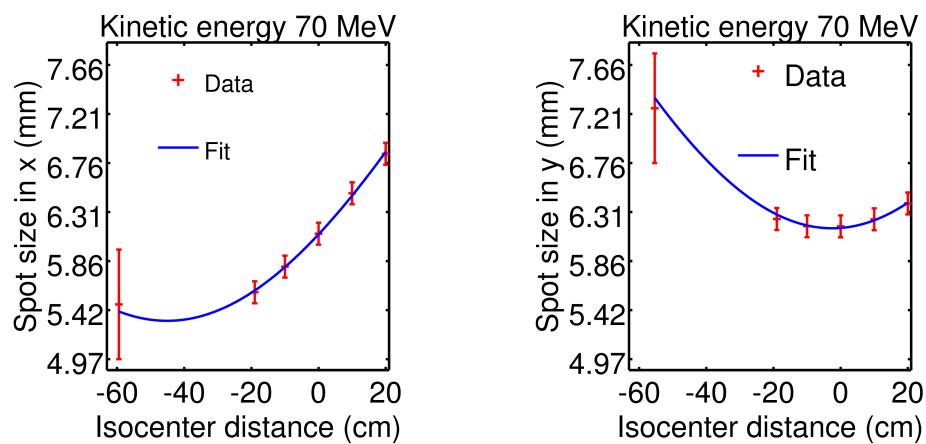


Figure 5.2:

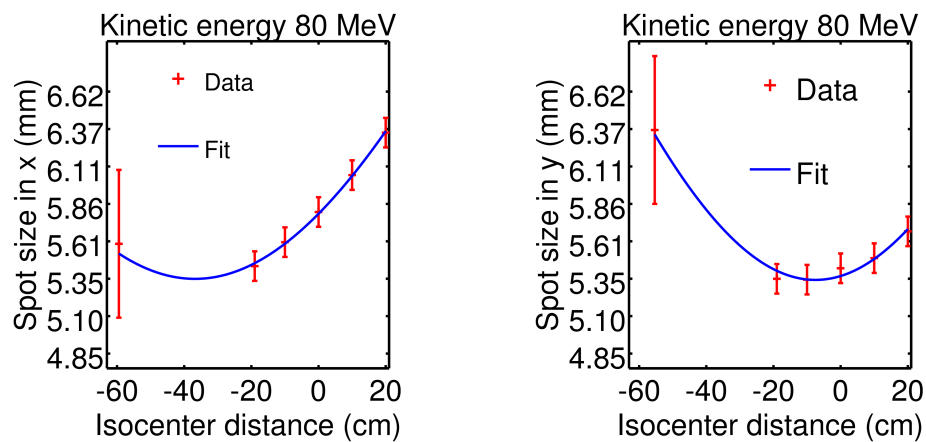


Figure 5.3:

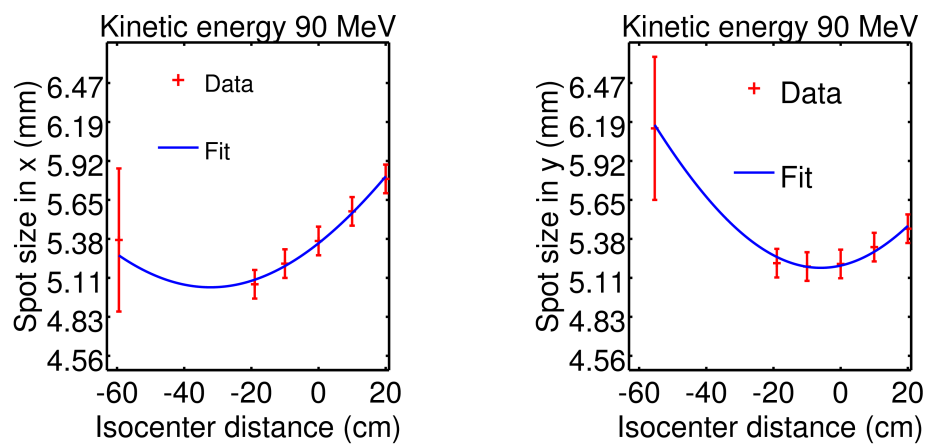


Figure 5.4:

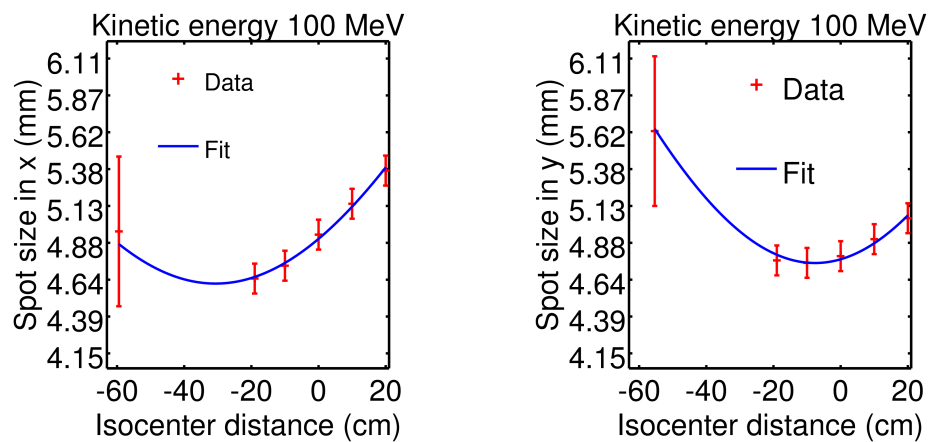


Figure 5.5:

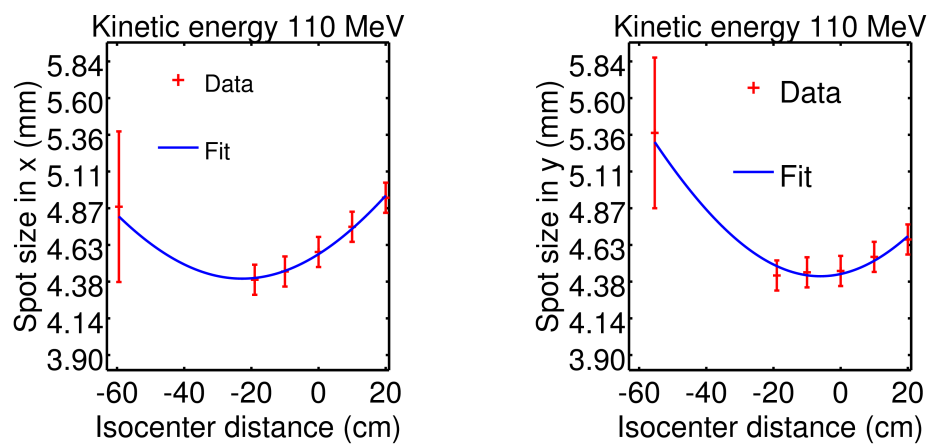


Figure 5.6:

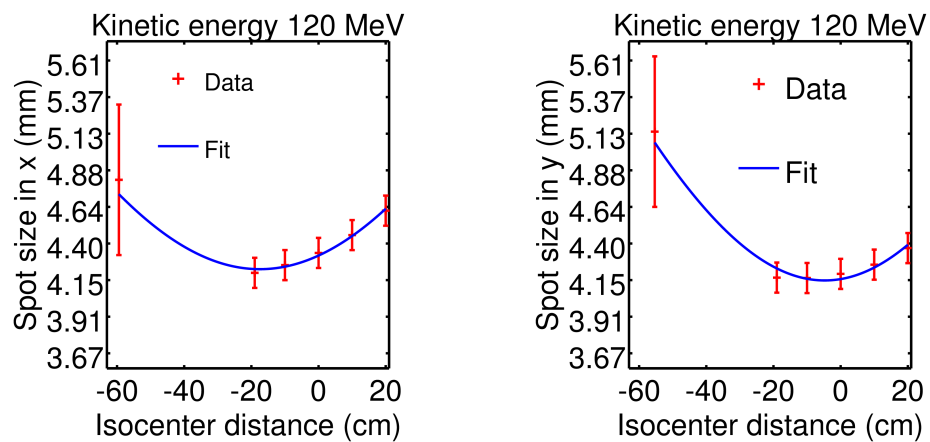


Figure 5.7:

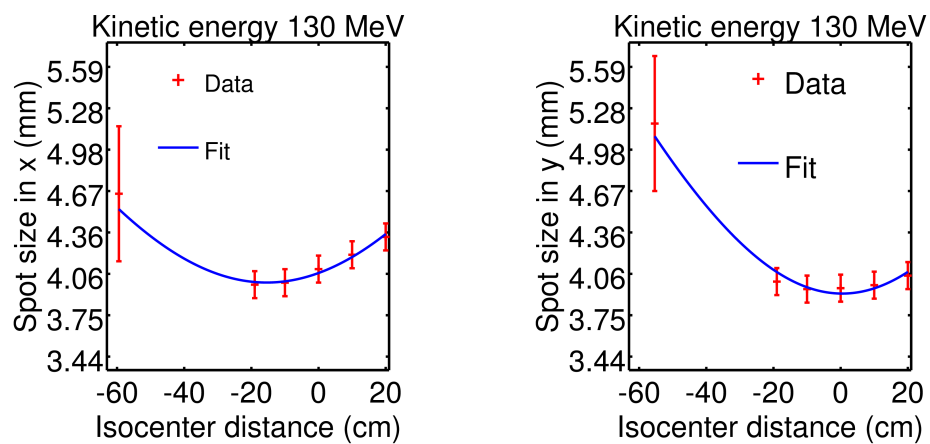


Figure 5.8:

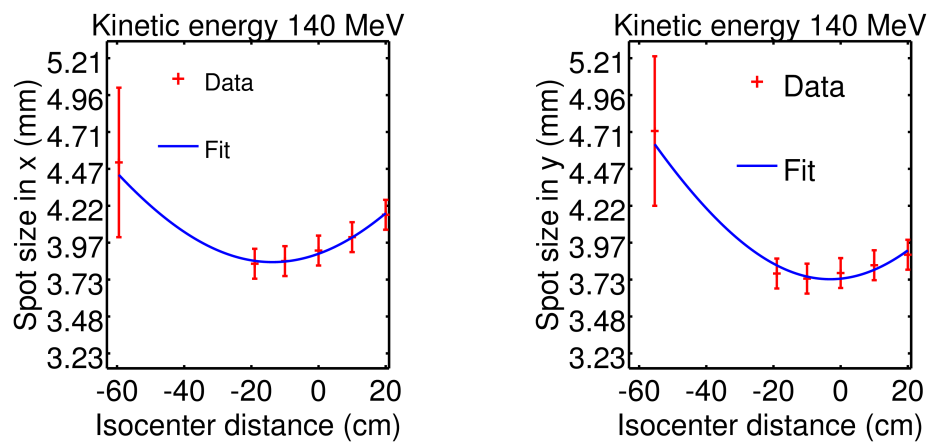


Figure 5.9:

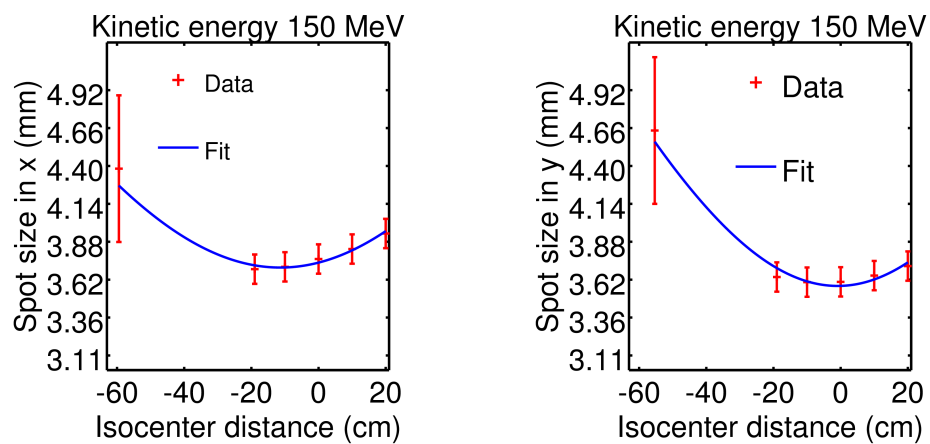


Figure 5.10:

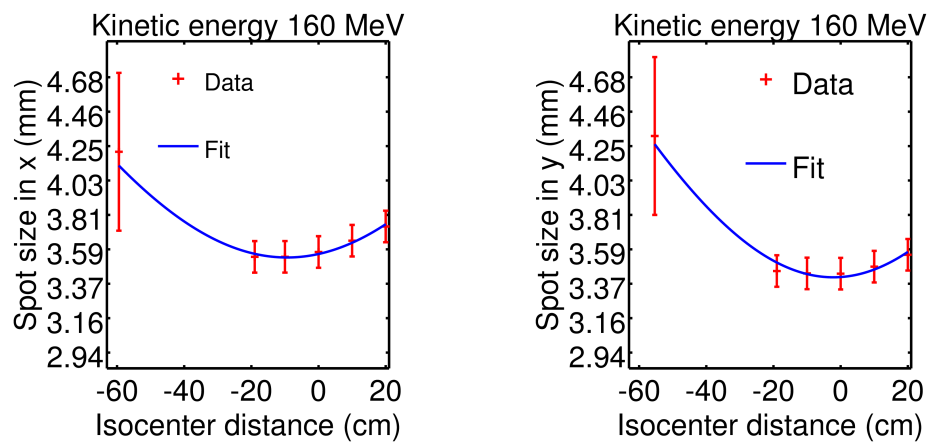


Figure 5.11:

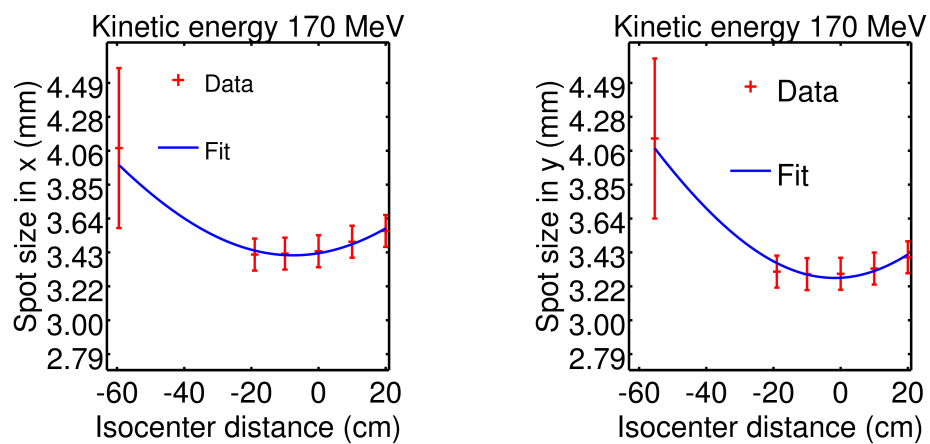


Figure 5.12:

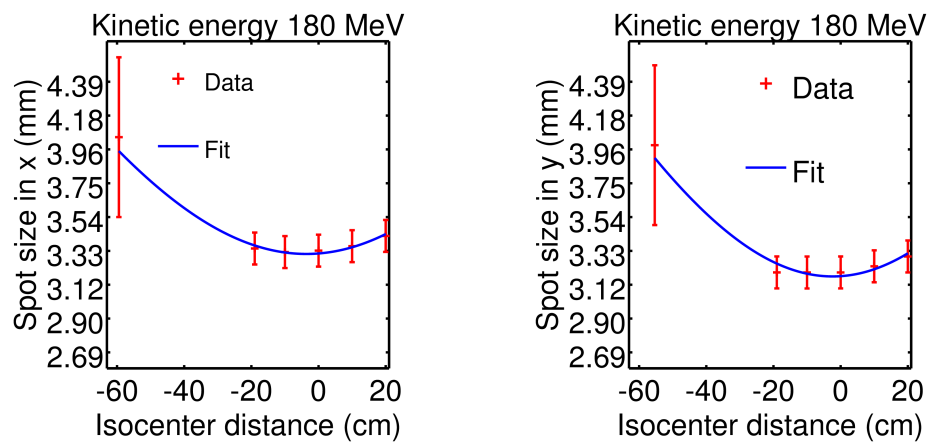


Figure 5.13:

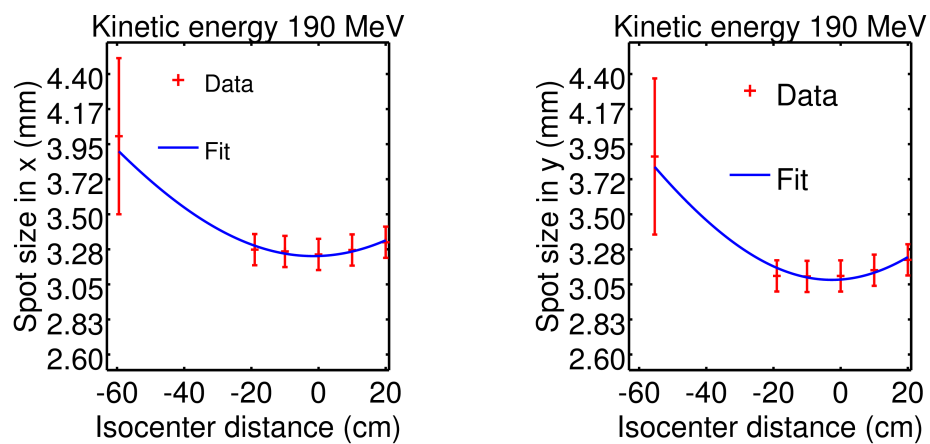


Figure 5.14:

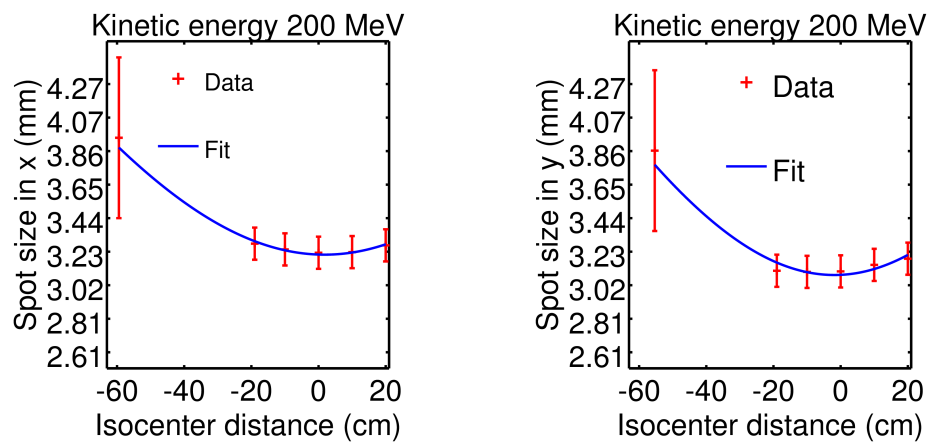


Figure 5.15:

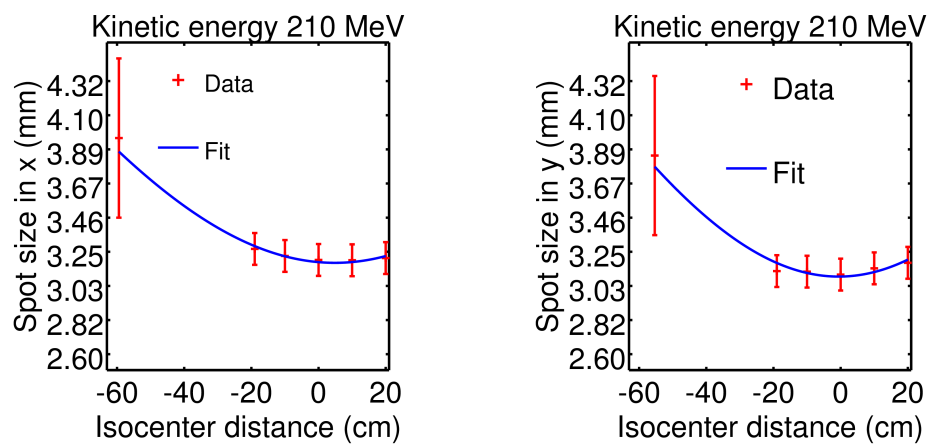


Figure 5.16:

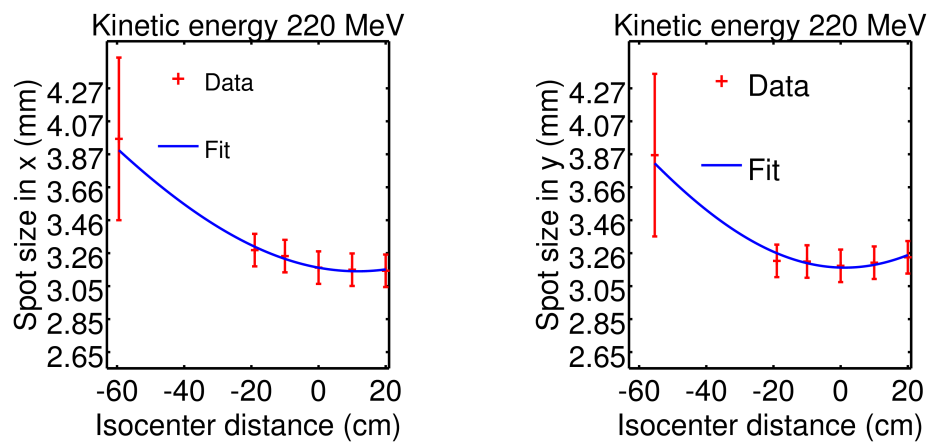


Figure 5.17:

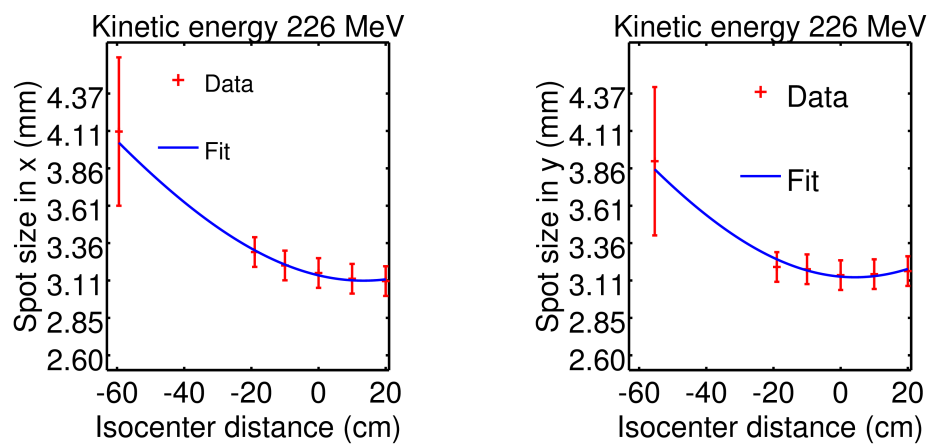


Figure 5.18:

List of abbreviations

BDL-Beam Data Library
CPU-Central Processing Unit
CSDA-Continuous Slowing Down Approximation
CT-Computed Tomography
GPU-Graphics Processing Unit
HP-High Precision
HU-Hounsfield Unit
IBA-Ion Beam Applications
IDD-Integral Depth Dose
IMPT-Intensity Modulated Proton Therapy
IMRT-Intensity Modulated Radiotherapy
MC-Monte Carlo
MCS-Multiple Coulomb Scattering
MLC-Multileaf Collimator
MU-Monitor Unit
PBS-Pencil Beam Scanning
PSI-Paul Scherrer Institute
PTV-Planning Target Volume
QA-Quality Assurance
SNIC-Swedish National Infrastructure for Computing
SOBP-Spread Out Bragg Peak
TPS-Treatment Planning System
UPPMAX-Uppsala Multidisciplinary Center for Advanced Computational Science
VMAT-Volumetric Arc Therapy
WET-Water Equivalent Thickness

Bibliography

- [1] R. R. Wilson. Radiological use of fast protons. *Radiology*, 47(5):487–491, 1946. [1](#)
- [2] H. Paganetti. Proton Therapy: History and Rationale. In H. Paganetti, editor, *Proton Therapy Physics*, pages 1–18. CRC Press, 2011. [1](#)
- [3] Nuclear Physics European Collaboration Committee. Nuclear Physics for Medicine. Technical report, 2014. [1](#)
- [4] T. F. DeLaney. Proton therapy in the clinic. *Frontiers of Radiation Therapy and Oncology*, 43:465–485, 2011. [1](#)
- [5] H. Paganetti. Range uncertainties in proton therapy and the role of Monte Carlo simulations. *Phys. Med. Biol.*, 57:R99–R117, 2012. [1](#)
- [6] A. V. Chvetsov and S. L. Paige. The influence of CT image noise on proton range calculation in radiotherapy planning. *Phys. Med. Biol.*, 55:N141–N149, 2010. [1](#)
- [7] A. Zietman. Proton beam and prostate cancer: An evolving debate. *Reports of Practical Oncology and Radiotherapy*, 18:338–342, 2013. [1](#)
- [8] J. Flanz and T. Bortfeld. Evolution of Technology to Optimize the Delivery of Proton Therapy: The Third Generation. *Seminars in Radiation Oncology*, 23(2):142–148, 2013. [1](#)
- [9] M. Gotein and M. Jermann. The relative costs of proton and X-ray radiation therapy. *Clin Oncol*, 15:S37–S50, 2003. [1](#)
- [10] U. Linz and J. Alonso. What will it take for laser driven proton accelerators to be applied to tumor therapy? *Phys. Rev. ST Accel. Beams*, 10(094801), 2007. [1](#)
- [11] D. Trbojevic, B. Parker, E. Keil, and A. M. Sessler. Carbon/proton therapy: A novel gantry design. *Phys. Rev. ST Accel. Beams*, 10(053503), 2007. [1](#)
- [12] A. R. Smith. Vision 20/20 : Proton therapy. *Med. Phys.*, 36:556–568, 2009. [1](#)
- [13] B. Clasie, N. Depauw, M. Fransen, C. Gomà, H. R. Panahandeh, J. Seco, J. B. Flanz, and H. M. Kooy. Golden beam data for proton pencil-beam scanning. *Phys. Med. Biol.*, 57:1147–1158, 2012. [1](#)

- [14] J. Flanz. Particle Beam Scanning. In H. Paganetti, editor, *Proton Therapy Physics*. CRC Press, 2011. [1](#)
- [15] H. Paganetti, H. Jiang, K. Parodi, R. Slopsema, and M. Engelsman. Clinical implementation of full Monte Carlo dose calculation in proton beam therapy. *Phys. Med. Biol.*, 53:4825–4853, 2008. [1](#), [2.1](#)
- [16] J. M. Schippers and A. J. Lomax. Emerging technologies in proton therapy. *Acta Oncologica*, 50:838–850, 2011. [1](#)
- [17] E. Pedroni, T. Böhringer, A. Coray, M. Grossmann, S. Lin, and A. Lomax. Experimental characterization and physical modelling of the dose distribution of scanned proton pencil beams. *Phys. Med. Biol.*, 50:541–561, 2005. [1](#)
- [18] G. O. Sawakuchi, R. X. Zhu, F. Poenisch, K. Suzuki, G. Ciangaru, U. Titt, A. Anand, R. Mohan, M. T. Gillin, and N. Sahoo. Experimental characterization of the low-dose envelope of spot scanning proton beams. *Phys. Med. Biol.*, 55:3467–3478, 2010. [1](#)
- [19] L. Lin, C. G. Ainsley, T. Mertens, O. De Wilde, P. T. Talla, and J. E. McDonough. A novel technique for measuring the low-dose envelope of pencil-beam scanning spot profiles. *Phys. Med. Biol.*, 58:N171–N180, 2013. [1](#)
- [20] L. Lin, C. G. Ainsley, and J. E. McDonough. Experimental characterization of two-dimensional pencil beam scanning proton spot profiles. *Phys. Med. Biol.*, 58:6193–6204, 2013. [1](#)
- [21] L. Lin, C. G. Ainsley, T. D. Solberg, and J. E. McDonough. Experimental characterization of two-dimensional spot profiles for two proton pencil beam scanning nozzles. *Phys. Med. Biol.*, 69:493–504, 2014. [1](#)
- [22] Y. Li, R. X. Zhu, N. Sahoo, A. Anand, and X. Zhang. Beyond Gaussians: a study of single-spot modeling for scanning proton dose calculation. *Phys. Med. Biol.*, 57:983–997, 2012. [1](#)
- [23] V. E. Bellinzona, M. Ciocca, A. Embriaco, A. Fontana, A. Mairani, M. Mori, and K. Parodi. On the parametrization of lateral dose profiles in proton radiation therapy. *Physica Medica*, 31(5):484–492, 2015. [1](#)
- [24] C. E. Agnew, R. B. King, A. R. Hounsell, and C. K. McGarry. Implementation of phantomless IMRT delivery verification using Varian DynaLog files and R/V output. *Phys. Med. Biol.*, 57:6761–6777, 2012. [1](#)
- [25] H. Li, N. Sahoo, F. Poenisch, K. Suzuki, X. Li, X. Zhang, A. K. Lee, M. T. Gillin, and X. R. Zhu. Use of treatment log files in spot scanning proton therapy as part of patient-specific quality assurance. *Med. Phys.*, 40(021703), 2013. [1](#)
- [26] J. Qian, L. Lee, W. Liu, K. Chu, E. Mok, G. Luxton, Q. Le, and L. Xing. Dose reconstruction for volumetric modulated arc therapy (VMAT) using cone-beam CT and dynamic log files. *Phys. Med. Biol.*, 55:3597–3610, 2010. [1](#)
- [27] B. Sun, D. Rangaraj, S. Boddu, M. Goddu, Y. Deshan, G. Palaniswaamy, S. Yaddanapudi, O. Wooten, and S. Mutic. Evaluation of the efficiency and effectiveness of independent dose calculation followed by machine log file analysis against conventional measurement based IMRT QA. *Journal of Applied Clinical Medical Physics*, 13(5):140–154, 2012. [1](#)

- [28] K. Strijckmans. The isochronous cyclotron: principles and recent developments. *Computerized Medical Imaging and Graphics*, 25:69–78, 2001. 1.1
- [29] D. L. Friesel and T. A. Antaya. Medical Cyclotrons. In A. W. Chou and W. Chou, editors, *Reviews of Accelerator Science and Technology, Volume 2: Medical Applications of Accelerators*, volume 2, pages 133–156. World Scientific Publishing Co., 2009. 1.1
- [30] M. Schippers. Proton Accelerators. In H. Paganetti, editor, *Proton Therapy Physics*, pages 62–102. CRC Press, 2011. 1.1
- [31] V. Anferov. Energy degrader optimization for medical beam lines. *Nuclear Instruments and Methods in Physics Research A*, 496:222–227, 2003. 1.1
- [32] H. Wiedemann. *Particle Accelerator Physics I: Basic Principles and Linear Beam Dynamics*. Springer, 2003. 1.1
- [33] U. Titt, B. Bednarz, and H. Paganetti. Comparison of MCNPX and Geant4 proton energy deposition predictions for clinical use. *Phys. Med. Biol.*, 57:6381–6393, 2012. 1.2.1
- [34] H. W. C. Tseung, J. Ma, and C. Beltran. A fast GPU-based Monte Carlo simulation of proton transport with detailed modeling of nonelastic interactions. *Med. Phys.*, 42(1474), 2015. 1.2.1
- [35] D. Giantsoudi, J. Schümann, X. Jia, S. Dowdell, H. Jiang, and H. Paganetti. Validation of a GPU-based Monte Carlo code (gPMC) for proton radiation therapy: clinical cases study. *Phys. Med. Biol.*, 60:2257–2269, 2015. 1.2.1
- [36] X. Jia, J. Schümann, H. Paganetti, and S. B. Jiang. GPU-based fast Monte Carlo dose calculation for proton therapy. *Phys. Med. Biol.*, 57:7783–7797, 2012. 1.2.1
- [37] J. Bert, H. Perez-Ponce, Z. El Bitar, S. Jan, Y. Boursier, D. Vintache, A. Bonissent, C. Morel, D. Brasse, and D. Visvikis. Geant4-based Monte Carlo simulations on GPU for medical applications. *Phys. Med. Biol.*, 58:5593–5611, 2013. 1.2.1
- [38] M. Fippel. Basics of Monte Carlo Simulations. In J. Seco and F. Verhaegen, editors, *Monte Carlo Techniques in Radiation Therapy*, pages 17–28. CRC Press, 2013. 1.2.1
- [39] W. Matthes. Monte-Carlo simulation of charged-particle histories (dominant small-angle scattering). *Ann. Nucl. Energy*, 8:455–459, 1981. 1.2.1
- [40] M. F. Berger. Monte Carlo Calculation of the penetration and diffusion of fast charged particles. In B. Adler, S. Fernbach, and M. Rotenberg, editors, *Methods in Computational Physics*, volume 1. Academic Press, 1963. 1.2.1
- [41] E. W. Larsen. A theoretical derivation of the condensed history algorithm. *Ann. Nucl. Energy*, 19(10-12):701–714, 1992. 1.2.1
- [42] H. A. Bethe. Moliere’s Theory of Multiple Scattering. *Phys. Rev.*, 89(6):1256–1266, 1953. 1.2.1
- [43] H. W. Lewis. Multiple Scattering in an Infinite Medium. *Phys. Rev.*, 78(5):526–529, 1950. 1.2.1
- [44] S. Goudsmit and J. L. Saunderson. Multiple Scattering of Electrons. *Phys. Rev.*, 57(1):24–29, 1940. 1.2.1

- [45] L. Eyges. Multiple Scattering with Energy Loss. *Phys. Rev.*, 74:1534–1535, 1948. [1.2.1](#), [2.3](#)
- [46] H. Paganetti. Protons: Clinical Considerations and Applications. In J. Seco and F. Verhaegen, editors, *Monte Carlo Techniques in Radiation Therapy*, pages 201–221. CRC Press, 2013. [1.2.1](#), [2.1](#)
- [47] L. E. Porter. Bethe-Bloch stopping power parameters for light projectiles at energies near the stopping power maximum. *Nuclear Instruments and Methods in Physics Research B12*, pages 50–55, 1985. [1.2.1](#)
- [48] P. Andreo. On the clinical spatial resolution achievable with protons and heavier charged particle radiotherapy beams. *Phys. Med. Biol.*, 54:N205–N215, 2009. [1.2.1](#)
- [49] G. Battistoni, F. Cerutti, A. Fasso, A. Ferrari, S. Muraru, J. Ranft, S. Roesler, and P. R. Sala. The FLUKA code: description and benchmarking. *AIP Conference Preceeding*, 896:31–49, 2007. [1.2.1](#)
- [50] S. Agostinelli, J. Allison, K. Amako, J. Apostolakis, H. Araujo, P. Acre, M. Asai, D. Axen, S. Banerjee, G. Barrand, F. Behner, Bellagamba. L., J. Boudreau, L. Broglia, A. Brunengo, H. Burkhardt, S. Chauvie, J. Chuma, R. Chytracsek, G. Cooperman, G. Cosmo, P. Degtyarenko, A. Dell’Acqua, G. Depaola, D. Dietrich, R. Enami, A. Feliciello, C. Ferguson, H. Fesefeldt, G. Folger, F. Foppiano, A. Forti, S. Garelli, S. Giani, R. Giannitrapani, D. Gibin, J. J. Gomez, V. Grichine, A. Grossheim, S. Guatelli, P. Gumplinger, R. Hamatsu, K. Hashimoto, H. Hasui, A. Heikkinen, A. Howard, V. Ivanochenko, A. Johnson, F. W. Jones, J. Kallenbach, N. Kanaya, M. Kawabata, Y. Kawabata, M. Kawaguti, S. Kelner, P. Kent, A. Kimura, T. Kodama, R. Kokoulin, M. Kossov, H. Kurashige, E. Lamanna, T. Lampen, V. Lara, V. Lefebure, F. Lei, M. Liendl, W. Lockman, F. Longo, S. Magni, M. Maire, E. Medernach, K. Minamimoto, P. Mora de Freitas, Y. Morita, K. Murakami, M. Nagamatu, R. Nartallo, P. Nieminen, T. Nishimura, K. Ohtsubo, M. Okamura, S. O’Neale, Y. Oohata, K. Paech, J. Perl, A. Pfeiffer, M. G. Pia, F. Ranjard, A. Rybin, S. Sadilov, E. Di Salvo, G. Santin, T. Sasaki, N. Savvas, Y. Sawada, S. Scherer, S. Sei, V. Sirotenko, D. Smith, N. Starkov, H. Stoecker, J. Sulkimo, M. Takahata, S. Tanaka, E. Tcherniaev, E. Safai Tehrani, M. Tropeano, P. Truscott, H. Uno, L. Urban, P. Urban, M. Verderi, A. Walkden, W. Wander, H. Weber, J. P. Wellisch, T. Wenaus, D. C. Williams, D. Wright, T. Yamada, H. Yoshida, and D. Zschesche. GEANT4-a simulation toolkit . *Nuclear Instruments and Methods in Physics Research A*, 506:250–303, 2003. [1.2.1](#)
- [51] J. Allison, K. Amako, J. Apostolakis, H. Araujo, P. Arce Dubois, M. Asai, G. Barrand, R. Capra, S. Chauvie, R. Chytracsek, G. A. P. Cirrone, G. Cooperman, G. Cosmo, G. Cuttone, G. G. Daquino, M. Donszelmann, M. Dressel, G. Folger, F. Foppiano, J. Generowicz, V. Grichine, S. Guatelli, P. Gumplinger, A. Heikkinen, I. Hrivnacova, A. Howard, S. Incerti, V. Ivanochenko, T. Johnson, F. Jones, T. Koi, R. Kokoulin, M. Kossov, H. Kurashige, V. Lara, S. Larsson, F. Lei, O. Link, F. Longo, M. Maire, A. Mantero, B. Mascialino, I. McLaren, P. Mendez Lorenzo, K. Minamimoto, K. Murakami, P. Nieminen, L. Pandola, S. Parlati, L. Peralta, J. Perl, A. Pfeiffer, M. G. Pia, A. Ribon, P. Rodrigues, G. Russo, S. Sadilov, G. Santin, T. Sasaki, D. Smith, N. Starkov, S. Tanaka, E. Tcherniaev, B. Tome, A. Trindade, P. Truscott, L. Urban, M. Verderi, A. Walkden, J. P. Wellisch, D. C. Williams, D. Wright, and H. Yoshida. Geant4 Developments and Applications. *IEEE Transactions on Nuclear Science*, 53(1):270–278, 2006. [1.2.1](#)
- [52] *MCNPX 2.6.0 Manual*. [1.2.1](#)

- [53] J. Perl, J. Shin, J. Schümann, and H. Paganetti. TOPAS: An innovative proton Monte Carlo platform for research and clinical applications. *Med. Phys.*, 39:6818–6837, 2012. [1.2.1](#)
- [54] P. Arce, J. I. Lagares, L. Harkness, L. Desorgher, G. De Lorenzo, Y. Abreu, and Z. Wang. GAMOS: an easy and flexible way to use GEANT4. *IEEE Nuclear Science Symposium Conference Record*, pages 2230–2236, 2011. [1.2.1](#)
- [55] S. Jan, G. Santin, D. Strul, S. Staelens, K. Assie, D. Autret, S. Avner, R. Barbier, M. Bardiès, P. M. Bloomfield, D. Brasse, V. Breton, P. Bruyndonckx, I. Buvat, A. F. Chatzioannou, Y. Choi, Y. H. Chung, C. Comtat, D. Donnarieix, L. Ferrer, S. J. Glick, C. J. Groiselle, D. Guez, P-F. Honore, S. Kerhoas-Cavata, A. S. Kirov, V. Kohli, M. Koole, M. Krieguer, D. J. Van der Laan, F. Lamare, G. Largeron, C. Lartizien, D. Lazaro, M. C. Maas, L. Maigne, F. Mayet, F. Melot, C. Merheb, E. Pennacchio, J. Perez, U. Pietrzyk, F. R. Rannou, M. Rey, D. R. Schaart, C. R. Schmidlein, L. Simon, T. Y. Song, J. M. Vieira, D. Visvikis, R. Van de Walle, E. Wieers, and C. Morel. GATE: a simulation toolkit for PET and SPECT. *Phys. Med. Biol.*, 49:4543–4561, 2004. [1.2.1](#)
- [56] S. Jan, D. Denoit, E. Becheva, T. Carlier, F. Cassol, P. Descourt, T. Frisson, L. Grevillot, Guigues L., L. Maigne, C. Morel, Y. Perrot, N. Rehfeld, D. Sarrut, D. R. Schaart, S. Stute, U. Pietrzyk, D. Visvikis, N. Zahra, and I. Buvat. GATE V6: a major enhancement of the GATE simulation platform enabling modelling of CT and radiotherapy. *Phys. Med. Biol.*, 56:881–901, 2011. [1.2.1](#)
- [57] D. Sarrut, M. Bardiès, N. Boussion, N. Freud, S. Jan, J. Letang, G. Loudos, L. Maigne, S. Marcatali, T. Mauxion, P. Papadimitroulas, Y. Perrot, U. Pietrzyk, C. Robert, D. R. Schaart, D. Visvikis, and I. Buvat. A review of the use and potential of the GATE Monte Carlo simulation code for radiation therapy and dosimetry applications. *Med. Phys.*, 41(064301), 2014. [1.2.1](#)
- [58] L. Urban. Multiple Scattering model in GEANT4. CERN-OPEN-2002-070. [1.2.2](#)
- [59] *Geant 4. 10. 1: Physics Reference Manual*, December 2014. [1.2.2.1](#)
- [60] J. M. Fernandez-Varea, R. Mayol, J. Baro, and F. Salvat. On the theory and simulation of multiple elastic scattering of electrons. *Nuclear Instruments and Methods in Physics Research B*, 73:447–473, 1993. [1.2.2.1](#)
- [61] I. Kawrakow and A. F. Bielajew. On the condensed history technique for electron transport. *Nuclear Instruments and Methods in Physics Research Section B*, 142:253–280, 1998. [1.2.2.1](#)
- [62] J. Schümann, H. Paganetti, J. Shin, B. Faddageon, and J. Perl. Efficient voxel navigation for proton therapy dose calculation in TOPAS and Geant4. *Phys. Med. Biol.*, 57:3281–3293, 2012. [1.2.2.2](#)
- [63] G. Meier, R. Besson, A. Nanz, S. Safai, and A. J. Lomax. Independent dose calculations for commissioning, quality assurance and dose reconstruction of PBS proton therapy. *Phys. Med. Biol.*, 60:2819–2836, 2015. [1.3](#)
- [64] A. Stankovskiy, S. Kerhoas-Cavata, R. Ferrand, C. Nauraye, and L. Demarzi. Monte Carlo modelling of the treatment line of the Proton Therapy Center in Orsay. *Phys. Med. Biol.*, 54:2377–2394, 2009. [2.1](#)

- [65] H. Paganetti, H. Jiang, S. Y Lee, and H. M. Kooy. Accurate Monte Carlo simulations for nozzle design, commissioning and quality assurance for a proton radiation therapy facility. *Med. Phys.*, 31(7):2107–2118, 2004. 2.1
- [66] S. W. Peterson, J. Polf, M. Bues, G. Ciangaru, L. Archambault, S. Beddar, and A. Smith. Experimental validation of a Monte Carlo proton therapy nozzle model incorporating magnetically steered protons. *Phys. Med. Biol.*, 54:3217–3229, 2009. 2.1
- [67] H. Paganetti. Monte Carlo method to study the proton fluence for treatment planning. *Med. Phys.*, 25(12):2370–2375, 1998. 2.1
- [68] C. Grassberger, A. Lomax, and H. Paganetti. Characterizing a proton beam scanning system for Monte Carlo dose calculation in patients. *Phys. Med. Biol.*, 60:633–645, 2015. 2.1, 4.2
- [69] L. Grevillot, D. Bertrand, F. Dessy, N. Freud, and D. Sarrut. A Monte Carlo pencil beam scanning model for proton treatment plan simulation using GATE/GEANT4. *Phys. Med. Biol.*, 56:5203–5219, 2011. 2.1, 2.2.2
- [70] L. Grevillot, D. Bertrand, F. Dessy, N. Freud, and D. Sarrut. GATE as a GEANT4-based Monte Carlo platform for the evaluation of proton pencil beam scanning treatment plans. *Phys. Med. Biol.*, 57:4223–4244, 2012. 2.1
- [71] J. W. Eaton, D. Bateman, S. Hauberg, and R. Wehbring. *GNU Octave version 3.8.1 manual: a high-level interactive language for numerical computations*. CreateSpace Independent Publishing Platform, 2014. 2.1
- [72] R. Brun and F. Rademakers. ROOT - An Object Oriented Data Analysis Framework. *Nuclear Instruments and Methods in Physics Research A*, 389:81–86, 1997. 2.2.1
- [73] R. X. Zhu, F. Poenisch, M. Lii, G. O. Sawakuchi, U. Titt, M. Bues, X. Song, X. Zhang, Y. Li, G. Ciangaru, H. Li, M. B. Taylor, K. Suzuki, R. Mohan, M. T. Gillin, and N. Sahoo. Commissioning dose computation models for spot scanning proton beams in water for a commercially available treatment planning system. *Med. Phys.*, 40(041703), 2013. 2.2.3
- [74] IAEA. Absorbed Dose Determination in External Beam Radiotherapy. Technical Report Series No. 398, 2000. 2.2.3
- [75] B. Gottschalk. Techniques of Proton Radiotherapy: Transport Theory. *Unpublished [available via <http://arxiv.org/abs/1204.4470>]*, 2012. 2.3
- [76] M. J. Berger, J. S. Coursey, and M. A. Zucker. ESTAR, PSTAR, and ASTAR: Computer Programs for Calculating Stopping-Power and Range Tables for Electrons, Protons, and Helium Ions (version 1.21). <http://physics.nist.gov/Star>, 1999. 2.4
- [77] T. Bortfeld. An analytical approximation of the Bragg curve for therapeutic proton beams. *Med. Phys.*, 24(12):2024–2033, 1997. 2.4
- [78] B. Gottschalk. Physics of Proton Interactions in Matter. In H. Paganetti, editor, *Proton Therapy Physics*, pages 19–59. CRC Press, 2011. 2.4
- [79] W. D. Newhauser and R. Zhang. The physics of proton therapy. *Phys. Med. Biol.*, 60:R155–R209, 2015. 2.4

- [80] K. Kurosu, M. Takashina, M. Koizumi, I. J. Das, and V. P. Moskvina. Optimization of GATE and PHITS Monte Carlo code parameters for uniform scanning proton beam based on simulation with FLUKA general-purpose code. *Nuclear Instruments and Methods in Physics Research Section B: Beam Interactions with Materials and Atoms*, 336:45–54, 2014. [2.5.1.1](#)
- [81] L. Grevillot, T. Frisson, N. Zahra, D. Bertrand, F. Stichelbaut, N. Freud, and D. Sarrut. Optimization of GEANT4 settings for Proton Pencil Beam Scanning simulations using GATE. *Nucl. Instr. Meth. Phys. Res. B.*, pages 3295–3305, 2010. [2.5.1.1](#)
- [82] C. Jarlskog Zacharatou and H. Paganetti. Physics Settings for Using the Geant4 Toolkit in Proton Therapy. *IEEE Transactions on Nuclear Science*, 55(3):1018–1025, June 2008. [2.5.1.1](#)
- [83] ICRU. *Stopping Powers and Ranges for Protons and Alpha Particles*. International Commission on Radiation Units and Measurements, report no. 49, 1993. [2.5.1.1](#)
- [84] T. Toshito, A. Bagulya, A. Lechner, V. Ivanochenko, M. Maire, T. Akagi, and T. Yamashita. Validation of New Geant4 Electromagnetic Physics Models for Ion Therapy Applications. *Progress in NUCLEAR SCIENCE and TECHNOLOGY*, 219:918–922, 2011. [2.5.1.1](#)
- [85] A. Lechner, V. N. Ivanochenko, and J. Knobloch. Validation of recent Geant4 physics models for application in carbon ion therapy. *Nuclear Instruments and Methods in Physics Research Section B: Beam Interactions with Materials and Atoms*, 268(14):2343–2354, 2010. [2.5.1.1](#)
- [86] G. Hoff, T. Basaglia, Chansoo. Choi, M. C. Han, C. H. Kim, H. S. Kim, H. K. Kim, M. G. Pia, P. Saracco, and M. Begalli. Methods and Techniques for Monte Carlo Physics Validation. *Joint International Conference on Mathematics and Computation (M&C), Supercomputing in Nuclear Applications (SNA) and the Monte Carlo (MC) Method*, 2015. [2.6](#)
- [87] D. A. Low, W. B. Harms, S. Mutic, and J. A. Purdy. A technique for the quantitative evaluation of dose distributions. *Med. Phys.*, 25:656–661, 1998. [2.6.3.4](#)
- [88] D. A. Low and J. F. Dempsey. Evaluation of the gamma dose distribution comparison method. *Med. Phys.*, 30:2455–2464, 2003. [2.6.3.4](#)
- [89] D. A. Low. Gamma Dose Distribution Evaluation Tool. *Journal of Physics: Conference Series*, 250(012071), 2010. [2.6.3.4](#)
- [90] G. A. Ezzell, J. W. Burmeister, N. Dogan, T. J. LoSasso, J. G. Mechalakos, D. Mihailidis, A. Molineu, J. R. Palta, C. R. Ramsey, B. J. Salter, J. Shi, P. Xia, N. J. Yue, and Y. Xiao. IMRT commissioning: Multiple institution planning and dosimetry comparisons, a report from AAPM Task Group 119. *Med. Phys.*, 36(11):5359–5373, 2009. [2.6.3.4](#)
- [91] S. Stojadinovic, L. Quyang, X. Gu, A. Pompos, Q. Bao, and T. D. Solberg. Breaking bad IMRT QA practice. *Journal of Applied Clinical Medical Physics*, 16(3):154–165, 2015. [2.6.3.4](#)
- [92] G. Heilemann, B. Poppe, and W. Laub. On the sensitivity of common gamma-index evaluation methods to MLC misalignments in Rapidarc quality assurance. *Med. Phys.*, 40(3), 2013. [2.6.3.4](#)
- [93] A. Fredh, J. Bengtsson Scherman, L. S. Fog, and P. Munck af Rosenschöld. Patient QA systems for rotational radiation therapy: A comparative experimental study with intentional errors. *Med. Phys.*, 40(3), 2013. [2.6.3.4](#)

- [94] B. Gottschalk. On the scattering power of radiotherapy protons. *Med. Phys.*, 37(12):352–367, 2011. 4.2